

Studies for the Development of a Minimum Bias Trigger at  
Low Luminosities in the ATLAS-Experiment at the Large  
Hadron Collider

D I P L O M A R B E I T

zur Erlangung des akademischen Grades  
Diplom-Physikerin  
(Dipl.-Phys.)



eingereicht an der  
Mathematisch-Naturwissenschaftlichen Fakultät I  
Humboldt-Universität zu Berlin

von  
Regina KWEE  
geboren am 8. Februar 1981 in Berlin

Berlin, 19. Juli 2007

Gutachter:

1. Prof. Dr. Hermann KOLANOSKI
2. Dr. Klaus MÖNIG

# Contents

<b>1</b>	<b>Introduction</b>	<b>1</b>
<b>2</b>	<b>Physics Aims at LHC</b>	<b>3</b>
2.1	The Standard Model and Beyond . . . . .	3
2.2	Discovery Potential at ATLAS-LHC . . . . .	5
2.3	Cross-section Predictions for LHC Energy Scale . . . . .	9
2.3.1	Total Cross-Section . . . . .	11
2.3.2	Minimum Bias Events . . . . .	12
2.3.3	Diffraction Dissociation . . . . .	13
<b>3</b>	<b>ATLAS at LHC</b>	<b>15</b>
3.1	The Large Hadron Collider . . . . .	15
3.2	The ATLAS Experiment . . . . .	16
3.2.1	Inner Detector . . . . .	17
3.2.2	Calorimeter System . . . . .	22
3.2.3	Muon Spectrometer . . . . .	24
<b>4</b>	<b>Trigger and Data Acquisition System</b>	<b>26</b>
4.1	Motivation . . . . .	26
4.2	The 3 Trigger Level- and Data Acquisition System . . . . .	26
4.2.1	First Trigger Level - LVL1 . . . . .	26
4.2.2	High Level Trigger - HLT . . . . .	27
4.3	HLT Selection . . . . .	29
4.4	Trigger Performance Targets - Technical Information . . . . .	31
4.5	Event Data Model . . . . .	31
<b>5</b>	<b>Development of a Minimum Bias Trigger</b>	<b>33</b>
5.1	Motivation . . . . .	33
5.2	Minimum Bias Trigger Scintillators - MBTS . . . . .	34
5.2.1	Trigger Strategies of MBTS . . . . .	34
5.3	Concept of a Random based Track Trigger for Minimum Bias Events . . . . .	34
5.3.1	Trigger Strategy . . . . .	35
5.4	Trigger Pattern Reconstruction Algorithms on LVL2 and EF . . . . .	37
5.4.1	LVL2 Track Reconstruction Algorithm IdScan . . . . .	38
5.4.2	EF Track Reconstruction: NewTracking . . . . .	40
5.5	Background Studies for Possible Cuts . . . . .	42
5.5.1	Efficiency and Fake Rate . . . . .	45
5.5.2	Empty Event Rejection based on Spacepoints Requirements . . . . .	47

5.5.3	Adaptation of IdScan for low $p_T$ tracks . . . . .	52
5.5.4	Beam-Gas Rejection based on Track Requirements . . . . .	57
5.6	Timing Performance . . . . .	62
5.6.1	Timings in IdScan . . . . .	63
5.6.2	Timings in NewT . . . . .	63
<b>6</b>	<b>Implementation of the “Random based” Minimum Bias Trigger</b>	<b>66</b>
6.1	Trigger Requirements . . . . .	66
6.2	Minimum Bias Trigger Chain . . . . .	67
<b>7</b>	<b>Summary and Outlook</b>	<b>69</b>
<b>A</b>	<b>Glossary</b>	<b>72</b>
<b>B</b>	<b>Error Calculation for Efficiency Computation</b>	<b>75</b>
<b>C</b>	<b>Parameters for low <math>p_T</math> Adaptation in IdScan</b>	<b>76</b>

## Abstract

The large hadron collider LHC is a proton-proton collider at CERN and will reach a center of mass energy of  $\sqrt{s} = 14$  TeV and a luminosity of  $\mathcal{L} = 10^{34}$  cm<sup>-2</sup>s<sup>-1</sup>. This enables to search for the undiscovered Higgs particle predicted by the standard model and responsible for mass creation of the elementary particles. At these high energies new particles with masses up to 5-6 TeV can be created. For these processes a high momentum transfer  $Q^2$  is involved. However, in most of the cases in proton-proton collisions, up to  $10^7 - 10^8$  times for certain processes, *soft* interactions take place where only a small momentum is transferred. These events are usually called *minimum bias* events. As more than 20 of these minimum bias events will overlap in the detector at high luminosity they will form *pile-up*. Their event topology must be precisely understood in order to identify the rare physics processes of high  $Q^2$ .

However, the physics of low  $Q^2$ -processes is only insufficiently understood. Thus, the strategy of ATLAS, one of the major experiments at LHC, is to study these events at low luminosity of  $\mathcal{L} = 10^{31}$  cm<sup>-2</sup>s<sup>-1</sup> in order to obtain a clean signal of single minimum bias events. In the present work a concept for a minimum bias trigger is outlined as well as feasibility studies for the realization of the trigger. A random event selection will be employed at the first trigger level. On higher trigger levels possible background sources have to be rejected efficiently. Main background sources that are expected to arise from empty bunch-crossing and beam-gas events. Their rejection was studied in detail and is outlined together with the results. Furthermore, timing measurements have been performed in order to test if the trigger constraints can be met. The results as well as an outlook to the implementation of such a trigger are discussed.

## Zusammenfassung

Der “Large Hadron Collider”, ein Proton-Proton Ringbeschleuniger am europäischen Kernforschungszentrum CERN bei Genf wird kommendes Jahr in Betrieb gehen, um fundamentale, offene Fragestellungen über die Natur von Elementarteilchen bei bisher unerreichten Schwerpunktsenergien von 14 TeV und Luminositäten von  $\mathcal{L} = 10^{34} \text{ cm}^{-2}\text{s}^{-1}$  genauer zu beleuchten. Bei diesen hohen Schwerpunktsenergien können neue, sehr viel massivere Teilchen von bis zu 5-6 TeV entstehen. Insbesondere sucht man nach dem vom Standardmodell vorhergesagten Higgs-Teilchen oder aber Signaturen von “neuer Physik”. Bei allen diesen Wechselwirkungen, die mögliche Entdeckungen bergen, ist ein hoher Impulsübertrag  $Q^2$  involviert. Der dominante Prozess, manchmal bis zu  $10^7 - 10^8$  mal häufiger, sind allerdings Prozesse, bei denen nur ein geringer Impuls übertragen wird. Diese *weichen* Wechselwirkungen werden als **Minimum-Bias**-Ereignisse bezeichnet und man erwartet bei den hohen Luminositäten, dass sich mehr als 20 dieser Minimum-Bias-Ereignisse überlagern und dadurch sog. *pile-up* im Detektor bilden. Sie stellen den größten QCD-Untergrund dar und müssen genauestens bekannt sein, um die seltenen Ereignisse zu identifizieren.

Momentan versteht man allerdings die Physik der weichen Wechselwirkungen so unzureichend, dass sie nicht eindeutig vorhergesagt werden können. Die Strategie bei ATLAS, einem der vier größeren Experimenten am CERN, ist nun, diese Ereignisse bei niedriger Luminosität von  $\mathcal{L} = 10^{31} \text{ cm}^{-2}\text{s}^{-1}$  zu untersuchen, um zunächst überlagernde Prozesse zu vermeiden und ein sauberes Signal dieser Ereignisse zu erhalten.

In der vorliegenden Arbeit wird ein Konzept für einen Trigger, der bei solchen Minimum-Bias-Ereignissen auslöst, vorgestellt sowie die Studien zur Machbarkeit. Im Konzept ist vorgesehen, auf erster Triggerstufe zufällig Ereignisse zu selektieren und auf den höheren Triggerstufen mögliche Untergrundereignisse zu verwerfen. Hauptuntergrundquellen stellen sogenannte leere Ereignisse dar, wobei sich die Protonenbündel ohne Wechselwirkungen durchdringen, sowie Strahlgas-Ereignisse, wenn die Strahlprotonen mit Restgasmolekülen im Strahlrohr wechselwirken. Es wurden verschiedene Selektionsvariable untersucht und vorgestellt, die einen effizienten Minimum-Bias Trigger erlauben. Weiterhin werden die Ergebnisse von Zeitmessungen der Triggeralgorithmen präsentiert und es wird ein Ausblick auf die Implementierung eines solchen Triggers gegeben.

# Chapter 1

## Introduction

A new machine is currently built to give some answers of many outstanding questions about the nature of elementary particles. The large hadron collider LHC at CERN, the European center of nuclear research in Geneva, is almost finished in construction and designed for the search of the undiscovered standard model Higgs particle and possible signs of new physics. It will provide an important instrument being able to enter new energy territory by reaching a center of mass energy of 14 TeV realized by accelerated protons in the 27 km long LHC tunnel. They will collide with an luminosity up to  $\mathcal{L} = 10^{34} \text{ cm}^{-2}\text{s}^{-1}$  rising the rate of rare processes which are studied in dedicated detectors placed along the tunnel. ATLAS is one of four major such experiments.

The high energy and luminosity will on the other hand also lead to many processes that are not of primary interest. In most of the cases the interaction of protons causes only a small momentum transfer. Interesting physics signatures incorporate a large momentum transfer e.g. for a light Higgs production, these high  $Q^2$ -events are expected to be about  $10^6$  times rarer than the *soft* QCD-processes transferring only a small amount of the initial momentum. The soft interactions are called **minimum bias events** and form pile-up in the detector as more than 20 of such events are expected to overlap at design luminosity. It will be one of the challenges at LHC to identify the rare signatures out of this large QCD-background.

The physics of soft interactions is however rather insufficiently understood such that their cross-section can not be precisely predicted. Instead, they have to be measured in order to understand the pile-up they form in the detector. Ideally, they are studied at low luminosity when the probability of a proton-proton interaction is sufficiently small to avoid overlapping reactions. This enables a study of clean minimum bias signals. Therefore, these events have to be triggered in the start-up phase of LHC.

The studies of this thesis aimed at the development of such a trigger for ATLAS. The main criteria were to develop a concept allowing for the rejection of possible background sources which are expected to stem essentially from empty bunch-crossing events and the beam-gas interactions. Also halo events must be rejected which are created by beam interactions with parts of the LHC-machines. Due to the unknown rate of the beam-gas and halo events the studies in this thesis also targeted a development of a *toolkit* that should be able to react on different situations to realize an optimal selection of minimum bias events. Special care has to be taken to introduce only *minimal bias* in the event selection. The employment of a random trigger at first selection step is best suited for this purpose. At higher trigger levels minimum bias events have to be selected out of background events. This concept must fulfil the trigger constraints, time-critical processing should be avoided

in order to stay within the given trigger level latencies. Therefore, it has to be studied if only restricted information of the tracking system will be sufficient to meet the requirements of the event selection.

This thesis is organized as follows: In the first part of chapter 2 general physics aims at ATLAS are depicted, in the second part the phenomenological theory of the physics of minimum bias signals is introduced. Chapter 3 outlines the experimental systems in ATLAS with emphasis on the components relevant for the studies. The following chapter 4 describes the trigger and data acquisition system that will be able to handle the high event rates at ATLAS-LHC. In chapter 5 the topic of the minimum bias trigger is detailed as well as the results of the studies. This is the main chapter of the thesis. Chapter 6 briefly summarizes the results and gives details of a possible realization of a minimum bias chain, while the last chapter, chapter 7, gives an summary and an outlook to this topic.

# Chapter 2

## Physics Aims at LHC

### 2.1 The Standard Model and Beyond

The Standard Model (SM) is our current framework of elementary particle physics describing fundamentally the interaction of two different types of particles and three of the four known forces: The interaction between matter (and anti-matter) particles, which are called *fermions*, by the exchange of force-particles<sup>1</sup> which are *bosons*. The fermions are classified in quarks and leptons and each of them comprise three generations. Altogether twelve matter particles are known. The bosons represent the forces of which four are known in nature, but only three of them are described in the SM. One additional particle playing a key role in all interactions is the massive *Higgs-Boson* and it is the only particle in the Standard Model that has not been discovered yet. The unique role of the Higgs-Boson lies in a mechanism that gives mass to elementary particle (Higgs-mechanism).

#### Success and Failure of the Standard Model

The Standard Model has passed up to now every experimental test with high precision. It predicted e.g. three particles, the Z- and W<sup>±</sup>-Bosons, that are mediators of the weak force, before they were seen. Also the existence of the gluon, the mediator of the strong force, the top and charm quark, matter particles, were predicted and experimentally confirmed. Measurements at LEP, a former electron-positron collider at CERN, resulted in a Z-mass value of  $(91.1876 \pm 0.0021)$  GeV [1], W-mass measurements at LEP and TEVATRON (a US  $p\bar{p}$ -particle-collider) yielded a W-mass of  $(80.403 \pm 0.029)$  GeV [1]. Both results are in striking accordance with the Standard Model predictions. Despite the series of successful predictions, there are indications that the Standard Model is not the ultimate theory to describe nature completely. One reason is that the mass of Higgs boson itself is not predictable in the SM despite its fundamental role. Only constraints could be obtained from experiments and on the base of theoretical arguments. A lower limit of the Higgs mass of  $m_H > 114.4$  GeV at 95% C.L. [1] was introduced by direct searches at LEP. The upper limit is set by the theory allowing  $m_H < 1$  TeV, otherwise unitarity is violated in certain scattering processes. This limit could be further reduced by a fit to electro-weak data such that  $114.4 < m_H < 251$  GeV at 95% C.L. [2].

Still, it is also unsatisfactory that the Standard Model has 17 more free parameters for all fermion masses apart for those of the neutrinos that are massless in the original form

---

<sup>1</sup>An interaction can additionally take place via the Yukawa-coupling.

of the SM, three coupling constants (coupling of particle to the force), four angles of the matrix linking mass eigenstates to electroweak eigenstates (CKM-Matrix) and the vacuum expectation value of the Higgs phase. They have to be “put in by hand” instead of being derived from first principles.

However, the main problem is that the fourth force, gravity, is not included in the theory. Compared to the weak force the strength of gravity is about  $10^{-36}$  times smaller at low or modest energy scale.

Another insufficiency closely related to it is that the SM suffers from a problem known as the *hierarchy problem*. It predicts a divergent Higgs mass due to the vast scale difference of weak and gravitational forces. Therefore, an unnaturally precise fine-tuning of the order of the scale difference covering more than 30 orders of magnitude had to be introduced. Many extensions to the SM or new theories have been proposed to overcome this and other problems of our current theory leading to physics *Beyond the Standard Model*.

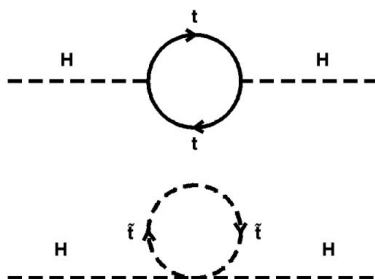


Figure 2.1: Resolving the hierarchy problem in the SM by introducing a supersymmetric partner particle  $\tilde{t}$  to the SM  $t$ . The contribution of quadratic divergencies in Higgs production cancels out automatically and no unnatural fine-tuning is needed in SUSY.

## Beyond the Standard Model

One possible solution to the hierarchy problem is proposed in the **Supersymmetric Theory** (SUSY) imposing a symmetry between fermions and bosons and postulating to each Standard Model particle a supersymmetric partner particle. They have the same quantum numbers like their SM partners except for the spin which differs by  $1/2$ . Thereby, each SM boson has a fermionic SUSY partner and each fermion has a scalar partner *sfermion*. If this symmetry is unbroken evidence for the SUSY particles would have arisen from current or previous experiments already as their masses would be the same like in the SM. So far, none of such SUSY particles has been observed. This requires that Supersymmetry is broken leading to masses up to the TeV scale, thus much higher as for the SM particles. The asset of introducing the concept of SUSY particles is that the unnatural fine-tuning can be avoided: radiative corrections in the Higgs mass cancel out automatically (stabilisation of Higgs mass) which is illustrated in figure 2.1.

The attractiveness of this theory has several more reasons. In SUSY a new quantum number called *R-parity* is introduced and defined as  $R = (-1)^{j+3B+L}$ , where  $j$  denotes the spin,  $B$  and  $L$  the baryon and lepton quantum number respectively. R-parity is assumed

to be a conserved quantity, otherwise it can predict a proton decay within a year which would exclude this model. Conservation of  $B + L$  implies that the baryon number itself is not necessarily preserved which is compatible with the observed baryon asymmetry in the universe. Supersymmetric theory also provides a candidate for so called Dark Matter, matter that must originate from unknown sources and consist of undiscovered particles: The preservation of R-parity in particular implies that the SUSY particles are produced in pairs. The lightest SUSY particle (LSP) should be stable, in which other SUSY particles eventually decay to. In many models the LSP is identified with the lightest neutralino  $\chi_1^0$ , interacting only weakly and being a stable massive particle. Other features of SUSY are that it allows easily unification of electroweak and strong force at GUT scale of  $10^{16}$  GeV that is the scale in the *grand unified theory* at which the gauge couplings are expected to have same strength. It likewise incorporates gravity in an natural way and is an essential part of string theory (see below).

Despite all the promising features of Supersymmetry this theory is a purely perturbation theory and not exactly formulated at finite interactions strength [3]. At LHC the masses of the supersymmetric partner particles will be accessible and already the first two years of data-taking might bring some evidence for such particles.

Many other theories beyond the Standard Model have been formulated to include also gravity. Ahead, there is Superstring Theory or just **String Theory** incorporating as an essential component Supersymmetry. Thus, String Theory claims to be able to answer to fundamental questions that are still open in the Standard Model. Moreover, it resolves conflicts of quantum mechanics and general relativity and a quantum theory of gravity emerges naturally. However, experimentally this theory is expected to be probed only at very high energies, much higher than accessible at LHC. Nevertheless relevant data also for String Theory are expected from LHC concerning the supersymmetric part of String Theory.

## 2.2 Discovery Potential at ATLAS-LHC

The LHC programme covers a wide range to probe our current theory for particle physics by precision measurements of e.g. CP-violations which is predicted by the SM. Furthermore, the discovery of the Higgs boson would be another, *the* major success of the Standard Model. In case no SM Higgs particle can be detected at LHC, physicists are prepared for systematical searches for new physics forseen in various SM extensions and perhaps even unexpected signals might be caught up at LHC. Exotic processes might also be produced like extra-dimensions or mini-black holes (that would decay practically instantaneously). In any case we expect that *something* has to emerge at the TeV scale up to which electroweak symmetry breaking is valid without becoming inconsistent with the current theory. The limit of the TeV scale applies also for supersymmetric extensions of the Standard Model.

At LHC there will be a more than seven fold increased energy and more than 100 fold higher luminosity as at the presently running machine TEVATRON where the highest c.m.e. of 1.96 TeV is currently available. As soon as LHC turns on rates of Standard Model channels are produced in a much higher number and when LHC reaches design luminosity it immediately enters new territory. New, heavy particles up to masses of 5-6 TeV can then be discovered [4].

## Search for the Higgs Boson

The importance of finding the Higgs boson has been outlined before. In contrast to the mass its decay modes are known because the SM predicts proportional coupling strength to the masses. The main Higgs production channels are either *direct* or *associated* production channels. They are illustrated in figure 2.2 by their Feynman graphs. For the different production channels different cross-sections were calculated as function of the Higgs mass. One expects that associated Higgs production will occur in fewer cases than direct created Higgs particles. Main contribution is anticipated from gluon-gluon fusion  $gg \rightarrow H$ . One can read this from figure 2.3.

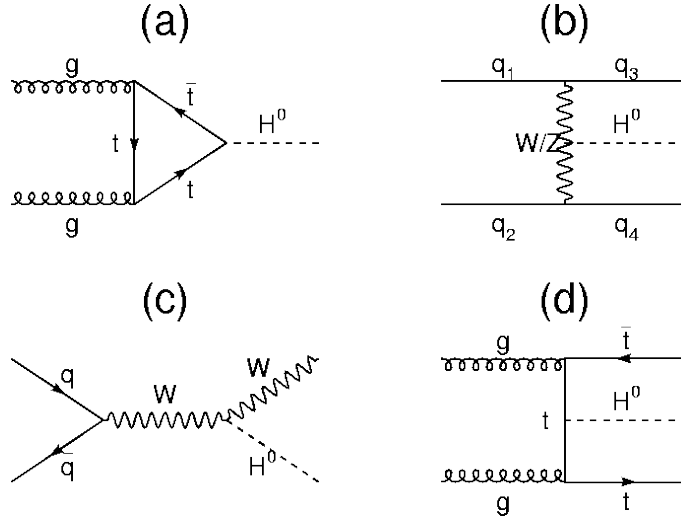


Figure 2.2: Higgs production modes either by gluon-gluon fusion (a)  $gg \rightarrow H$  and (d)  $gg \rightarrow t\bar{t}H$  or by vector boson fusion (VBF) (b)  $qq \rightarrow WW, ZZ \rightarrow qqH$  and (c)  $qq \rightarrow WH, ZH$ . The outcome is either a direct (a,b) or an associated (c,d) Higgs production.

The decay modes of the Higgs will exhibit distinctive event topologies. For an integrated luminosity of  $100 \text{ fb}^{-1}$  the expected signal significance is shown in figure 2.5 for Higgs discovery over the range that LHC will access. In the case the Higgs has a mass of more than  $\sim 150 \text{ GeV}$  it will be relatively fast and easy to discover due to the so called *golden channel* with four leptons in the final state  $H \rightarrow ZZ^{(*)} \rightarrow 4l$  which would be quasi background-free and thus show a clean signal, even over a wide range of  $130 < m_H < 600 \text{ GeV}$  (apart from a break-down at  $\sim 160 \text{ GeV}$ ). More challenging will be the case if the Higgs has a small masses, i.e.  $m_H < 200 \text{ GeV}$ , though this is the best motivated region. For  $m_H < 130 \text{ GeV}$  the channel  $H \rightarrow \gamma\gamma$  is relevant but it would be only a small peak over irreducible, non-resonant background. Therefore, highest performance of the electromagnetic calorimeters is essential. The Higgs particles created associated to  $t\bar{t}$  would mostly decay purely hadronically, ending up in  $H \rightarrow b\bar{b}$ . As the top quark would also decay in beauties, i.e.  $t \rightarrow \bar{b}\nu$  and  $t \rightarrow bq\bar{q}$ , four b-jets have to be tagged to minimise possible background e.g. from light-quark or gluon-jets, i.e.  $t\bar{t}jj$ . This decay is shown in figure 2.4.

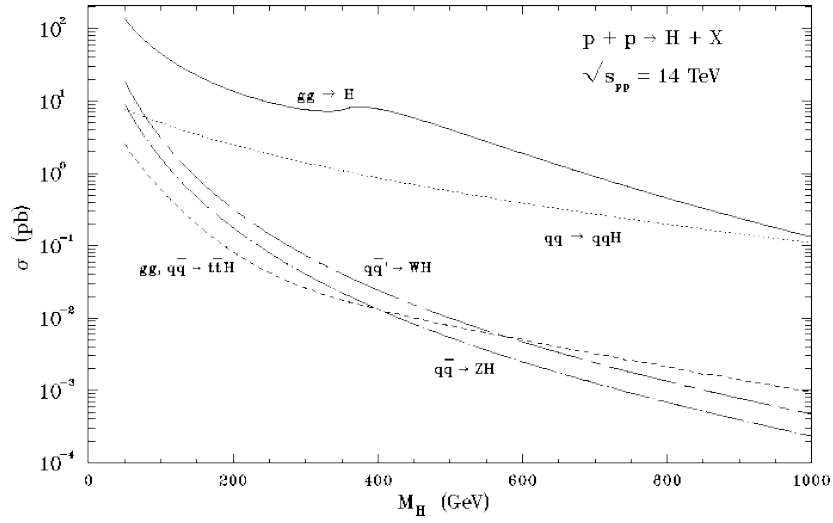


Figure 2.3: Cross-section predictions for different channel modes. The associated Higgs production has smaller cross-sections than the direct production. Largest contribution may come from  $gg \rightarrow H$ .

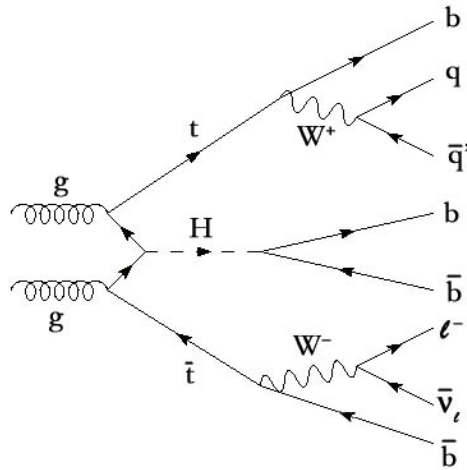


Figure 2.4: Higgs decay produced in  $t\bar{t}H$ -channel.

## Searches Beyond the Standard Model

In supersymmetric extensions of the SM, in particular in the minimal supersymmetric Standard Model (MSSM) a light Higgs particle is favoured, though in SUSY two Higgs doublets are required to realize up- and down like quarks. Thus, a Higgs sector of five Higgs particles is imposed<sup>2</sup> in the MSSM. At LHC the dominant supersymmetric process would be pair production of squarks  $\tilde{q}$  and gluinos  $\tilde{g}$ . It was estimated in [4] that - if gluinos and squarks will have a mass of  $\sim 1$  TeV - already at a luminosity of  $\mathcal{L} = 10^{33}$   $\text{cm}^{-2}\text{s}^{-1}$  about  $10^4$  pairs of  $\tilde{g}\tilde{g}$ ,  $\tilde{g}\tilde{q}$  and  $\tilde{q}\tilde{q}$  may be produced. A typical decay would then

<sup>2</sup>In the SM there is one complex Higgs doublet.

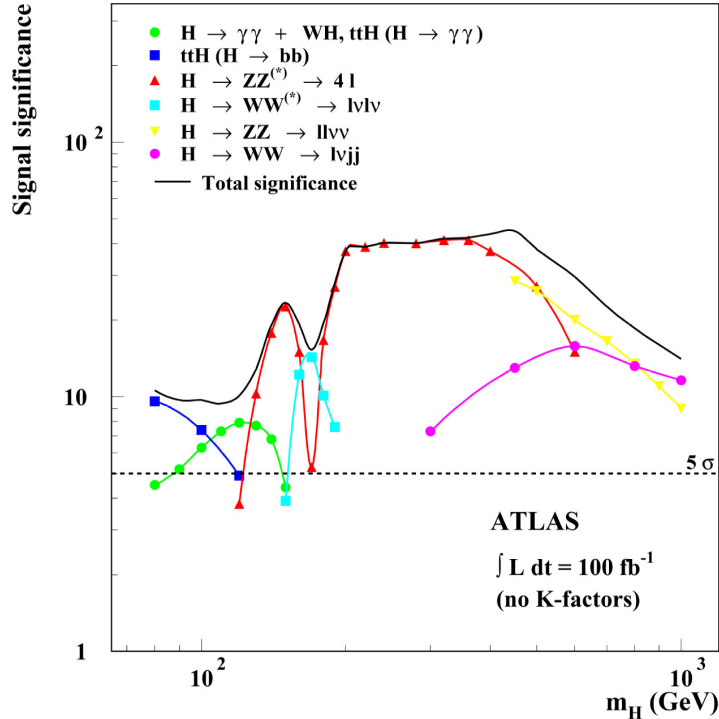


Figure 2.5: The SM-like Higgs can be seen in ATLAS in most cases with  $5\sigma$  significance.

look like  $\tilde{q} \rightarrow q\chi_2^0 \rightarrow ql^+l^-\chi_1^0$ , a decay of a squark into a quark and one of the neutralinos which itself will decay into a lepton pair and the lightest neutralino. If R-parity is not violated two neutralinos will occur in the final state being invisible for direct detection. They will leave large missing energy in the detector which would be, together with a jet of high  $p_T$ , a clear and distinctive sign for SUSY. The mass of gluinos and squarks is ought to be at most 3 TeV. Thereby, these particles should be detected at LHC if they exist.

### Precision Measurements

Precision measurements will be possible at hadron colliders as TEVATRON demonstrated. The Standard Model predicts **CP-violation** in the b-sector which will be studied in a dedicated large hadron collider beauty (LHCb) experiment, designed to exploit also decay channels that are not accessible otherwise due to rather modest  $K/\pi$  separation in ATLAS or CMS. Nevertheless, also at ATLAS B-physics studies will be performed profiting from higher collision rates<sup>3</sup>. Studies of CP-violation are strongly motivated by open questions what the origin of CP-violation is and what consequences to the development of our universe follow. It was found that CP violating processes are not sufficient to explain the asymmetry between the produced baryons and anti-baryons in the early universe (baryogenesis). Investigating CP-violation means measuring the lengths and angles in the unitarity triangles given by the CKM-matrix. Unitarity holds if  $V_{CKM}V_{CKM}^\dagger = 1$  leading to the set of equations by  $\sum_j V_{ji}V_{jl}^* = \delta_{il}$ , where  $j$  represents the quark flavours. In direct searches in processes where CP is not preserved and in indirect searches which are

<sup>3</sup>At LHCb the luminosity is inflated to  $\mathcal{L} = 10^{32} \text{ cm}^{-2}\text{s}^{-1}$ .

sensitive to higher order loop processes one can systematically probe the predictions of the Standard Model being sensitive also to possible new physics.

Other precision measurements concern the **top quark** mass. The top quark was discovered at Fermilab where the mass was measured to  $170.9 \pm 1.1(\text{sta}) \pm 1.5(\text{sys})$  GeV [5]. What can we learn then by knowing the top mass with higher accuracy? The top is the heaviest elementary particle so far discovered and only after the discovery of the b-quark we knew that the top-quark existed. At LHC the statistics on SM channels will improve intensively and the top mass can be measured with highest precision. LHC will be a factory of  $t\bar{t}$  pairs, producing 1 event/s which are  $10^7$  per year already at luminosities in the initial phase of  $\mathcal{L} = 10^{33} \text{ cm}^{-2}\text{s}^{-1}$ . In fact the  $t\bar{t}$  production rate will be so high, that it becomes a dangerous background in direct Higgs search. From this point of view detailed understanding of the top quark is crucial. Thus, the identification of top pairs out of the large QCD background is one experimental challenge. Single top events are easier to trace but the Higgs boson cannot be produced associated to single top quarks. Top quark measurements can further be used to predict the Higgs mass. Due to limited statistics in the former and present experiments at Fermilab or at LEP the top-mass measurements have relatively large uncertainties which transfers to the Higgs mass prediction. At LHC the statistics allow for much higher precision.

## 2.3 Cross-section Predictions for LHC Energy Scale

All of the processes promising a discovery of new physics mean to search for essentially high  $p_T$ -signatures in the detector arising from *hard interactions*. The main challenge at LHC is to find these signatures out of the so much larger QCD background which is a direct consequence that the proton is a composite, extended particle. Moreover, the proton-proton collider will be in fact a gluon-gluon collider because the gluon density distribution will be most relevant at LHC energies and small  $x$  (fraction of the proton momentum). This gives rise to any QCD-cross-section. For different processes the cross-sections is shown in figure 2.7.

Most of the interactions of the partons are *soft interactions* and which is - like in any other hadron collider machine - the dominant process. Any high  $Q^2$  process is much rarer and will be additionally overlapped by at least 20 so called **minimum bias** events at design luminosity originating from soft interactions causing activity in the whole detector acceptance. Soft interactions are characterized by an energy scale of the order of the hadron size  $R \sim 1 \text{ fm}$  which is the only typical scale in these processes. The momentum transfer is usually very small due to  $|t| \sim 1/R^2$  where  $|t|$  the corresponding Mandelstam variable.

In *hard* interactions there is next to the hard-scale still the soft scale, i.e. the hadron size, present. The high momentum transfer allows to use perturbative QCD, however part of the process is of non-perturbative origin incorporated by quark and gluon density functions. With what is known as “factorization theorems” one ensures that perturbative and non-perturbative parts can be treated independently.

QCD has been very successively probed in the frame of perturbation theory, i.e. for hard interactions which are characterized by a high momentum transfer. This holds for  $p_T \gtrsim 2 \text{ GeV}$ . However, two problems arise when one departs from the QCD-scale. At  $p_T \sim 2 \text{ GeV}$ , where perturbative QCD is still applicable, the interaction cross-section of two

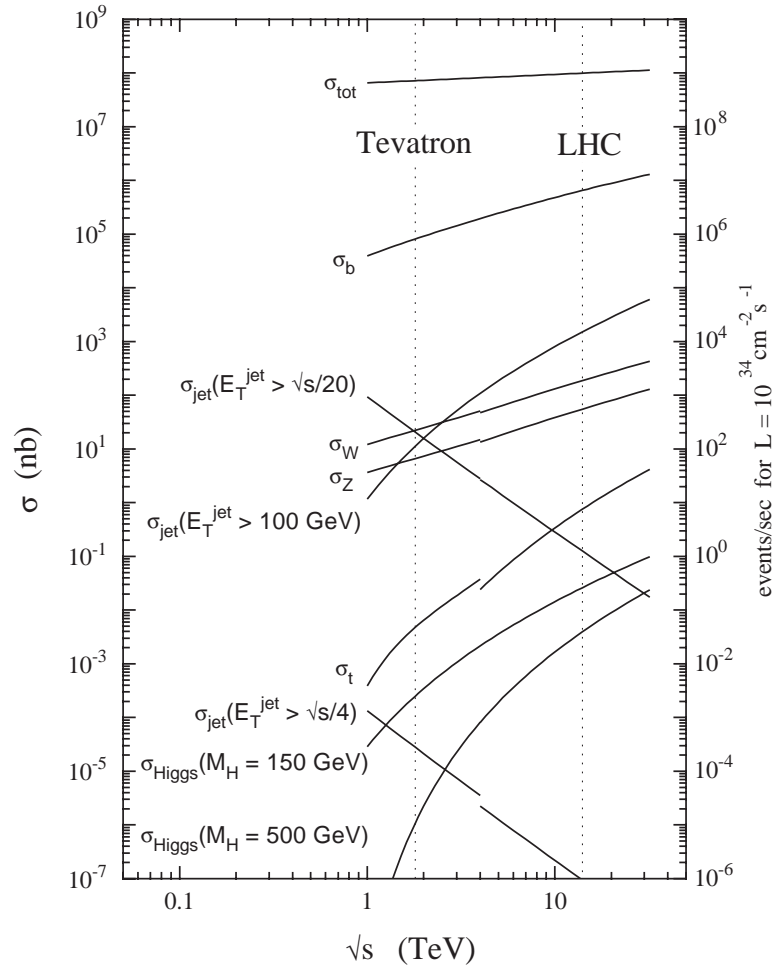


Figure 2.6: Cross-section predictions for different physics processes at LHC. Compared to QCD-background e.g. heavy jet production where  $E_T^{\text{jet}} > 100 \text{ GeV}$  the light Higgs with  $m_H = 150 \text{ GeV}$  is produced only with a ratio of  $10^{-5}$ .

partons becomes larger than the proton-proton cross-section. This could be understood in terms of *multiple interactions* where the probability of partonic interaction of several parton pairs in a proton is enhanced. This is also supported by recent data from CDF where multiple interactions were directly measured [7]. Nevertheless, a problem remains for smaller  $p_T$ -values. There, the perturbative QCD differential cross-section for 2 parton  $\rightarrow$  2 parton scattering diverges for  $p_T \rightarrow 0$  and a minimal  $p_T$  had to be introduced [27]:

$$\sigma_{int}(p_{T_{min}}) = \int_{p_{T_{min}}^2}^{s/4} \frac{d\sigma}{dp_T'^2} dp_T'^2$$

The most successful theory for soft interactions is a phenomenological approach known as *Regge Theory*. According to Regge theory hadrons interact by the exchange of *pomerons* that are characterized by vacuum quantum numbers. The way the pomeron interacts with the proton will result in distinctive event topologies. The low energy scale makes soft interactions intrinsically non-perturbative and as already mentioned perturbative QCD is inadequate to describe these processes. However, there exist several approaches to translate the pomeron into QCD-language, i.e. describe the interactions by gluon exchange [12]. The ‘‘QCD-pomeron’’ would correspond to a two gluon exchange to realize the pomeron quantum numbers, in order to exchange no net-colour.

### 2.3.1 Total Cross-Section

The total  $pp$ -cross-section can be split into an elastic and inelastic part where the latter can be divided into *non-diffractive* and *diffractive* contributions. The diffractive part itself consists of single (sd), double (dd) and central diffractive (cd) processes.

$$\sigma_{tot} = \sigma_{el} + \underbrace{\sigma_{sd} + \sigma_{dd} + \sigma_{nd}}_{\sigma_{inel}} + (\sigma_{cd}) \quad (2.1)$$

Principally in all inelastic processes low and high  $Q^2$ -interactions can take place showing each a distinctive event topology, although processes with low  $Q^2$  are dominant. In predictions for the total cross-section at LHC-energies data from various experiments were incorporated resulting in an  $(\ln s)^\gamma$  fit to explain the rising slope at higher energies as it is shown in figure 2.7. At TEVATRON highest energies were achieved so far. In the CDF experiment also at  $\sqrt{s} = 1.8$  TeV the total proton-antiproton cross-sections was measured to  $(80.03 \pm 2.24)$  mb [9] while the E710 experiment at  $\sqrt{s} = 1.8$  TeV measured the total cross-section to be  $(72.8 \pm 3.1)$  mb [8]. The difference from both results cause an ambiguous shape of the cross-section at LHC energies. While an  $\ln^2 s$  rise is favoured by the result of CDF, an  $\ln s$  slope is favoured by E710. From cosmic ray data no conclusion could be derived as measurements are relatively widely spread and introduce themselves large uncertainties. Thus, at LHC energy the cross-section prediction lies at  $\sim 100$  mb, but has still large uncertainties of about 30 mb.

Also expectations from MC studies are not quite unambiguously. The mechanism of the pomeron exchange is included in Monte Carlo simulations combined with perturbative QCD to cover low and high  $Q^2$ -interactions. The simulation of single contributions mentioned in equation 2.1 yielded a total cross-section ranging from 100 mb - 120 mb. An overview of MC studies as they were performed in [10] and [27] is tabled in 2.1. Central diffraction (see below) could not be simulated within PYTHIA, but it could in PHOJET.

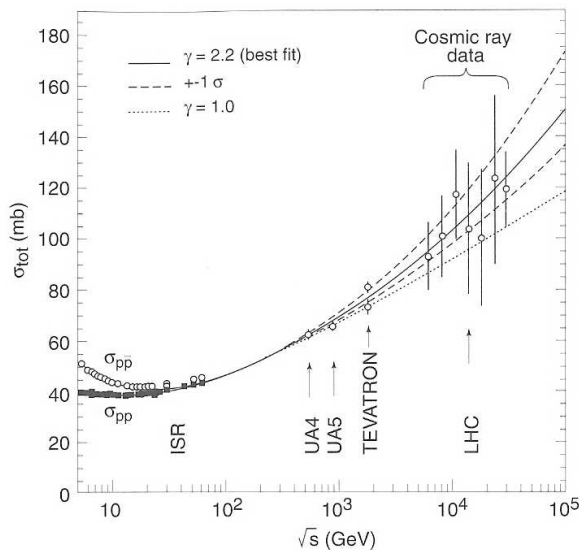


Figure 2.7: Cross-section prediction for LHC. Total  $p\bar{p}$  (empty dots) and  $pp$  (black dots) were fitted to  $(\ln s)^\gamma$ . At LHC energies the fit-prediction ranges from 90-120 mb.

However, it has a comparatively small cross-section and they include hard scattering processes such that they do not contribute to background in searches of new physics. More conclusive is that in both simulations the largest contribution is due to non-diffractive processes. They are usually referred to minimum bias events and are described in more detail in the following section. The subsequent section summarises the relevant facts about the diffractive physics.

### 2.3.2 Minimum Bias Events

Minimum bias events will form *pile-up* in the detector when LHC reaches design luminosity. Knowledge of their event topology is crucial for a successful physics programme in ATLAS because they occur dominantly. Additionally to their high cross-section a single minimum bias event creates activity in the whole detector which will “pile up” and complicate the differentiation of single reactions.

In literature, minimum bias events are defined in slightly different ways. Sometimes, they comprise non-diffractive and double diffractive interactions (and are called non-single-diffractive [27]), which is rather an experimental definition based on trigger systems of the respective experiment defining a minimum bias event as an event that is triggered with minimal trigger conditions.

However, from the theoretical point of view, they are identified only as non-diffractive events. These denote interactions with small momentum transfer in a color field (by gluon emission) leading to projections of color-neutral sets of partons into hadronic states distributed all over the detector. In figure 2.8 this process is illustrated. As such reactions occur practically always in hadron collisions they are called *minimum bias* events. The expression *bias* refers to the experimental setup to capture such an event defined by trigger thresholds in the event selection. Throughout this thesis a similar definition is used. Non-diffractive interactions will contribute most, therefore they were taken as reference for tuning studies of the trigger. Nevertheless, diffractive samples were also investigated and

cross-section [mb]	PYTHIA 6.205	PHOJET 1.12
$\sigma_{tot}$	101.5	119.1
$\sigma_{el}$	22.2	34.5
$\sigma_{inel}$	79.3	84.6
$\sigma_{sd}$	14.3	10.8
$\sigma_{dd}$	9.8	4.1
$\sigma_{cd}$	-	1.4
$\sigma_{nd}$	55.2	68.3

Table 2.1: Cross-section predictions at LHC energy of 14 TeV. Despite of different predictions for  $\sigma_{tot}$  one recognises that the non-diffractive part (nd), usually referred to minimum bias events, contributes largely in contrast to single and double diffractive (sd, dd) events. While in PHOJET also central diffraction (cd) was simulated, it was not in PYTHIA [10], however the differences between these two model are relatively large (more than 50% for the elastic processes).

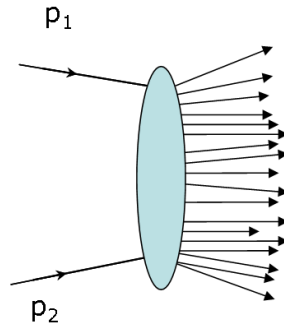


Figure 2.8: A typical non-diffractive process: By gluon radiation in a proton-proton collision a color field is produced which allows final states particles everywhere in the detector.

handled here as a separate class, so one can see any impacts on these as well.

### 2.3.3 Diffractive Dissociation

Common to all definitions of processes with diffractive dissociation is that during the process no quantum numbers except the vacuum quantum numbers are exchanged [12], [11]. This leads to a completely different event structure compared to non-diffractive events, showing an exponential suppression of final state particles in the central detector region. So called rapidity gaps are the main characteristics of these processes which are sketched in figure 2.9. As already mentioned there are different types of diffractive dissociation as single diffractive (sd), double diffractive (dd) and central diffractive (cd) dissociation all being inelastic interactions:

$$\text{sd: } pp \rightarrow p'X \quad \text{dd: } p_1 p_2 \rightarrow X_1 X_2 \quad \text{cd: } pp \rightarrow p'Xp'$$

Formally they can be described by pomeron exchange between the protons. Thereby, the proton can be excited such that it dissociates into a system of mass  $M$ . Due to

a missing color field no particles can couple and a rapidity gap is produced. In single diffractive dissociation the rapidity gap is between the quasi-elastic scattered proton and the dissociated final state system, in double diffractive dissociation it is very similar apart from the quasi-elastic proton that will also transform to a dissociated system. In central diffractive dissociation two rapidity gaps are generated, it is a so called *multi-gap* event, originating from the double pomeron exchange.

In the following merely the terminology “diffraction” will be employed instead of “diffractive dissociation” for practical reasons. However, diffractive dissociation rather describes the physical process [11].

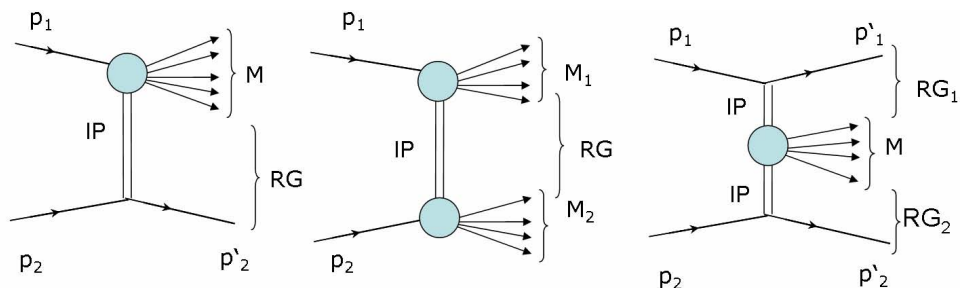


Figure 2.9: Schematic processes for diffraction: The exchange of color-neutral objects, here in Pomeron picture ( $\mathbb{P}$ ), gives rise to rapidity gaps (RG) where final state particles are exponentially suppressed. Shown are single diffractive (left), double diffractive (middle) and central diffractive dissociation (right). The dissociated system is assigned a mass  $M$ .

# Chapter 3

## ATLAS at LHC

At LHC there will be four major experiments each one executing a dedicated physics programme to explore the innermost of particles constituents. Two of the experiments are general purpose detectors, ATLAS, a toroidal LHC apparatus, and CMS, the compact muon solenoid. Both detectors surround their respective collision point almost completely. In contrast, the dedicated B-physics experiment LHCb is build in forward direction (quite similar to HERA-B at DESY). ALICE, a large ion collider experiment, is like ATLAS or CMS a general-purpose detector and symmetric in construction dedicated to heavy ion physics. There one will study amongst others quark-gluon plasma from heavy ion collisions. In this thesis only the ATLAS experiment will be described in more detail with strong emphasis on the detector components relevant for these studies.

### 3.1 The Large Hadron Collider

The Large Hadron Collider is situated in the former LEP-tunnel at CERN and has a circumference of about 27 km. There are two beam-pipes in the main tunnel for each proton beam <sup>1</sup> surrounded by 120 m long magnets cells of 8.4 T field strength to keep the protons in the orbit. The beam energy will be 7 TeV making discoveries possible for new particles with masses up to 6 TeV. Each beam will consist of more than 2,800 bunches, where each bunch will contain around  $10^{11}$  protons at the start of nominal fill. One such bunch will be several cm long at the time of injection but squeezed to 16 microns width and 16 microns length at the collision points [13]. The bunch crossings will have a nominal time distance of 25 ns, in the initial phase it will be 75 ns. Throughout this thesis the expression *bunch crossing* is used in the same way as an *event*, whereas an *interaction* is employed as synonym of the expression *collision* such that an event contains usually several collisions. ATLAS is build around one such collision point.

The coordinate system which is used in ATLAS is a right-handed frame with the x-axis pointing to the centre of the LHC-orbit, y-axis going upwards and the z-axis following the beam direction. The azimuthal angle  $\phi$  increases clockwise looking in positive z direction. The origin is normally taken as the nominal interaction point (IP).

The most common kinematic variables used in hadronic interactions are the pseudo-rapidity  $\eta$  defined as  $\eta = -\ln(\tan \theta/2)$ , where  $\theta$  is angle with respect to to the z-axis, and the transverse momentum  $p_T$ , which is the momentum perpendicular to the z-axis.

---

<sup>1</sup>There will be also the possibility to accelerate heavy ions such as Pb.

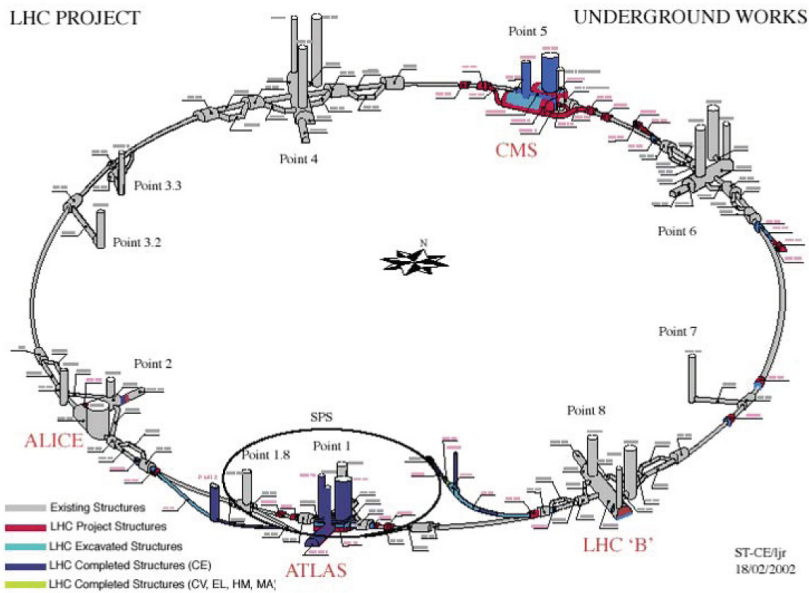


Figure 3.1: Four major experiments located along the tunnel of the Large Hadron Collider. ATLAS, CMS, LHCb and ALICE. ATLAS is situated at Point 1.

## 3.2 The ATLAS Experiment

New physics will be probed at ATLAS by proton-proton collisions. At  $\sqrt{s} = 14$  TeV the substructure of the protons can be resolved such that LHC becomes in first order a gluon-gluon collider. One basic consequence is that longitudinal quantities of the colliding partons are unknown<sup>2</sup>, however *transverse* quantities are preserved which is respected in the construction of the single sub-detectors in ATLAS.

The ATLAS detector consists of three main sub-systems. Following the way of the particle through the detector, it first passes the **Inner Tracking System** leaving hits (if it carries an electric charge) ideally in the pixel-detector, in the microstrip semi-conductor tracker system (SCT) and in the drift tubes of the transition radiation tracker (TRT). The trajectory of the charged particle will be bended by a homogeneous magnetic field of 2 T to determine its transverse momentum and charge sign. Then it continues to the **Calorimetric System**. If the particle is a photon or an electron its energy will be fully absorbed in the electromagnetic calorimeter, if it is of hadronic nature the hadronic calorimeter will absorb it. If it is neither of them it can be only a muon or a uncharged, weakly interacting particle like a neutrino or the postulated neutralino. In case it is a muon we can trace it in the **Muon Spectrometer**, otherwise one can observe the neutral weakly interacting particles only indirectly by some amount of missing transverse energy. A simulation of the complete detector, which fills in reality space of 35 m height, 55 m length and 32 m width, is shown in figure 3.2.

<sup>2</sup>In contrast to  $e^+e^-$  colliders where the collision energy is known due to scattering of pointlike particles.

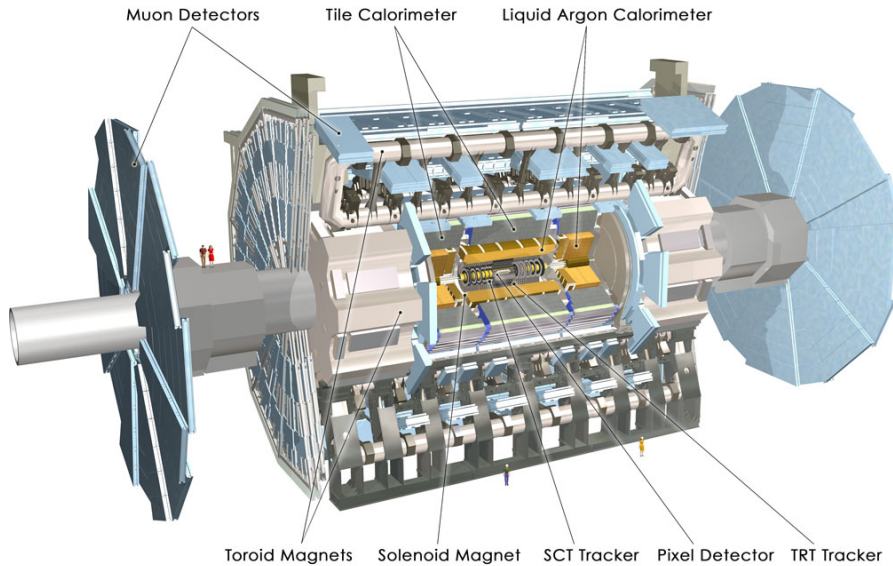


Figure 3.2: Computer animation of the ATLAS detector in its full beauty. Indicated are the main components of the detector. Especially the large toroidal magnets are eye-catching, giving ATLAS the name.

### 3.2.1 Inner Detector

The inner tracker system will provide track information to reconstruct with high efficiency and low fake rate charged particles inside the inner detector acceptance of  $|\eta| < 2.5$ . It is designed to detect particles with  $500 \text{ MeV} \lesssim p_T \lesssim 500 \text{ GeV}$ . In particular the hits in the inner detector are used to reconstruct precisely primary and the secondary vertices which are crucial for b-tagging. Challenging is the environment of high multiplicity events in which the inner detector will be operating. Despite the expected high track densities accurate position measurements of single tracks have to be performed. At nominal luminosity up to 1000 particles can be created irradiating the detector in a time distance of 25 ns [14]. This requires radiation hard technology especially close to the interaction point which can be realized by semiconducting detectors. Two such detectors will be employed, one using pixels for detection (pixel detector), the other microstrips (SCT-detector). The outer part of the inner detector uses drift-tubes and features detection of transition radiation (TRT detector). They are shown in figure 3.3. The TRT has been completely excluded in the studies, relevant for our approach to trigger minimum bias are only the silicon sub-detectors. Specifically the occupancy probability is outlined for one pixel cell or SCT-microstrip indicating the noise rate which was studied in more detail for the rejection of empty bunch-crossing events.

#### Pixel-Detector

The pixel detector is situated nearest to the collision point and can measure the hit positions with highest accuracy. However, it will also suffer most from radiation damage due to the high track densities. This concerns in particular the closest pixel layer (“B-

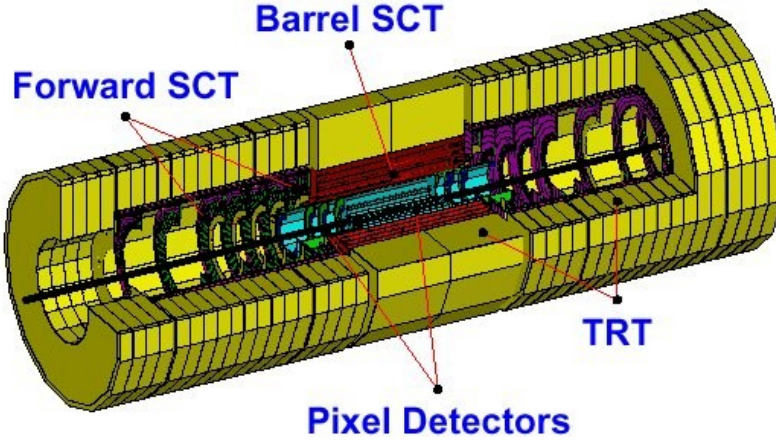


Figure 3.3: The tracking system, consisting of two silicon sub-detectors pixel and SCT and a gaseous tracking chambers featuring transition radiation detection TRT.

layer”) which will have to be replaced after about four years of operation<sup>3</sup>.

The total pixel system consists of a barrel part for the central region and endcaps on each side covering the forward and backward region. The barrel comprises three concentric cylinders with radii of 50.5 mm, 88.5 mm and 122.5 mm. The five wheels of each endcap are placed before and after the barrel. The basic unit of the pixel detector is a unified designed module mounted in mechanical and cooling sub-elements called staves in the barrel and sectors in the endcap. In total there are 1508 modules in the barrel region and 720 modules in the endcap regions. On each module the sensor unit is arranged together with 16 front-end (FE) chips and a control chip being amongst others responsible for collection of information in the FE-chips. The FE chips receive signals from the sensor that is a n-bulk with a highly n-doped implant (also known as “ $n^+$ -in- $n$ ”). It contains an active array of 60.8 mm  $\times$  16.4 mm were 144  $\times$  328 pixel cells, each of the size 50  $\mu\text{m}$   $\times$  400  $\mu\text{m}$ , are placed. A resolution can thereby be achieved to 14  $\mu\text{m}$  in  $r - \phi$  and 115  $\mu\text{m}$  in z-direction. Increasing the resolution is possible for analogue read-out using the height of the pulse. Overall, there will be more than 80 millions read-out channels.

**Noise in the Pixel-Detector** The initial charge collected at the electrodes of the transistors (Bipolar and CMOS technology is used) is pre-amplified before a discriminator threshold passes the signal to the read-out buffers. The lowest discriminator threshold<sup>4</sup> is set to 2000 e to meet the requirement of correct time assignment to the signal in a 25 ns clock. This demands very low noise from the electronics and also a small dispersion of the discriminator thresholds which means that the threshold values for all pixel chips should not largely deviate from its nominal value. These two noise sources compose the effective noise  $\sigma_{\text{eff}}$  which is set to 1/5 of the lowest threshold, i.e. 400 e, to ensure clear differentiation between signal and noise also for initial low luminosities. The FE chips represent a significant heat source dissipating more than 15kW into the detector volume.

<sup>3</sup>This assumes 3 years at  $\mathcal{L} = 10^{33} \text{ cm}^{-2}\text{s}^{-1}$  and one more at  $\mathcal{L} = 10^{34} \text{ cm}^{-2}\text{s}^{-1}$ .

<sup>4</sup>The unit is the electron charge e.

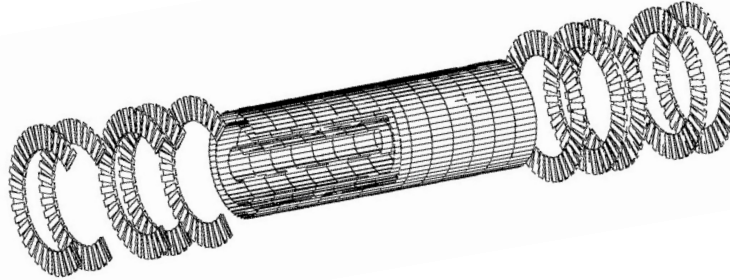


Figure 3.4: Arrangement of pixel detector components. The barrel, which consists of three cylindrical layers, is enclosed by 5 disks at each side representing the pixel endcaps. This figure is taken from [15].

This has negative effects on the electronic devices, mainly the increase of the temperature dependant leak current in the transistors (which disables the functionality of the devices) and is taken out by integrated cooling channels in the detector support elements (staves and sectors) [16]. Therefore, the pixel detector will be operated at  $-10^{\circ}\text{C}$ .

**Spacepoint Formation** The pixel detector will provide three precision measurements per track which are used in the pattern recognition algorithms. To reconstruct spacepoints raw data from the read-out buffers (see next chapter) have to be unpacked (known as *Bytestream Decoding* or *Bytestream Unpacking*) which is one of the three steps to be measured in order to verify whether trigger constraints can still be met in the selection of minimum bias events. The second step is *clustering* of neighbouring pixel cells information. These hit clusters can be in the third step directly transformed into pixel *spacepoints* by a “local-to-global” transformation [26] as they provide already two dimensional (*surface*) position information<sup>5</sup>.

### Microstrip Semi-Conductor Tracker - SCT

The SCT is based on silicon strip technology and covers as well the complete inner detector acceptance. It is divided into a barrel part of four concentric cylinders at radial positions of 300 mm, 373 mm, 447 mm and 514 mm and an endcap part of nine disks on each side at  $z$ -positions ranging from  $z = \pm 835 \text{ mm} \dots \pm 2778 \text{ mm}$  as shown in figure 3.5. The cylindrical layers comprise in total 2112 SCT-modules while all disks count 1976 modules. The modules in the endcaps are slightly different constructed being tapered in order to be arranged in circular sectors. On a single module four sensors are mounted, two at the front- and two at the back-side. Each such sensor is a p-strip read-out in an n-bulk silicon (“p-in-n”-sensor). It has a size of 63.6 mm length and 64 mm width and contains 768 strips. One microstrip is  $18 \mu\text{m}$  wide and 62 mm long. In balance with minimisation of costs and read-out channels with hit occupancy per strip two of the sensors are daisy-chained forming a strip length of 12.8 cm. The strips have a distance of  $80 \mu\text{m}$  in the

<sup>5</sup>Together with the position of the pixel cell, one has three dimensional localization information.

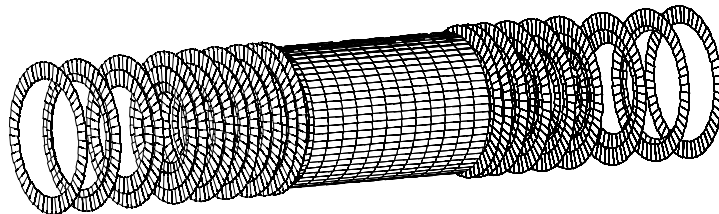


Figure 3.5: Arrangement of the SCT detector components. The barrel, which consists of four cylindrical layers and nine disks at each side of the endcap. This figure is taken from [18].

barrel and on average  $\sim 80 \mu\text{m}$  in the endcaps. The back-side is staggered by a small stereo angle of 40 milliradian ( $2.3^\circ$ ) which gives a  $r - \phi$ -resolution of about  $20 \mu\text{m}$ . The introduction of stereo angle between front- and back-sensors is primarily done to be able to resolve the second dimension (z-coordinate, the first is given in  $\phi$  and the third dimension is provided by  $r$ ). The amount of rotation with respect to the front-side was chosen to be very small as less fake spacepoints, so-called *ghosts* are formed. This is illustrated in figure 3.6 where two sets of read-out strips are shown, one with a small rotation angle and one with  $90^\circ$ . A small angle in between the strips covers obviously a smaller area and reduces thereby the impact of ghosts in the pattern recognition algorithms as for the case when the microstrips are arranged perpendicular to each other. An advantage of the microstrip concept compared to pixel read-out is an intrinsic noise suppression for the SCT, which will be very useful for noise event rejection.

**Noise in the SCT** The noise source is caused (like for the pixel-detector) in the FE-chips of the detector. Per module there will be 6 FE-chips each of it consisting of control sections and 128 channels. The control sections are likewise clocked by the LHC frequency of 40 MHz, they receive the read-out trigger signal, set the thresholds for the front-end transistors and contain analogue-to-digital converters as the SCT has binary read-out. The discriminator threshold is set to  $1 \text{ fC} = 10^{-15} / 1.6 \cdot 10^{-19} \hat{=} 6250 \text{ e}$ . The effective target noise  $\sigma_{\text{eff}}$  should not exceed 1500 e [18] corresponding to an occupancy of  $3 \cdot 10^{-4}$ , however this was changed in the studies (see also section 5.5.2). The operation of the SCT detector will be at  $-7^\circ\text{C}$  in a dry nitrogen environment to minimise radiation damage as it is foreseen to employ the SCT-devices for the whole LHC operation period of ten years.

**Spacepoint Formation** The SCT detector will provide up to four precision measurements. In principle it follows the same formation steps as the pixel measurements, however the last step is different: Same is that during BS decoding raw data are converted into RDOs and in the clustering step neighbouring strips are formed to cluster objects. However here, the “local-to-global” transformation can not be performed. Instead, the spacepoints are formed out of cluster pairs of opposite sides of one module or from separate modules which overlap in  $\eta$  or in  $\phi$ .

### Transition Radiation Tracker - TRT

The transition radiation tracker is a gaseous detector. It is the outermost tracking station of the inner detector and will provide charged particle information from drift tube cham-

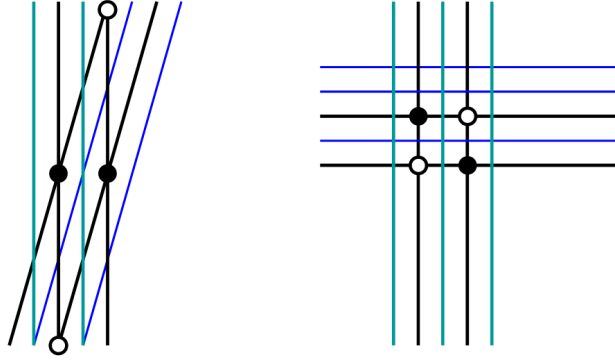


Figure 3.6: Ghost spacepoints in silicon strip detectors. Thanks to a very small stereo-angle the impact of ghost hits can be reduced in pattern recognitions. In blue and green are the strips shown for a front- and back-side of a SCT module. The black lines indicate a hit on these strips. Assuming the black dots as true spacepoints, the white dots will be also registered as spacepoints, though they are ghosts. From the right picture one can imagine many more possibilities of ghost spacepoints (only few strips are indicated).

bers also for the complete inner detector acceptance. Additionally it features transition radiation detection for separation of high energy electrons from pions.

The TRT consists in total of 370,000 carbon fibre drift tubes which are also called “straws”. It has barrel and endcap regions. The barrel is divided in three radial sections which is shared by 50,000 drift tubes arranged parallel to the beam-line. The endcap regions consists of nine wheels on each side holding the 320,000 tubes lying perpendicular to the beam-line [18].

Each such straw has a diameter of 4 mm, a  $30 \mu m$  thick tungsten wire and is filled with a gas-mixture of 70 % Xe, 30 %CO<sub>2</sub> and a small amount of O<sub>2</sub>. The spatial resolution will be comparatively low with  $170 \mu m$ , however one track contributes on average with 36 detector hits called “drift-circles”. By traversing a drift tube a charged particle ionizes the gas creating ions along its track. These ions will drift in an high electric field to the respective electrode where they give signals in the order of arrival. To produce transition radiation from electrons, “radiator” foils<sup>6</sup> are placed in between the drift tubs. Two independent signal thresholds can then be surmounted, a lower one providing position information, and a higher one if transition radiation is emitted.

For the minimum bias trigger the information of this sub-detector has been entirely omitted. Additional track information to improve the track quality is not necessary for these kind of events. Likewise the timing constraints of the trigger would barely allow for complete read-out of additional 420,000 channels. The following sub-systems were also not considered in the minimum bias studies for similar reasons and are therefore rather briefly described. Instead, a dedicated experimental setup is described following a complementary trigger approach to the one studied in this work.

<sup>6</sup>They are made of polyethylene and polypropylene.

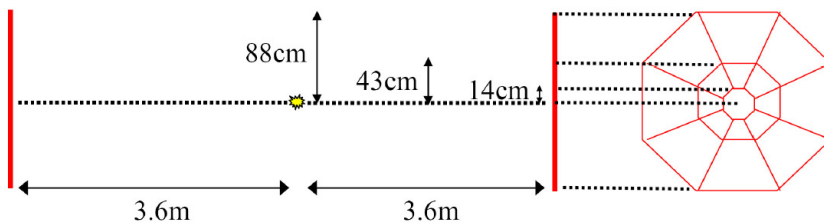


Figure 3.7: Planned deployment of the MBTS (red). The yellow spot represents the IP while the horizontal line is the beam-axis. The scintillators are mounted on the front-face of the LAr endcaps of the hadronic calorimeter and provide a total acceptance of  $2.12 < |\eta| < 3.85$ .

### Minimum Bias Trigger Scintillators - MBTS

This setup consists of two wedge shaped plastic scintillators each one identically constructed. They are divided in two sections in  $\eta$  and each of them is segmented in 8 equal pieces of  $\phi$ . In total there are 32 counters,  $2 \times 8$  for each span per scintillator with an acceptance of  $2.83 < |\eta| < 3.85$  for the inner span and  $2.12 < |\eta| < 2.83$  for the outer span. The scintillators are each situated at the front-face of the LAr endcap at  $z = \pm 3.6$  m. They are 3 cm thick and have an inner radius of 14 cm and an outer radius of 88 cm. A sketch in figure 3.7 illustrates their deployment.

The material of which the MBTS consist is a blend of poly-styrene doped with a fluorescent agent in order to detect efficiently minimal ionizing particles (MIP). Due to the expected radiation damage a degradation of the scintillation light output by a factor of two should be allowed. The emitted light is collected by wavelength shifting optical fibres that are connected to photo-multipliers and read-out electronics of the hadronic calorimeter. Finally the signal is transported via a 80 m twisted pair cable to LVL1 processors. It was measured that the inner section produces 1.4 times more photoelectrons as the outer section [28]. Furthermore, it was shown that the probability that no charged particle will pass through any of the scintillators is 0.3 % for a luminosity of  $\mathcal{L} = 4 \cdot 10^{32} \text{ cm}^{-2}\text{s}^{-1}$ . However, the mean deposited energy of a MIP in one of a MBTS around 7 MeV while the trigger of tile towers<sup>7</sup> of the calorimeter (see hadron calorimeter) is designed for energy deposits of several GeV's. But results of first testings showed that the tile calorimeter towers are still sensitive enough [29]. The trigger strategies are further detailed in chapter 5.

### 3.2.2 Calorimeter System

Around the inner tracking system the calorimetric system is placed. It provides high precision measurements of electrons, photons, jets and missing transverse energy. An incoming particle loses energy by scattering on material and produce a “shower” of particles such that they are ideally completely stopped and absorbed within the fiducial detector volume. ATLAS uses the *sampling* method for electromagnetic and hadron calorimetry where active material is interleaved with passive absorber material. The operation in the environment of high multiplicity events resulted in two different techniques that are employed for the calorimeters; liquid argon (LAr) and tile technique. LAr is used for the inner parts of calorimeters, in the electromagnetic barrel and endcap region as well as in the hadronic

<sup>7</sup>A tile tower is a read-out unit in the hadron calorimeter.

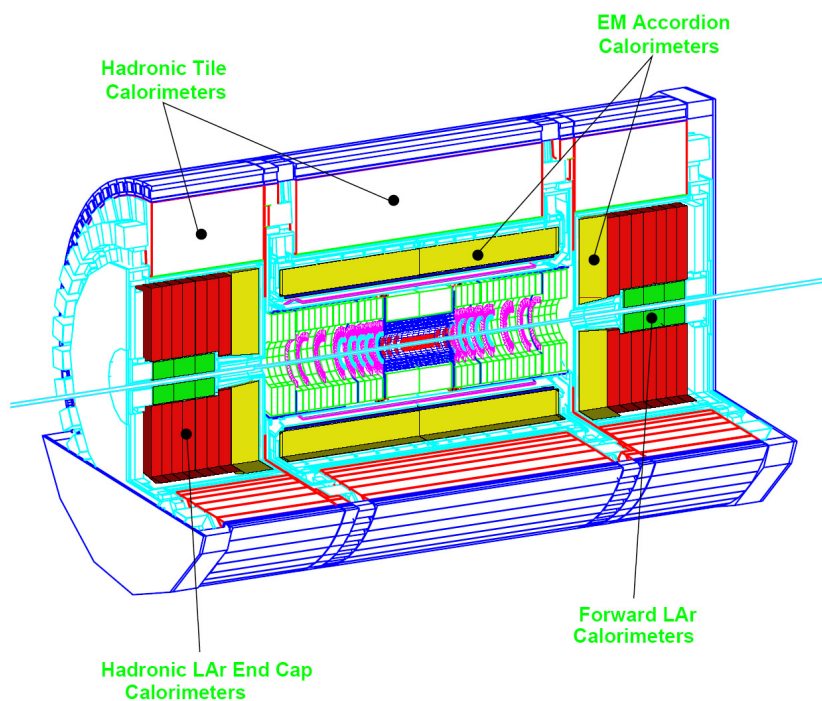


Figure 3.8: Calorimetric system in ATLAS. In yellow the electromagnetic calorimeters based on the LAr technique are shown. Also part of the hadron calorimeter uses LAr technique (red). For larger radii with respect to the beam-line the hadronic calorimeter is made of iron tile scintillators.

endcaps (HEC) and forward calorimeter (FCAL). At increased radial positions  $> 2.2$  m the (less expensive) iron tiles are used for hadronic calorimetry in the barrel and extended barrel above the calorimeter endcaps. The tiles lie in the  $r - \phi$  plane, wavelength shifting fibres running radially collect the light from the tiles along their two open edges. Read-out cells are then organized in tile towers and defined by grouping together the fibres to one photo-multiplier such that three dimensional segmentation is obtained. An overview of the single components is given in figure 3.8. LAr as active medium is used together with lead in an accordion-like geometry for the electromagnetic sampling covering  $|\eta| < 3.2$ . For the HEC copper is used as absorber material covering a region of  $1.5 < |\eta| < 3.2$ . The FCAL covers up to the acceptance limit with  $3.2 < |\eta| < 4.9$  and as showering material copper was chosen for the inner section and tungsten for the outer ones. The Tile Calorimeter incorporating the largest massive part of the calorimeter system covers the central part with  $|\eta| < 1.7$ . It consists of steel plates alternating with plastic scintillator tiles in a “sandwich-structure”. The barrel and the endcaps of the electromagnetic calorimeter are segmented in three different regions “samplings”. Sampling 1 has a very fine granularity of  $\Delta\eta \times \Delta\phi = 0.003 \times 0.098$  and a depth of  $4.3 X_0$ <sup>8</sup>. Sampling 2 has a granularity of  $0.025 \times 0.025$ , thus about eight times lower, and a depth of  $16 X_0$ . Here most of the particles deposit their energy. The back sampling provides a coarse granularity of  $0.05 \times 0.0245$  and is  $2X_0$  deep. In this part tails of the showers are measured which extend the middle sampling. Otherwise one can differentiate already electromagnetic from hadronic showers, as hadronic showers deposit here more energy. The tile calorimeter is segmented in four regions. They have two cell granularities, a finer one for inner parts  $0.1 \times 0.1$  and for the outer part  $0.1 \times 0.2$ . More details can be found in [17]. For a detailed and more recent description, see e.g. [6].

### 3.2.3 Muon Spectrometer

In many interesting physics signatures high  $p_T$ -muons are involved. Therefore, they should be accurately measured and used for triggering. For this purpose in ATLAS a complex muon spectrometer is built instrumented with precision and trigger chambers. They operate in an toroidal magnetic field of 4 T produced by the barrel toroid covering  $|\eta| < 1$  and two endcap toroids for  $1 < |\eta| < 2.7$ . Each of the toroid parts is constructed of eight of the prominent coils located radial-symmetrically around the beam-pipe and will be operated with 20.5 kA. The trigger chambers are Resistive Plate Chambers (RPC) and Thin Gap Chambers (TGC) based on multi-wire proportional chambers providing trigger decisions within about 10 ns, thus well within the LHC clock. The precision chambers are Monitored Drift Tube (MTD) and Cathode Strip Chambers (CSC). Their signal is built up in 300 ns and 30 ns respectively. The data are directly stored in memory buffers and only retrieved upon trigger request. The CSC are also multi-wire proportional chambers segmented with read-out cathodes, providing a resolution of  $60 \mu m$ . The MDT are multi-layers of drift tubes giving spatial resolution of  $80 \mu m$ . See figure 3.9 for an overview of the arrangement of the chambers.

The muon spectrometer with the toroidal magnetic system is certainly one of the most impressive constructions in ATLAS. However, it was not further considered in this work as specifically muons were not relevant. Details can be found in [19] or [20].

---

<sup>8</sup> $X_0$  = radiation length = mean distance up to which the particle loses its initial energy to  $1/e$ .

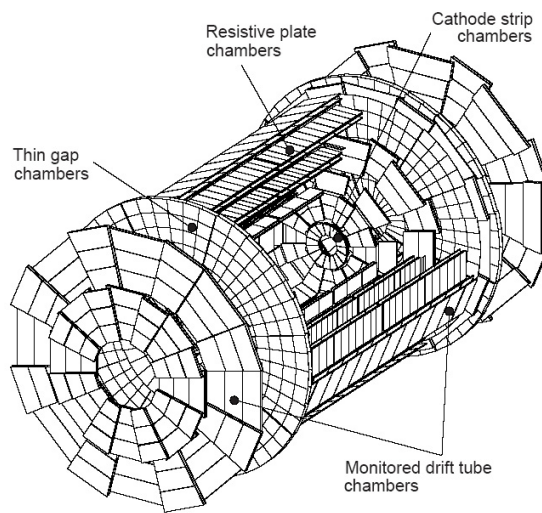


Figure 3.9: Muon Spectrometer. Shown are: Monitored Drift Tube (MTD) and Cathode Strip Chambers (CSC) as well as Resistive Plate Chambers (RPC) and Thin Gap Chamber (TGC).

## Chapter 4

# Trigger and Data Acquisition System

### 4.1 Motivation

The LHC is designed to cope with a bunch crossing rate of 40 MHz. At its nominal luminosity  $\mathcal{L} = 10^{34} \text{ cm}^{-2}\text{s}^{-1}$  and total cross-section of  $\sigma_{tot} \approx 100 \text{ mb}$  roughly 25 collisions per bunch crossing are expected. Assuming a size of such an event to be  $\sim 1.5 \text{ MB}$  large one will have to deal with  $\sim 1.5 \text{ PB/s}$  data volume. It is impossible to store all the produced data. From the physics point of view there is also no need in keeping each pp-interaction as most of them are already well known from previous experiments. As mentioned in chapter 2 the search is made for *rare* events and the trigger must therefore be highly selective. The trigger system is one of the biggest challenges in ATLAS. It must provide a suppression factor of more than  $10^5\%$  to achieve a recordable rate of  $\sim 200 \text{ Hz}$ . Two main concepts are pursued to face this task: *Step-wise* and *seeded* event selection. The first basic concept deduces the decision time by using a *step-wise* design of the trigger system allowing an early rejection of uninteresting events. Seeded selection means only data in so-called *region-of-interests* are processed for deriving a trigger decision. In such a specified detector region merely a small fraction of about 2 % of the whole event data are processed first and thus reduce the amount of data transfer which enables also to produce a fast trigger decision.

In ATLAS there will be three trigger levels realizing this strategy: level 1 (LVL1), level 2 (LVL2) and the event filter (EF) as third trigger level. Their main purpose during the selection is to ensure to make a *right* selection covering any unknown physics processes. On the one hand the trigger thresholds must be as generic as possible not to reject potentially new physics but on the other hand one has to identify very fast the content of each event. A more detailed description of the trigger system followed by an explanation of the event selection is given below.

### 4.2 The 3 Trigger Level- and Data Acquisition System

#### 4.2.1 First Trigger Level - LVL1

The first trigger level is hard-ware based and has to reduce the event rate below 75 kHz (or 100 kHz as foreseen in the LHC upgrade) within a latency of  $2.5 \mu\text{s}$ . The Level-1 trigger

system can be divided in three LVL1 sub-systems: The calorimeter trigger L1 Calo, that receives data from both calorimeters, the muon trigger L1Muon, processing information of the resistive plate chambers (RPC) and thin gap chambers (TGC), and the central trigger processor CTP. The L1 decision is based on multiplicities of physics **objects**<sup>1</sup> for electron/photons,  $\tau$ 's/hadrons, jets and muons as well as for flags of total missing transverse energy and total transverse jet energy. These **objects** are triggered by  $e/\gamma$ -,  $\tau/h$ -,  $\mu$ -, energy- and jet-triggers respectively and taken as standard input for the CTP. Additional input is defined for minimum bias events triggered by Minimum Bias Trigger Scintillator (MBTS, see section 5.2), for cosmic events and for special CTP-internal triggers. In total there are twelve internal triggers, two random triggers with different trigger rate, two prescaled clocks and eight group triggers. A group can be defined e.g. as filled bunches using beam pick-up monitor signals. The prescaled clocks are periodic triggers taking only bunches with constant distance in between. Also combinations are possible. The approach for triggering minimum bias events independently from MBTS will use one of the random triggers combined with a trigger on filled bunches. These additional triggers serve commissioning and monitoring reasons and are an important tool to produce redundancy in order to check the systems functionality. The random based minimum bias trigger will be outlined in the next chapter.

The CTP forms the level-1 accept (L1A) from external and internal trigger input according to a level-1 *trigger menu*. Such a menu consists of maximal 256 *trigger items* that are combinations of one or more conditions set on the trigger inputs. If e.g. MU6 symbolizes a condition on a muon to possess at least a transverse momentum of 6 GeV then 1MU6 can define a LVL1 trigger item that *one* such a muon must be measured. Each trigger item possesses a bit mask, a prescale factor which is needed in order to suppress very high rates of some physics **objects** and a priority (can be set to LOW or HIGH) for dead-time that will be created by the CTP. Within 100 ns a logical OR-combination of trigger items are formed representing the L1A.

Each event is kept in pipeline memories of the detector front-end electronics. Detector-specific readout drivers (RODs) combine the large number of readout channels to about 1600 data fragments and each fragment is sent to an individual readout buffer (ROB). Only data for events selected by the LVL1 is transferred to these ROB's being part of a larger unit, a so called readout systems (ROs).

After every L1A generation information is sent from the calorimeter and muon trigger to the level-2 Region-of-Interest-Builder (RoIB). An RoI is a geometrical region in the detector in  $(\eta, \phi)$  and contains additionally a bit pattern indicating which threshold was passed. The CTP also sends information to the read-out and data acquisition system containing data for several bunches for debugging and monitoring purposes.

#### 4.2.2 High Level Trigger - HLT

The HLT system is comprised of LVL2 and EF which are software triggers running on dedicated farms built of standard PC's and interconnected by ethernet network. At LVL2 the basic concept is to combine high rejection power with fast and rather rough precision algorithms consuming modest CPU in LVL2. At the EF modest rejection power

---

<sup>1</sup>They are objects in the sense of C++.

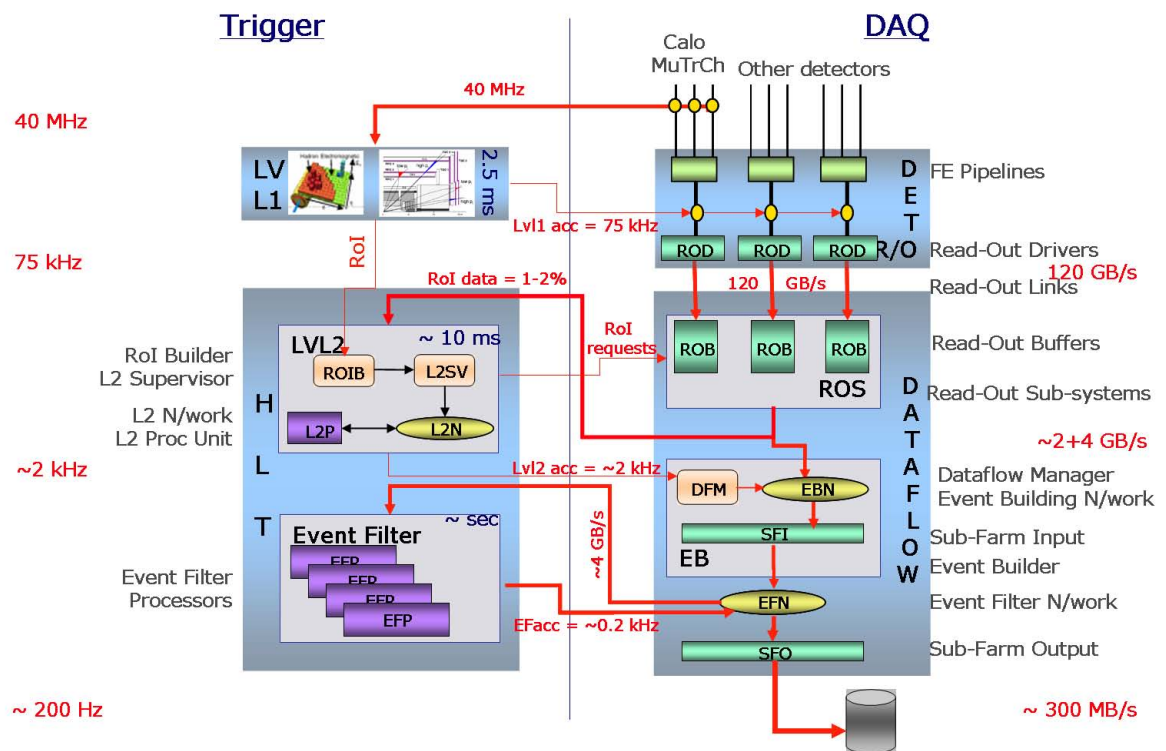


Figure 4.1: Overview of the ATLAS Trigger and Data Acquisition System. It shows functional elements and their connections, see text for explanations. This figure is taken from [21].

with higher precision and therefore slower algorithms are employed using more extensive computing power.

**Second Trigger Level - LVL2** Signals from LVL1 sub-systems are sent to RoIBs which will run with the same rate as LVL1. This information is passed to level-2 supervisor computers (L2SV) which assigns each event a level-2 processor unit (L2PU) running on an level-2 processor (L2P) where LVL2 event selection algorithms are executed. Only data associated with an RoI are requested via the dedicated level-2 network (L2N) from ROS. After processing RoI data the L2PU produces summary information and adds the LVL2 decision which represents the LVL2 result. During the processing time more event fragments can be requested from the ROS. The LVL2 decision is sent back to L2SV which forwards it to the data flow manager (DFM). In case an event is rejected the DFM passes the decision to the ROS such that the event can be removed from read-out buffers (ROB). In case of a positive decision the event-building operation is initiated by the DFM. The total processing time to produce a LVL2 decision is limited to about 10 ms and the LVL1 rate is diminished to about 1 kHz.

For the **event-building process** a sub-farm input (SFI) is allocated for fragments of each accepted event. In SFI the event is build in its memory and signalizes a correct assembling to DFM where they are buffered to serve further processing on EF. A switching event building network (EBN) links ROS, SFI and DFM to increase efficiency as the network enables concurrent event building.

**Event Filter - EF** The EF comprises several thousand farm processors (EFP) each one running a EF data flow control program (EFD) that receives a complete event “seeded” from SFI. The EFD application makes in principle the whole event available on processing tasks (PT) where EF event selection software is executed. The EF algorithms are guided by the LVL2 result and will only process data from an RoI but with full access to calibration and alignment data as well as with a more detailed detector material description. If a PT has finished processing an event it requests a new event from an SFI. In case of an accepted event data generated during processing on the PT is appended to the raw event which is then classified and transferred to sub-farm output buffers (SFO). Completed events are accessed by the mass storage system for permanent storage. Analogue to LVL2 an EF-network (EFN) interconnects SFI, SFO and EFP. The overall processing time on the EF is about 1-2 seconds resulting in a output rate of 100-200 Hz.

The TDAQ control system known as the Online Software system is responsible for configuration, controlling and monitoring of the processes but excludes processing of data itself as well as management and transport of physics data. For further information on the online software system as well as TDAQ see [22].

### 4.3 HLT Selection

The event selection is a very sophisticated procedure though in principle there are two fundamental concepts which reign the design of the HLT selection. Firstly, HLT algorithms are *seeded* by the results of the previous level in order to reduce data transfer and produce a fast decision. The seed is given in form of the already above introduced region-of-interest

in the detector where conditioned activity has been measured in a thereby specialized detector area. The second concept is to process the event *step-wise*. The trigger decision is initially based on coarse information but then refined at each further processing step by accessing higher granularity of more sub-detectors. At the end of each step a new decision is made after algorithmic work is performed on the present information allowing for the employment of algorithms with high rejection power first and enabling early rejection of unwanted events. The Steering provides the necessary functionality framework for such a concept in which algorithms can be plugged in. They communicate via restricted interfaces such as trigger elements (in which the result of the algorithms is incorporated) or error codes and its task is e.g. starting the execution of algorithms, selecting and combining trigger elements (TEs) whereas the raw data processing is performed by the algorithms. As this thesis aims at a development of a minimum bias trigger the basic architecture design for such an implementation is described below.

**Derivation of a Trigger Decision** The configuration of the HLT trigger menu comprises *trigger chains* consisting of physics *signatures* from which a list of signatures or a *signature table* can be defined for each processing step. Each trigger chain provides one signature at each step. Only if at a given step N at least one signature being a logical combination of trigger elements is fulfilled, the event is passed to the next processing step N+1. Otherwise the event is stopped and a new event can be accepted, thus the trigger decision is defined in terms of trigger chains. The chains must be configured such that at N+1 each signature must correspond to exactly one signature at N. A simplified case of trigger chains and signature tables is shown in figure 4.2. As a first approach a trigger chain is defined by a list of signatures. However, signatures can also be shared by different trigger chains which will lead to split chains. Splitting is only possible at a transition to the next trigger level and in one direction only towards higher processing steps but not vice versa. The reason is that with chains just splitting into the higher trigger direction and only at the trigger level transitions one can determine trigger efficiencies with the help of the last signature. Otherwise the system becomes unpredictable e.g. due to dependencies that can not be traced back.

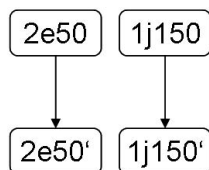


Figure 4.2: Example for signature tables (horizontally) and two trigger chains (vertically). In case of the left trigger chain a signature consists of two equal trigger elements of an electron with at least  $p_T \geq 50$  GeV. The refinement is indicated by '.

**Refinement of Trigger Elements** Another part of the configuration is to describe a *sequence table*, a list of algorithms necessary in order to refine event characteristics e.g. at step N there is a trigger element TE, a *sequence* refines it to TE'. One sequence consists of certain refinement algorithms, usually feature extracting algorithms (FEX) extracting

quantities from raw data and hypothesis algorithms (HYPO), testing if certain thresholds have been passed. In general the refinement is based on a LVL1 RoI or -in terms of the steering language- the corresponding LVL1 trigger item which is normally written in capital letters, like EM50, symbolizing an electromagnetic RoI having passed the 50 GeV transverse momentum threshold. A sequence needs one trigger element as input and creates one output trigger element (or deactivates a trigger element which is dependant of the HYPO-result). According to the active trigger elements the steering decides which algorithms are run at the next step, therefore unique names of trigger elements must be ensured to identify the sequence. Also the trigger elements link a sequence table with the signature table as a sequence algorithms perform work on trigger elements and signatures are a logical combination of trigger elements. More details like an complete configuration example can be found in [24].

For the development of a minimum bias trigger chain non-standard algorithms are needed as the event will not be analysed in a certain RoI but for the whole inner detector region (see chapter 5.3). Therefore so called unseeded algorithms will be employed.

**Unseeded Algorithms** This type of algorithms was originally developed for B meson decay scanning at least half of the inner detector region for b-tagging. Nevertheless they are also suited for minimum bias event selection. *Unseeded* means that the algorithm is started without requiring an input TE but by the mere existence of corresponding signatures at the processing step before. However, they do create an output TE which can be combined to signatures with other TEs. An unseeded algorithm for minimum bias events must be called only once per event as it is not RoI based.

## 4.4 Trigger Performance Targets - Technical Information

The trigger decision including the data retrieval should as mentioned before not take longer as  $\sim 10$  ms for LVL2 and  $\sim 1$  second for EF which was meant to be realized by 8 GHz CPU's. This is the initial target as described in the TDR [22]. Since, the target has somewhat changed and the performance of a 8 GHz CPU will be provided by 2-3 CPU cores with the same throughput but with double latency as initially expected such that the target times are now 20 ms at LVL2 and 2 seconds at the EF. However the relation between the times consumed by individual algorithms and the averaged time to make a trigger decision is not trivial. For each step several issues have to be taken into account: the rejection factor, the RoI multiplicity for RoI based selection and overheads in the steering as well as in data retrieval at LVL2. Rejection at an earlier step as will lead to more time for the subsequent level as algorithms are called less frequently. The timing measurement for the minimum bias concept were performed on an 3 GHz machine as recommended which takes into account the new trigger performance targets [23].

## 4.5 Event Data Model

The ATLAS software has to incorporate detector specific information provided by the TDAQ system and combine them such that trigger decisions can be derived and understood also afterwards in the analysis. One major step has been achieved in order to retrace trigger decisions by the employment of an *Event-Data-Model* (EDM) [25], a computing

model for ATLAS software to ensure common tools and physics data objects (physics objects provide information of particle tracks e.g. clusters in the one silicon detector, momentum, etc). The EDM aims also at simple maintenance for long time periods and especially consistent software all across the detector sub-systems. Moreover, the EDM uses common software in online data processing and offline reconstruction: Algorithms elaborated for the offline analysis have been adapted for trigger utility able to work also RoI based. The commonality between trigger and offline processing concerns the structure of the EF, LVL2 algorithms in the computing model, however LVL2 and EF algorithms use different base classes and can therefore not be easily combined. Nevertheless this represents already a huge advantage. Thereby one avoids e.g. redoubling of code and multiplication of physics data objects. Instead, the formed object are shared objects between various sub-detector systems. One of the main elements representing the EDM is the *Common Track* class whose basic concepts are described in 5.4.2. It provides e.g. standard definitions of track parameters and common interfaces which are tools to perform the data analysis. Very generally it represents a measurement on a surface in the inner detector, providing thereby two-dimensional information. Throughout the design of the EDM one emphasizes the separation of the two types of data within the data flow: persistent and transient data. While transient data exists for the lifetime of an event or run and serve technical needs, persistent data contain the physics and are therefore stored persistently. A detail class description defined in the EDM can be found in [26].

## Chapter 5

# Development of a Minimum Bias Trigger

### 5.1 Motivation

LHC is designed to reach a luminosity of  $\mathcal{L} = 10^{34} \text{ cm}^{-2}\text{s}^{-1}$  and a center of mass energy of  $\sqrt{s} = 14 \text{ TeV}$ . The bunches collide every 25 ns leading to an event rate of 40 MHz. The collision rate is with 1 GHz much higher as around 25 collisions are expected per bunch crossing. They will lead to pile-up of interactions in the detector and produce more particles themselves which are almost all low  $p_T$  particles (see section 2.3). As no theory exists to describe soft interactions such that their rate can be predicted at different energy scales, these kind of processes are an interesting study object themselves. But more important is that the detector must be understood in the presence of this *pile-up* in order to identify correctly the physics processes. At TEVATRON minimum bias events were measured and used to tune simulation models employed for cross-section predictions, especially for those energies LHC will reach. However, this is not sufficient for cross-section predictions at higher energies. The strategy at ATLAS is hence to study minimum bias events at low luminosity to avoid overlapping collisions. This can be used to estimate their rate at higher luminosity. For this purpose two dedicated triggers are being developed, following two independent strategies to select these events. One uses trigger scintillator signals at LVL1 and possibly further processing on HLT. This will be realized by two Minimum Bias Trigger Scintillators (MBTS). The alternative approach will employ a random trigger at LVL1 and perform a track based selection on HLT. Studies necessary to develop such a trigger based on random selection at first stage and inner detector signals are the subject of this thesis and described in this chapter.

After depicting the trigger strategies of the MBTS, the concept of the random based track trigger is presented in section 5.3. In this context several strategies are discussed. Primary background sources as empty and beam-gas events were investigated in order to achieve an efficient rejection which is subject in section 5.5 before ATLAS trigger pattern recognition algorithms are introduced in a general way in section 5.4 concentrating on the LVL2 Inner Detector Scan algorithm IdScan and the EF tracking code NewTracking. They were used for the minimum bias trigger studies. In section 5.6 the results for feasibility studies are presented focusing on time consumption of the trigger algorithms.

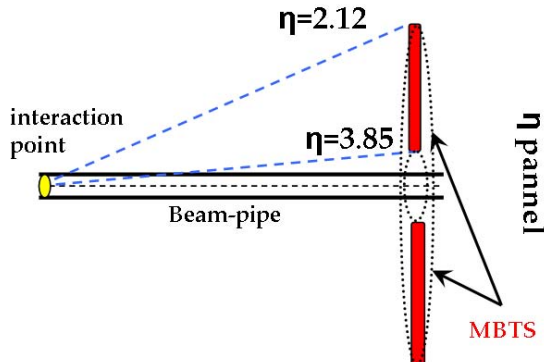


Figure 5.1: Sketch of the acceptance of Minimum Bias Trigger Scintillators (MBTS). The event selection is restricted to events with tracks with  $2.12 < |\eta| < 3.85$ .

## 5.2 Minimum Bias Trigger Scintillators - MBTS

MBTS are planned to be employed in the first 3-4 months of running at low luminosity  $\mathcal{L} = 10^{31} \text{ cm}^{-2}\text{s}^{-1}$ . As they will be strongly affected by the radiation damage their lifetime is relatively short. The experimental setup was described in section 3.2.1.

### 5.2.1 Trigger Strategies of MBTS

Several strategies are being investigated. The most favourable trigger concept to employ the MBTS trigger signals at LVL1 with application of a very low signal threshold which will also lead to a high noise rate. Therefore, a software based verification on the HLT in order to suppress the noise is needed. The advantage is that by a lower noise threshold less bias is introduced. For the HLT verification it is foreseen to replicate the LVL1 results on HLT and use the high-gain output instead of the low gain signal as a much better signal-to-noise ratio can be obtained as the use of the high-gain output is not directly feasible at LVL1. Other trigger strategies such as an application of an increased threshold but also a low hit-requirement or even an application of higher hit-requirements in order to suppress significantly noise rate are rather disfavored due to a stronger bias introduction. Nevertheless this is under investigation as well as several other possibilities. Studies e.g for equal hit-requirement were performed [28], but other ideas such as only requiring a total hit multiplicity are still to be studied in order to favor a concept [30].

## 5.3 Concept of a Random based Track Trigger for Minimum Bias Events

The scenario for which this minimum bias trigger is developed is the start-up phase of LHC data taking. The rate of interactions will be rather useful in the case the luminosity grows to  $\mathcal{L} = 10^{31} \text{ cm}^{-2}\text{s}^{-1}$ . Generally, the aim of this phase is to achieve final tunings for HLT algorithms and selection thresholds. Most likely, a large part of bandwidth will be assigned to minimum bias events allowing for record of single pp-interactions events.

Presumably the trigger bandwidth will be about 50 % [31], but this is still under discussion. Estimating the probability to have one interaction per event can be calculated by the ratio of the reaction rate  $R$  and the collision frequency of a proton bunch  $f$ :

- The reaction rate  $R$  is given by the cross-section  $\sigma$  and the luminosity  $\mathcal{L}$ :  $R = \sigma \cdot \mathcal{L}$ . Assuming a total cross-section of about  $\sigma_{tot} \approx 100$  mb  $R$  becomes  $R \approx 1$  MHz.
- The collision frequency  $f$  of a proton bunch is the inverse bunch pitch  $f = 1/75$  ns  $\approx 13$  MHz

Thus the probability of one pp-interaction per bunch crossing is around 10 %.

### 5.3.1 Trigger Strategy

The trigger strategy is outlined for the calculated pp-interaction probability, but also others for lower interaction probabilities are shortly discussed.

Obviously it is important to minimize the bias in the event selection for minimum bias events. The definition of possible sources of bias depends on the way the event is triggered and does not mean to process only coarse trigger informations if more precise data provides a significant gain of information. In order to introduce no bias at the first selection step a random trigger will be used. This can be realized by a combination of a random trigger and a trigger on filled bunches at the first trigger level LVL1. Both triggers are internally implemented in the central trigger processor CTP as described in the preceding chapter. Further, the event will be passed to the higher level trigger bypassing the second trigger level directly to event filter farm where processing is performed in mainly two steps. In the first selection step empty bunch-crossing events are rejected. Therefore, all the hits of the inner detector silicon sub-detectors will be processed. TRT information will be omitted for reasons of time constraints as already for the silicon detectors up to 86 millions channels have to be read out. Moreover, the TRT serves to improve the quality of the measured track from silicon detectors. For minimum bias events this is irrelevant. Track reconstruction is hence the next step to be performed which should reject most of other background events e.g. due to beam interactions with residual gas. These beam-gas events are treated as background in order to get pure minimum bias events. In other possible trigger applications beam-gas events can be interesting for different background studies. Such a trigger is not considered here but these events can be obtained additionally to minimum bias events by setting different threshold tunings of the random based track trigger. This underlines the aim of this thesis to develop a flexible trigger that enables us to react on different needs.

The minimum bias algorithms will not work RoI based like most of the other triggers. In contrast to the *seeded* event processing as described in the chapter 4, minimum bias event data will be processed in a *full scan* mode, making use of the total inner detector acceptance of  $|\eta| < 2.5$ . As measurements of the whole silicon detectors are used, i.e. of pixel and SCT detector, minimum bias algorithms will run most likely on the event filter farm as time constraints are looser. The LVL2 farm is omitted which does not exclude to possibly make use of LVL2 algorithms, one can run these without any restrictions also on the EF <sup>1</sup>. The reason for omitting rejection power on LVL2 is that it simply might not be needed: Having as estimated above an event rate of 13 MHz one needs to down-scale

---

<sup>1</sup>This should be a feasible configuration in the steering by loading required libraries to the respective farm.

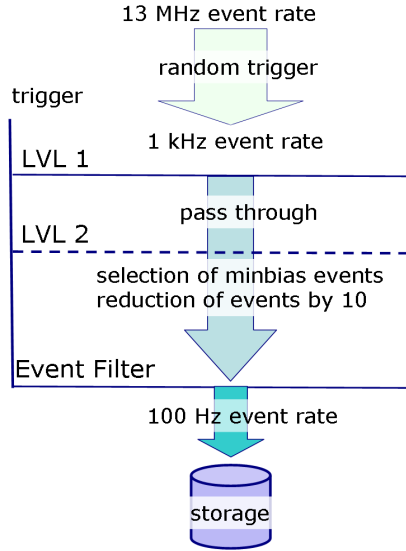


Figure 5.2: Concept of the random based track trigger for minimum bias events: At the first stage at LVL1 a random trigger selects with a rate of 1 kHz, that are passed through LVL2 and processed on the third trigger level using its maximal processing capacity of 1 kHz to obtain a storage rate of 100 Hz.

the event rate to 1 kHz. Supposing the minimum bias algorithms stay within the time budget of the EF latency of 1 s one will be able to run with the maximal processing power of the EF and the recording rate corresponds to the minimum bias output rate of about 100 Hz. The rejection factor of 10 at the EF stage fits thereby precisely to the probability of a single pp-interaction: In 1 kHz we have in 10 % of it a pp-interaction, thus 100 Hz which corresponds exactly to the (assumed) recording rate. This concept is illustrated in figure 5.2 showing a sketch of the trigger levels with corresponding event rates. For scenarios with lower pp-interaction probability one will need definitely LVL2 in order to obtain the same minimum bias output rate. One would then reject empty events at LVL2 and perform the track based selection at the EF. The bottleneck of this trigger strategy is the time of data retrieval at this stage as it is not foreseen to have to whole event data available at LVL2.

The approach employing a random based event selection represents the major advantage compared to the experimental setup of the MBTS. Another one is due to the “lifetime” of the random based track trigger which is not determined by any material damage. Thereby, it will be possible to employ this trigger as long as it is needed also at higher luminosities to study several overlapping interactions. One can also imagine a combination together with MBTS signals for empty event rejection. Anyhow, both triggers follow a different approach and are complementary to each other e.g. in acceptance coverage and for trigger efficiency determination.

It is to be decided on which trigger level the minimum bias event selection will take place and which trigger strategy to follow. Therefore, track reconstruction algorithms for LVL2 and EF were studied. In the next section two such track reconstruction algorithms are presented starting with the LVL2 algorithm IdScan that is followed by a description

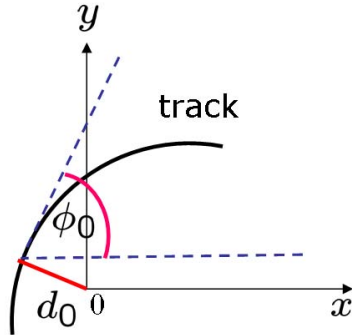


Figure 5.3: Illustration of perigee parameters  $d_0$  and  $\phi_0$ . The longitudinal impact parameter  $z_0$  is the z-coordinate of the perigee.

of the EF pattern recognition algorithm NewTracking (NewT). Studies on background rejection efficiencies are all based on these algorithms.

## 5.4 Trigger Pattern Reconstruction Algorithms on LVL2 and EF

LVL2 track reconstruction algorithms are much faster in a first data evaluation performing rather crude pattern recognition. On the second trigger level two of such track reconstruction algorithms following different strategies were developed aiming both on a fast and efficient performance: Inner Detector Scan (IdScan) and SiTrack. They have similar reconstruction efficiencies at high  $p_T$  values. For low  $p_T$  physics the performance in a comparable setup of SiTrack and IdScan has not been investigated yet. Studies have been merely performed with IdScan as SiTrack was directly based on Monte Carlo simulation which at the time of the start of the studies. MC dependence for unpredictable processes seemed not appropriate for minimum bias event selection. However, meanwhile the strategy of SiTrack has changed and it does not directly depend of Monte Carlo simulation anymore. It could be now at least equally suitable for low  $p_T$ -track reconstruction as IdScan [32].

After introducing the naming convention of track parameters in ATLAS IdScan is described in more detail with the emphasis on topics relevant for this thesis.

### Naming Conventions in ATLAS

**Perigee parameters** are defined for the closest approach (perigee) of a track to the beam line. The projection of the distance of the perigee to the transverse plane, that is same as the (x,y)-plane in cartesian or  $(\phi, \rho)$ -plane in cylindrical coordinates, is the transverse impact parameter  $d_0$ . The angle  $\phi_0$  lies as well in the transverse plane and is the angle between the tangent of the perigee and the x-axis which is the same as  $\phi - 90^\circ$ , where  $\phi$  is the usual definition of the azimuthal angle. These two parameters are illustrated in figure 5.3. The third perigee parameter is the longitudinal impact parameter  $z_0$  being the z-coordinate of the perigee.

### 5.4.1 LVL2 Track Reconstruction Algorithm IdScan

A common feature of all reconstruction algorithms is to form so called spacepoints from silicon sub-detectors (spacepoint formation is described in section 3.2.1) and out of these measurements tracks. Additionally  $\sim 36$  drift-circles are used to extend the track to the TRT.

IdScan makes use of spacepoints and drift-circles using measurements from pixel, SCT and TRT detector. It consists of four main parts which will be described in more detail: I. zFinder, II. HitFilter + GroupCleaner and III. Track-Fit and IV. Extension of the track to TRT [35].

An essential part of IdScan is the **zFinder** which provides the z-position of the pp-interaction usually incorporating a high  $p_T$  signature [34]. Thereby, the number of track candidates considered for the following steps are significantly reduced which enables IdScan to be run as an LVL2 trigger algorithm. A general principle for such a mechanism -also known as Hough-Transformation- is to do the following: Firstly, the  $(\rho, \phi)$ -plane is divided into small pieces of equal sized  $\phi$ -slices. Then, after spacepoint formation, the spacepoints are grouped for each such a  $\phi$ -slice. Pairwise coupled their interpolation is extrapolated to the z-axis using the assumption that within a constant solenoidal magnetic field of 2 T helix trajectories are straight lines within the  $\rho$ -z projection. This assumption holds for high- $p_T$  tracks. The intersection with the z-axis is filled in a histogram and a peak in this z-histogram will indicate the most probable value of the z-coordinate. The weighted mean of the bin containing the peak and two neighbouring bins is taken as the z-coordinate of the vertex. One expects this as spacepoints from tracks with the same primary vertex will give a rise of entries. The resolution of the z-coordinate is determined by the width of the z-bin. For RoI's this width also scales with  $\eta$  of the size of the RoI usually given in  $\Delta\eta \times \Delta\phi$ . In the present study it was taken independently from  $\eta$  as constantly the whole  $\eta$  range is covered in the minimum bias event section.

The original motivation of having small  $\phi$ -slice widths is to reduce possible combinatorics of detector hits originating from pile-up or noise. This is visualized in figure 5.4: Spacepoints coming from a high- $p_T$  particles lay rather in a single  $\phi$ -slice whereas spacepoints created by a low  $p_T$  track -that are considered in the original conceot of IdScan as *background*- are distributed over several of neighbouring  $\phi$ -slices and thereby can be easily removed. Additionally to the pile-up detachment small  $\phi$ -slices also improve the time performance as it scales linearly with hit occupancy [35]. As minimum bias events are mainly characterized by a large production of low  $p_T$  particles and the  $p_T$ -cut enters in the width of the  $\phi$ -slice, this was a main parameter to vary in the adaptation for low- $p_T$  tracks and is described in section 5.5.3.

The purpose of the second part is to find track candidates out of the spacepoints. After computing the z-vertex of a group of spacepoints the **HitFilter** follows. This algorithm exploits the fact that spacepoints from a sufficient high  $p_T$  and coming from tracks with one z-position have similar  $\eta$  and  $\phi$  values. The first step is to calculate the  $\eta$ -values of the spacepoints and a two-dimensional histogram in  $(\eta, \phi)$  is filled. In each of the bins the number of spacepoints is determined. Is this number greater than a certain threshold the spacepoints are accepted otherwise neglected for further processing. The subsequent **GroupCleaner** generates a new list of so called clean groups of spacepoints. The purpose of this algorithm is to remove groups that possibly contain fake spacepoints either from

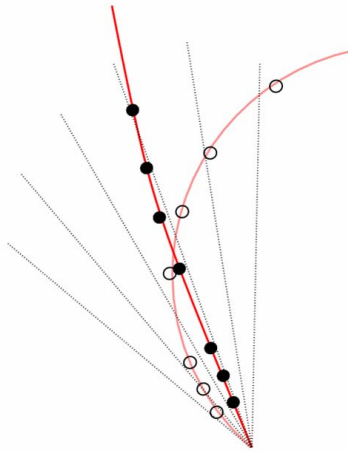


Figure 5.4: shows a sketch of the reconstruction mechanism of IdScan from the transverse plane: Filled dots represent detector hits of a high  $p_T$  track and empty dots hits of a low  $p_T$  track. By slicing the transverse plane in  $\phi$  one can grep most of the 3d-hits of a high  $p_T$  particle in one slice (filled dots) while those of a low  $p_T$  track (empty dots) are distributed over several slices.

several tracks together or noise. To clean the groups produced by the HitFilter track parameters from triplets of spacepoints are extracted:  $\phi_0$ ,  $1/p_T$  and  $d_0$ . Again clustering of spacepoints is expected for those coming from the same track in a two-dimensional histogram in  $(\phi_0, 1/p_T)$ . After filling such a histogram the same procedure as in the HitFilter is followed to remove too small groups by comparing the number of spacepoints per group to a minimal amount of spacepoints in at least four different layers. To avoid binning effects neighbouring bins are merged and their content is returned as track candidates.

In the third part of IdScan a **Track-Fit** is performed on the track candidates. About 100 % of the track candidates become tracks within this step [33].

In the final part an **extension to TRT** is performed for each track and refitted afterwards. The fitter uses the technique of the extended Kalman filter by only estimating the track parameters at the closest approach to the beam line. Then the track state propagation from layer to layer is performed by including corrections of material effects.

For this work part IV was completely excluded. As the efficiency between the HitFilter and the Track-Fit is about 100% an extension to TRT would merely consume more processing time, also a fit on a track is not required. The crucial part is solely a good guess of the z-vertex.

The performance of track reconstruction in IdScan becomes efficient for relatively high  $p_T$ 's about 85% for 6 GeV muons and higher for greater  $p_T$  values [33]. In order to use it for minimum bias event selection the performance had to be optimized for lower  $p_T$  tracks.

## 5.4.2 EF Track Reconstruction: NewTracking

At the EF stage full event information is available as well as access to complete calibration. More sophisticated track reconstruction can then be executed based on the offline reconstruction code but “wrapped” in order to use it in the trigger (RoI based processing). The software for such track reconstruction is named NewTracking. Particular emphasis on performance was already put during the development of offline code such that the trigger setup of NewTracking immediately profited.

**Track Reconstruction Strategies** The inner detector track reconstruction software consists currently of two sequences, the main *inside-out* approach and the consecutive *outside-in* track reconstruction sequence. The primary pattern recognition is realized in the inside-out sequence by a sequence of modules, represented by four **Algorithms**: I. spacepoint formation, II. spacepoint seeded track finding, III. ambiguity solving and IV. TRT track extension.

**I. Spacepoint formation** Spacepoints are formed in the same way as for the second trigger level. Still, there is a difference in the storing and retrieving information about spacepoints as they do not use the same base classes. However, there is no difference in LVL2 or EF spacepoints from the physics point of view, i.e. spacepoints formed at LVL2 and EF are the same, the LVL2 spacepoints formed can not be processed by EF algorithms which is important for the implementation of the minimum bias chain.

**II. SpacePoint seeded Track Finding** The track seeding works by first finding a pair of pixel spacepoint objects and then calling the **SizVertexMaker** to build z-vertices using the histogramming technique. Those spacepoints compatible with a minimal given  $p_T$  and  $d_0$  are kept as seeds. After a fast primary vertex search seeds are furthermore required to consist of at least three spacepoints, although this tolerance region for predicted vertices can be chosen as cut parameter. Another approach is to perform *unconstrained seed search*, i.e. without the primary vertex constraint. Naturally this leads to more initial seeds and thus to a higher time consumption. On the other hand higher efficiency is found for “loosely” constraint primary vertices.

The spacepoint seeds mark the direction in which a *road* of detector elements is build (by the road builder) in order to search for more associated hits to one track candidate. One detector element is the smallest unit of the detector able to send a signal. The combination of hits yielding the lowest residuals (squared distance of measurement and track extrapolation) are taken to build the road. At this level a spacepoint object is still dissolved in clusters, of which it originally consists. To find track candidates, all the raw data clustered to collections are retrieved from the transient event store, including those cluster collections that were not used for a creation of a spacepoint object. Only cluster collections that are located on the road are further processed by the Kalman-fitter-smoother to form track candidates. It follows the track trajectory and adds hits successively. At each step the track information is progressively updated by performing a fit. Thus, on the next measurement surface the track representation is precisely predicted.

track characteristics	detector	scores
B layer hole	pixel	- - -
layer hole	pixel	- -
overlap hit	pixel	+++
overlap hit	sct	+++
sensor hole	sct	-
layer hole	sct	- - -

Table 5.1: Scoring strategy employed for ambiguity solving by evaluation of track characteristic. Track scores are distributed according to the sub-detector and detector layer; + symbolizes a benefit and - a penalty.

**III. Ambiguity Solving** The output of the Kalman-fitter-smoother are in general more than one track candidates for one true track. This number can be very high also depending which kind of event is processed. It has to be resolved before the extension to the TRT is performed. Track candidates can have shared hits or can be incomplete. They can also describe fake tracks for which the majority of the hits do not originate from a single particle. A first step is to refit the hits forming a track candidate with refined geometry incorporating a detailed material description. The outcome of the fit is a global fit-parameter =  $\chi^2/n_{d.o.f.}$  which is not sufficient to decide if it was good or fake track. Therefore, a scoring strategy has been developed allowing to take into account the morphologic character of a track. Different track characteristics are scored with penalty or benefit weighting measurements of different sub-detectors. This results finally in an overall track score. An overview of scores for tracks found in the seeded track search is given in table 5.1. In each layer exists a small overlap region. If a hit in such a region is registered, the track is highly scored. In contrast if a track candidate misses a hit in the first pixel layer (B-layer) or in one of the SCT layers, it receives strong penalty. After scoring shared hits are assigned to the track with higher scores. The remaining track is re-fitted without the former shared hits and scored again. If it falls beyond a certain quality cut it will not be further processed. Otherwise the resulting track can be extended.

**IV. TRT track Extension** This part is divided into two modules represented by the algorithms `TRT_ExtensionAlg` and `InDetExtensionProcessor`. `TRT_ExtensionAlg` calls as a first step a dedicated `AlgTool` to find extensions of the track candidates from the preceding part. Two extension tools are implemented. The extended Kalman-Fitter follows a classical approach, building a road of detector elements based of track extrapolation. A track-fit checks afterwards the compatibility to the silicon tracks. The second one is the deterministic annealing filter, optimized for very high hit densities. Here, TRT measurements are grouped for each read-out element and represent one input object for the track fit. The hits are weighted according to the distance of the hit to the prediction of the trajectory. The output of `TRT_ExtensionAlg` is a map filled with the silicon tracks and their extension, if no extension could be found, the entry is empty. This map is stored in `StoreGate` and retrieved from `InDetExtensionProcessor` in order to evaluate the extended track with respect to the original, silicon track. The combined track is fitted and scored with the same mechanism used in the ambiguity solver. The track is then re-fitted in an iterative way. Finally it is compared to the original track reconstructed only with

event type	category
minimum bias/non-diffractive	signal
single + double diffractives	not-background
beam-gas	background
(halo)	background
empty/noise	background

Table 5.2: Events considered for the presented minimum bias trigger concept. The diffractive events were neither background nor signal events. They are rather counted to signal but with less priority w.r.t the non-diffractive processes. Halo events have not been studied here but will be treated as background.

silicon information.

For the future there will be the subsequent track reconstruction known as the *outside-in* sequences which is up to now under development and only partly put in place in the latest stable release <sup>2</sup>. Outside-in track reconstruction is required as some tracks coming from secondary decay vertices or from photon conversions may have not sufficient silicon hits to enter the list of track candidates as no initial seed was formed or if yes, would survive the ambiguity solver. However, for the same reasons as mentioned for the studies with IdScan the part with the TRT extension was completely excluded. For the following studies merely “silicon” algorithms were used.

## 5.5 Background Studies for Possible Cuts

This section contains the main results of the studies. First of all, signal and background samples are detailed with focus on their event characteristics including an estimation for beam-gas rates in the start-up phase of LHC. After that general aspects on efficiency determination are outlined which were applied in the following two sections dedicated to empty and beam-gas rejection. An overview of the event types and their meaning for the presented concept is given in table 5.2.

**Signal** Non-diffractive processes were taken as signal throughout this thesis as they are usually referred to minimum bias events giving the largest contribution to the total cross-section at LHC energies (see section 2.3.2). Typical topologies for these events are the event particle distribution, the  $p_T$ -spectrum and the pseudorapidity distribution. For minimum bias events about 15 charged stable particles are produced per event at design luminosity (figure 5.5) according to Pythia MC simulation. They possess an exponential suppressed  $p_T$ -spectrum (figure 5.20) and are distributed flat in  $\eta$  (figure 5.7). Diffractive events were not taken into account for the design of a minimum bias trigger though single and double diffractive processes do not represent background. They contribute only little and are therefore labelled “non-background”.

**Background** There will be several kind of events which are treated as background in the presented concept. As estimated before empty bunch-crossings events will occur about

<sup>2</sup>The status of is the same as of the note [36].

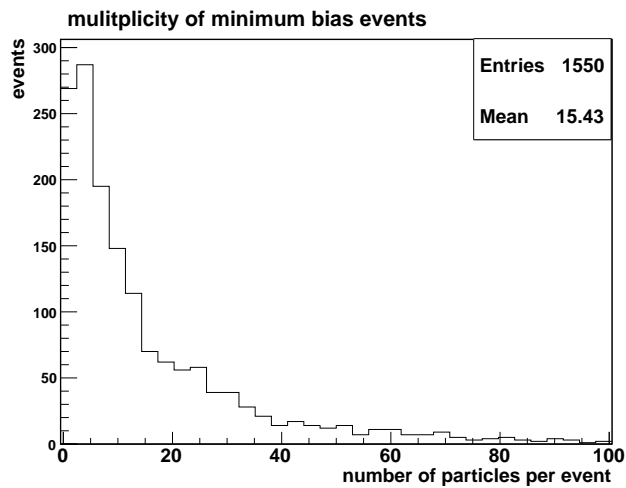


Figure 5.5: MC truth distribution of particles per event. About 15 charged stable particles per event are expected at design luminosity. Not shown are the number of neutral particles created in pp-collisions as they are invisible to the inner detector tracking system.

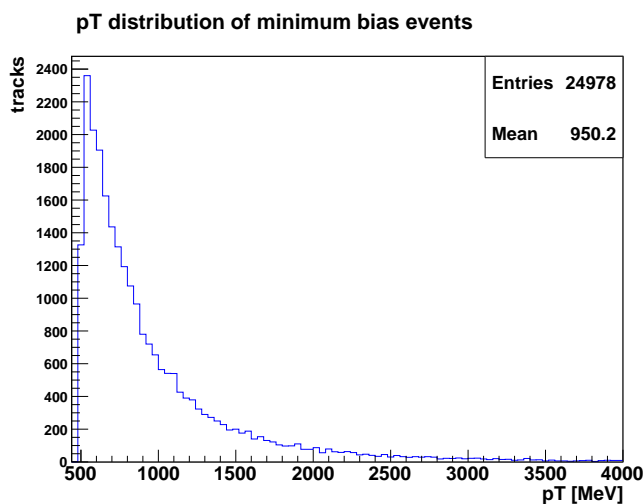


Figure 5.6: MC truth  $p_T$ -distribution of minimum bias events. The charged stable particles rather settle at lower  $p_T$ -values, showing an exponentially suppressed  $p_T$ -spectrum.

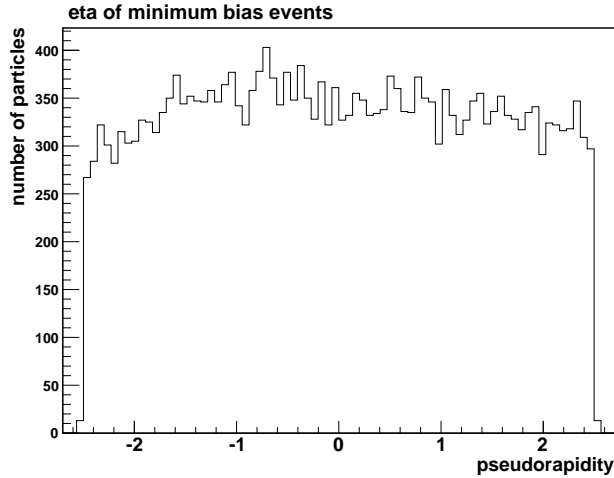


Figure 5.7: MC truth distribution of pseudorapidity in minimum bias events. The particles are approximately flat distributed in  $\eta$ .

9 times more often than single proton-proton interaction. These empty or more precisely noise events have to be rejected. They are characterized by low detector activity. Another background will rise from interactions of the beam with residual gas inside the beam pipe. These interactions are normally referred to as beam-gas events and usually have a large spread in  $z_0$  as they can occur all along the beam-pipe. Most crucial are those close to the interaction point. The reason for considering beam-gas rejection *online* is simply due to the unknown precise rate of such kind of interaction. However, an estimate on the beam-gas rate can be given (see below). Further events to be considered as background are so called halo events, which are created if the beam hits material from the machines outside of the detector itself. Some of the produced charged particles will fly collinear to the beam and pass the detector leaving essentially hits in the endcaps. They should therefore show a significantly different signature from minimum bias events. A simulation of such events did not exist and could not be produced during the time of this thesis. For this reason they were not studied in this work.

A **beam-gas rate estimation** is given for the start-up scenario. It has been estimated before in [43] for the commissioning phase and for different machine scenarios and -as it is noted- in an inconsistent way due to certain assumptions for unsettled parameters.

The collisions of proton beams with residual gas molecules can be treated as an inelastic fix target collision between a proton and a nucleon. At LHC energies the proton-nucleon cross-section can be approximated by the proton-proton cross-section. With a proton beam energy of 7 TeV and the energy of the proton in rest the c.m.e. is 115 GeV. The rate for beam-gas collisions  $\dot{N}$  is

$$\dot{N} = \dot{N}_1 n_2 dx \sigma \quad (5.1)$$

with

$$\dot{N}_1 = \text{beam proton rate} = I_{beam}/e,$$

$I_{beam}$  = beam current,  
 $e$  = the electron charge =  $1.6 \cdot 10^{-19}$  C,  
 $n_2$  = the density of the target particles =  $N_A/V_m$ ,  
 $N_A$  = Avogadro-constant =  $6.02 \cdot 10^{23}$  mol $^{-1}$ ,  
 $V_m$  = mole volume =  $V/n = RT/p$  using the ideal gas equation (thin gas),  
 $R$  = universal gas-constant = 8.3 J/K mol,  
 $T$  = temperature = 5 K,  
 $p$  = pressure in the beam-pipe =  $4 \cdot 10^{-7}$  Pa,  
 $dx$  = interaction range =  $\pm 25$  cm,  $\pm 3.5$  m  
 $\sigma$  = ionisation cross-section of gas molecule =  $\sigma_{pp} \cdot A^{0.7}$   
 $\sigma_{pp}$  = inelastic proton-proton cross-section  $\approx 50$  mb at  $\sqrt{s} = 120$  GeV,  
 $A$  = molecule mass number of gas constituents.

The nominal beam current is  $I_{beam} = 0.6$  A corresponding to  $1.1 \cdot 10^{11}$  protons per bunch thereby to the nominal luminosity of  $\mathcal{L} = 10^{34}$  cm $^{-2}$ s $^{-1}$ . As the luminosity for the presented concept will be  $\mathcal{L} = 10^{31}$  cm $^{-2}$ s $^{-1}$  and the bunch crossing pitch 75 ns, the beam current is taken to be 0.01 A supposing the same size of the proton bunches as for the nominal values.

According to [44] mostly residual gas molecules of H<sub>2</sub>, CH<sub>4</sub>, CO and CO<sub>2</sub> will be present in the start-up phase. These were taken into consideration and their cross-section and rates integrated over the inner detector acceptance region and close to the interaction point (IP) were calculated and summarized in table 5.3. A constant gas density of  $9.6 \cdot 10^{14}$  molecules/m<sup>3</sup> at 5 K has been assumed throughout the ATLAS cavity as the pressure was taken the same for each gas molecule. This results in an overall beam-gas rate of about 30 kHz at  $\pm 25$  cm at the IP and 410 kHz at  $\pm 3.5$  m for the inner detector range. If one considers design values for the beam current the rate may rise to 1.8 MHz and 24 MHz respectively. This estimation depends crucially on details of the machine commissioning scenario. More information about input parameters and operating scenarios can be found in [44] and [45].

gas molecule	A	$\sigma$ [mb]	rate IP [kHz]	rate InDet [kHz]
H <sub>2</sub>	2	85	1.5	20.0
CH <sub>4</sub>	16	350	6.1	85.8
CO	28	520	9.0	126.9
CO <sub>2</sub>	44	710	12.4	174.1

Table 5.3: Estimation of the gas rate in the start-up phase is listed for main gas species close to the interaction point at  $\pm 25$  cm and for the inner detector acceptance at  $\pm 3.5$  m.

### 5.5.1 Efficiency and Fake Rate

Depending on which of the above defined background events has to be rejected, different sets of cuts can be applied in order to increase the trigger performance. There are basically two **selection variables** that have been studied in more detail: I. number of spacepoints which can be further differentiated into number of SCT- and pixel-spacepoints and II. number of rough reconstructed tracks. The number of spacepoints can already reject empty events while tracking can discard beam-gas or halo events. The considerations

variable	cut
radius at start vertex	$R_{start}(vtx) < 1 \text{ cm}$
radius at end vertex	$R_{end}(vtx) < 20 \text{ cm}$
particles	$p, \bar{p}, K^\pm, \pi^\pm, \mu^\pm, e^\pm$
z-coordinate	$ z_0  < 10 \text{ cm}$
pseudorapidity	$ \eta  < 2.5$
transverse momentum	$p_T > 500 \text{ MeV}$

Table 5.4: To define the Monte Carlo truth sample several cuts were used ensuring to take only those into account that are *visible*. Application of the last cut is a looser restriction on the sample.

about fake rates merely enter in the track based selection as only fake tracks were considered.

For the determination of the **reconstruction efficiency** only *visible* particles, which means charged, stable particles generated within the central detector region were taken into account. An overview of the selection cuts on MC truth particles is given in table 5.4. A cut on the generated  $p_T$  at 500 MeV was applied as a first aim was to reconstruct tracks down to this value. For higher  $p_T$ -tracks it is assumed that reconstruction performance improves. For the reconstructed tracks only those inside the inner detector acceptance were accounted, i.e. with  $|\eta_{rec}| < 2.5$ .

The **trigger efficiency** was determined for different selection variables which will be specified in the respective section. It is defined as  $\epsilon$  taking into account the fraction of number of events having passed the cut  $N_{pass}$  and those reconstructed events without conditions on the selection variable  $N_{total}$ .

$$\epsilon := \frac{N_{pass}}{N_{total}} \quad (5.2)$$

The error of the efficiency was calculated according to 5.3 taking into account that the events passing the cuts form a subsample of the total sample. It is derived from the usual error propagation law (see appendix B):

$$\sigma_\epsilon = \sqrt{\frac{\epsilon(1-\epsilon)}{N_{total}}} \quad (5.3)$$

**Fake tracks** indicate wrong combinations of detector hits to a track and are constructed either by combining noise hits with true track hits or by a false combination of hits of a true track but originating from different tracks. In the latter case the event is a real minimum bias event and worth to be triggered. In the first case it can still represent a minimum bias event as such an minimum bias event contains usually more than a single particle. Other tracks may have been successfully reconstructed. The mean multiplicity of  $\sim 15$  as shown in figure 5.5 constates that there are in general more than one particle produced per event. Therefore, even events containing wrongly reconstructed tracks next to correctly reconstructed ones are real minimum bias events. For this reason fake tracks were not explicitly excluded in the determination of trigger efficiency. However, in order to compare the performance of different reconstruction algorithms the fake tracks were

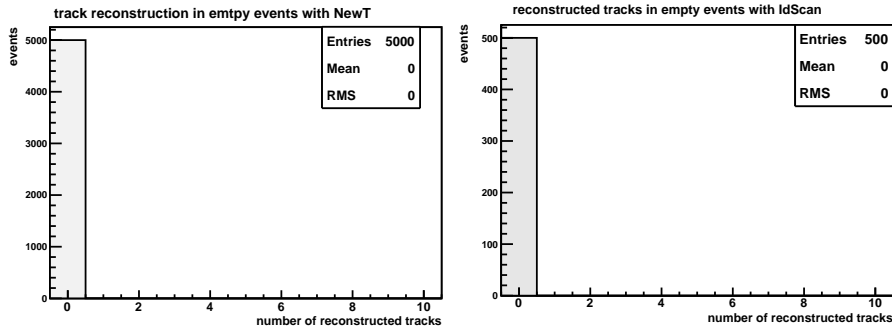


Figure 5.8: As expected no tracks are reconstructed in empty events, neither on LVL2 by IdScan (right) nor on EF by NewT (left).

also taken into account. A track was considered as a fake track if  $< 50\%$  of the hits are assigned to true MC hits.

The trigger purity for minimum bias events depends on the mixture of beam-beam and beam-gas events. Due to missing information of the beam-gas event simulation it was not possible to connect the beam-gas event simulation to the estimation of beam-gas rates in order to determine the trigger purity. However this is not considered to be crucial so far as the result of the rate estimation shows a very small rate of 30 kHz near the interaction point compared to the estimated minimum bias rate of 13 MHz.

### 5.5.2 Empty Event Rejection based on Spacepoints Requirements

The rejection of empty events was investigated by looking at earlier stages than track reconstruction. No tracks were expected to be reconstructed in these events which was the case for the LVL2- as well as for the EF- track reconstruction algorithms (IdScan and NewT) as shown in figure 5.8. The earliest measurements to look at would be clusters of detector hits. The next stage would be spacepoints formed out of these clusters. As the SCT spacepoint formation provides an intrinsic noise suppression they seem well suitable. The direct transformation of pixel clusters into spacepoints offers in contrast no gain but also no loss in information. Therefore, one can consider pixel spacepoints and their clusters equally in the studies. It turned out that the time performance is not downgraded significantly by forming pixel spacepoints of clusters. Therefore, pixel spacepoints are considered throughout this thesis. However, for the later realizations of the trigger merely clusters might be sufficient.

In the following section the studies on each kind of spacepoints are presented covering a description of the processed data. A comparison of simulated empty events to measured empty events is presented for SCT spacepoints before discussing its rejection power. Afterwards, the rejection power is discussed for pixel spacepoints.

## Semiconductor Tracker (SCT) - Spacepoints

In the simulation of empty events only random (gaussian) noise was taken into account. Correlated<sup>3</sup> noise that arise in electronics of one module and extend to a neighbouring module was not included in the simulation as one estimates gaussian noise to be dominant [38]. One parameter was modified in the simulation which controls the amount of generated noise in each strip (or pixel-element respectively). This noise parameter is the width of the gaussian distribution in unit of electron charge (see also section 3.2.1). The occupancy probability of a channel, indicating the probability of creating such a noise hit, can then be estimated using the gaussian distribution formula

$$1 - \alpha = \frac{1}{\sqrt{2\pi}\sigma} \int_{\mu-T}^{\mu+T} e^{-(x-\mu)^2/2\sigma^2} dx = \operatorname{erf}\left(\frac{T}{\sqrt{2}\sigma}\right) \quad (5.4)$$

where  $\mu$  denotes the mean value,  $\sigma$  its standard deviation (width of the distribution),  $T$  the threshold defining the confidence interval and  $\operatorname{erf}$  the error function. Computing  $\alpha = 1 - \operatorname{erf}(T/\sqrt{2}\sigma)$  yields the occupancy probability. The default value of the SCT noise level in the simulation was set to 1400 electrons which corresponds with a 1 fC threshold to an occupancy probability of  $8.1 \cdot 10^{-6}$  using equation (5.4). The noise level parameter was increased up to 1800 electrons representing an occupancy of  $5.2 \cdot 10^{-4}$  in order to be in a conservative scenario.

Simulated noise events were compared with real noise events recorded in cosmic runs, summer 2006. During this test phase, part of the SCT detector also in combination with the TRT were tested. In the following only those events were taken into account for noise events when the cosmic tracking algorithm did not reconstruct any tracks. These events were a measure for empty events and the SCT spacepoint distribution was used as an estimate for the SCT simulation quality. The run configurations were chosen such that they were similar to those in later physics runs in the real experiment. The main criteria was a triggered read-out of the events. Also data from dedicated noise runs existed but in these runs noise threshold scans were performed which is not useful for our purposes. For detailed technical information on the configuration, see [39].

In figure 5.9 one can see the comparison of real data of  $\pi/2$  of the SCT-barrel and the simulation of the whole SCT-detector. There is an discrepancy visible in the mean value of formed spacepoints having a mean number of spacepoints for  $\pi/2$  of SCT-barrel  $N_{barrel}^{data} \approx 4$  and for the simulation  $N_{SCT}^{sim} \approx 0.2$ . This can be due to some inefficiency in the track reconstruction algorithm for cosmic events. Cosmic tracks may fall such that they hit the barrel only very slightly possibly at regions close to the endcaps. In this way just a tiny part of the track is seen by the barrel and could not be reconstructed by the cosmic tracking algorithm but in reality they are contributions from real tracks.

Further, several data from cosmic runs employing  $\pi/2$  of the SCT-endcap were analysed. Data recorded in different runs (but similar in configuration) for  $\pi/2$  of the SCT-endcap were analysed and their spacepoint distribution is shown in figure 5.10. A mean value of 0.9 spacepoints for all runs were formed. This smaller mean value of the formed spacepoints for endcap data is in accordance with what can be expected from cosmic runs:

---

<sup>3</sup>also called coherent noise

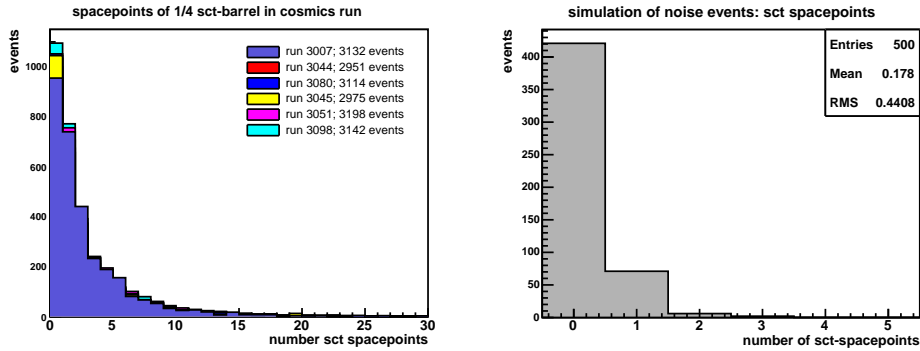


Figure 5.9: Comparison of noise events of real data (right) and simulation (left). For the real data several data files from a  $\pi/2$  of the SCT barrel were used indicated by different run numbers.

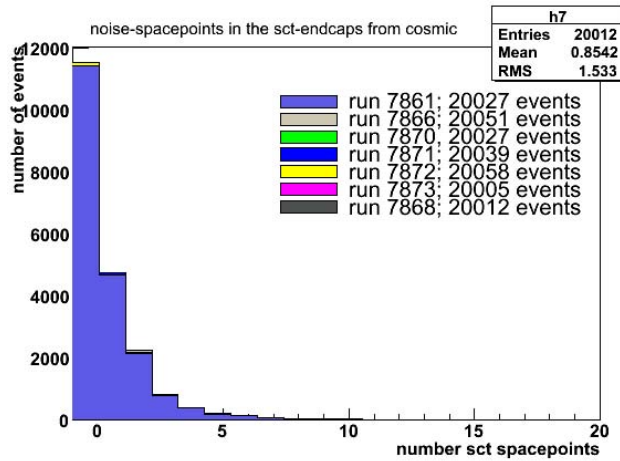


Figure 5.10: Noise events of recorded in cosmic runs for  $\pi/2$  of the SCT-endcap.

Cosmic tracks fall rather vertically and therefore hit the barrel more than the endcaps<sup>4</sup>. About 7.6 times more events were available than for the barrel data, for further details on the configuration of the dataset, see [40].

## Pixel Spacepoints

In the same simulation of noise events the noise parameter of the pixel detector was left as set to its default value of  $10^{-4}$  as recent measurements evaluated this to be pessimistic already (measurements in the end of 2006 showed an occupancy of  $10^{-6}$  [41]). As expected many more pixel spacepoints are formed as in the SCT detector due to their distinctive spacepoint formation.

<sup>4</sup>Cosmics are quite complementary to halo events that rather leave hits in the endcaps.

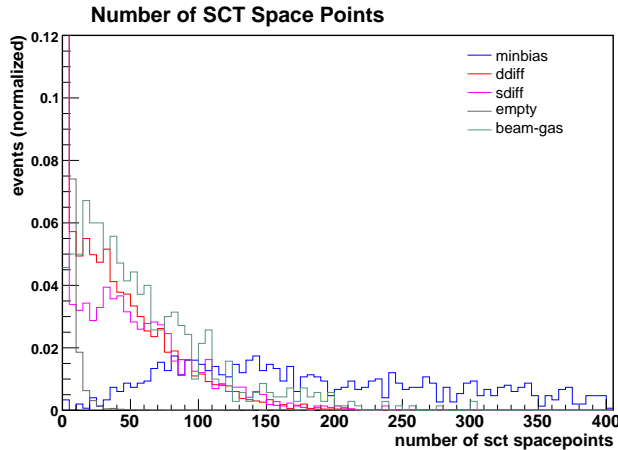


Figure 5.11: Comparison of summed noise events of real data from  $\pi/2$  of the SCT barrel and  $\pi/2$  of the SCT endcap (grey) and simulation of SCT spacepoints of minimum bias events (blue). In red and magenta are the double and single diffractive events shown. A relatively low cut can be applied at around 25 to reject empty events already while keeping almost all of the signal.

detector	mean number of spacepoints
SCT barrel	$15.7 \pm 0.1$
SCT endcap	$3.558 \pm 0.003$
SCT total	$19.3 \pm 0.1$
pixel total	$820 \pm 5$

Table 5.5: Mean number of spacepoints in the SCT and pixel detector for empty events. The SCT-values were obtained from data while the value for pixel spacepoints was obtained from simulation. The small error for the endcaps is due to the larger sample that was available.

## Results for Empty Event Rejection

**SCT cut** Both noise measurements, from SCT-barrel and endcap together were linearly scaled to the whole detector by multiplication of the data by four which is obviously an approximation neglecting any non-linear response of the detector systems. For the pixel spacepoints the mean number could be directly determined as only simulation “data” was used. The result for the number of formed spacepoints in the SCT-barrel and SCT-endcap are listed in table 5.5 together with those for the pixel detector. It includes uncertainties obtained by using the usual formula for the standard deviation<sup>5</sup>. The numbers are an overall quantity averaged for several events. Looking at event-by-event spacepoints many more of them can be formed.

The noise spacepoints were compared to the one of the minimum bias, diffractive and beam-gas events which is shown in figure 5.11. One can see that the distributions of empty events and minimum bias events separate quite well such that by a single SCT-cut it is

$${}^5\sigma_N = \sqrt{\frac{\sum_{i=0}^n (N_i - \bar{N})^2}{n(n-1)}}$$

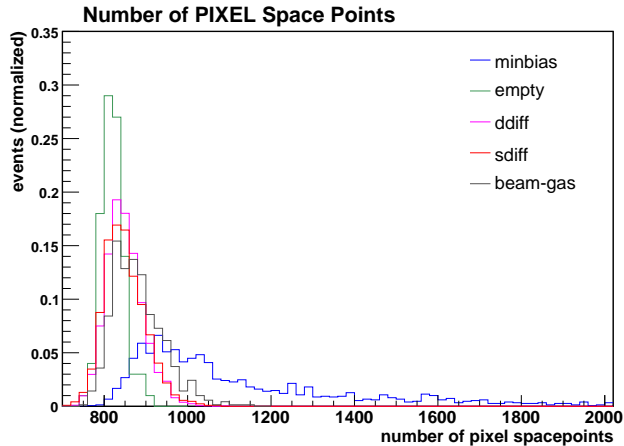


Figure 5.12: Simulated noise spacepoints in the pixel detector are compared to pixel spacepoints of minimum bias and diffractive events. As the distributions of noise and minimum bias events overlap significantly it will not be possible to remove empty events with a single cut on pixel spacepoints completely without losing efficiency in the signal.

possible to reject all of the noise events while retaining a high efficiency for minimum bias events. The diffractive events resemble slightly empty events showing many events with a low number of spacepoints with respect to the minimum bias events. Beam-gas events are only shown for completeness. Their rejection is considered by a multiplicity cut (next section).<sup>6</sup>

The same distributions are shown for pixel spacepoints in figure 5.12. There, the pixel spacepoint distribution for minimum bias overlaps in the range from 800 - 930 spacepoints with the noise spacepoints. Hence, a single pixel cut will not lead to a high rejection efficiency without loss of minimum bias trigger efficiency.

The trigger efficiency for different cuts on either the number of pixel spacepoints or on the number of SCT spacepoints or on both was then investigated. In figure 5.13 the trigger efficiency is shown when only a single cut on SCT spacepoints is applied for minimum bias, empty, beam-gas and diffractive events. The efficiencies for a single cut on pixel spacepoints using the same samples are plotted in figure 5.14. Cutting at about 20 SCT-spacepoints yields a sufficiently good result: While for minimum bias events

$$(99.5 \pm 0.1)\%$$

are retained, only

$$(6.1 \pm 0.1)\%$$

are for empty events. In contrast a single cut on pixel spacepoints at around 830 as figure 5.14 suggests may still keep more than 99% but also around 35% of the empty events which is not satisfactory. However, this is a rather pessimistic scenario compared to noise

<sup>6</sup>Beam-gas events were simulated by a collision of a proton with various gas molecules (H, C, O, N, Zr, V, Ti).

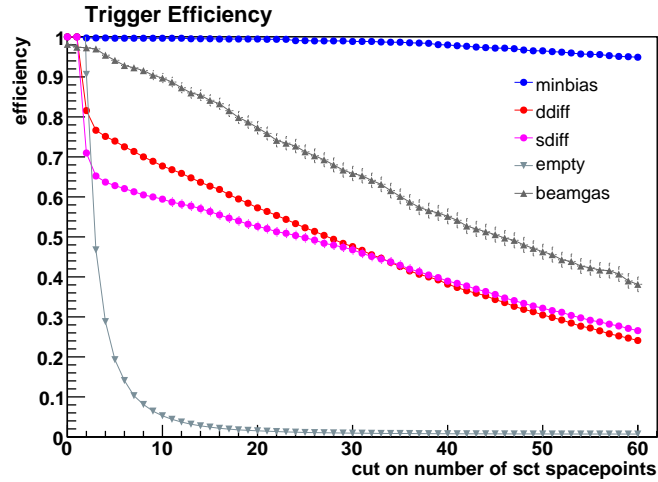


Figure 5.13: Trigger efficiency for essentially minimum bias (blue), empty (dark grey) and for other datasets are shown when applying a cut on sct spacepoints. For the empty events real data of  $\pi/2$  of the SCT detector were used linearly scaled to the whole detector.

measurement in Dec. 2006. In reality one may obtain higher efficiencies.

Another possibility is a combined cut, where one requires a certain number of SCT OR pixel spacepoints. To decide whether this cut can lead to better results the empty event rejection efficiency was plotted over the signal trigger efficiency in figure 5.15. The left plot shows an overall comparison of the different cuts while the right plot is a zoom into to the most interesting region. One can see that a single pixel cut (black) is worse than the combined cut (green) and the single SCT-cut (red). From all three different cuts the single SCT-cut yields the best results, i.e. high empty event rejection and at the same time high signal trigger efficiency. Only in few cases the trigger efficiency of the combined cut is above the trigger efficiencies of the single SCT-cut but in these cases the rejection of empty events is rather modest with 60-70%. However, the combined cut can be still very useful for the case that the SCT detector performs differently (worse) from what can be expected by these studies.

### 5.5.3 Adaptation of IdScan for low $p_T$ tracks

In order to be able to reconstruct efficiently low  $p_T$  tracks parameters in IdScan had to be adapted. As already pointed out in the description of IdScan in 5.4.1 the most crucial part of IdScan concerns the first part, the zFinder. If the z-vertex can be reconstructed correctly with high performance the following steps of IdScan will show in a similar way a high reconstruction performance. Thus parameters of the zFinder had to be modified in order to reconstruct the correct z-position of the low  $p_T$  tracks. These were essentially the  $\phi$ -slice width (in degree) and a resolution parameter in z (in units of cm). For reference, parameters were used which were comparable to the largest RoI employed for the B-physics trigger<sup>7</sup>. The reference values were  $(\delta\phi, z\text{-bin size}) = (1^\circ, 0.2)$  and yielded a rather bad to modest reconstruction efficiency. One can see it in figure 5.16 where the

<sup>7</sup>the Bphysics-RoI uses  $(\delta\phi, z\text{-bin size}) = (1^\circ, 0.4)$

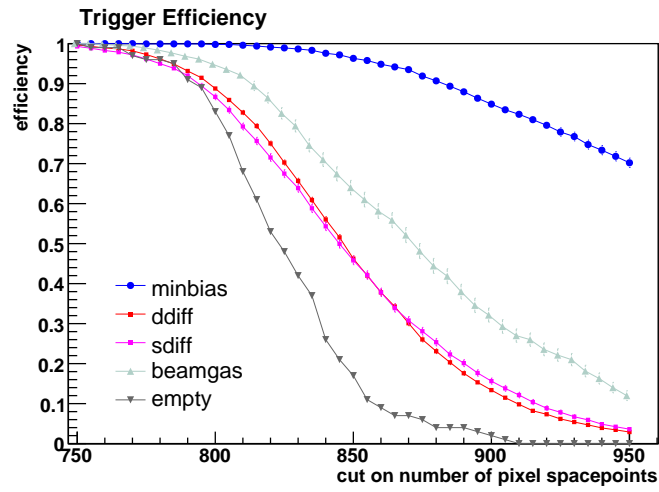


Figure 5.14: Trigger efficiency is shown for the case that a single cut on pixel spacepoints is applied. Though one could principally reject also empty events by cutting on pixel spacepoints e.g. at around 900, one loses also efficiency on the signal. SD and DD show a very similar behaviour which is not very surprising.

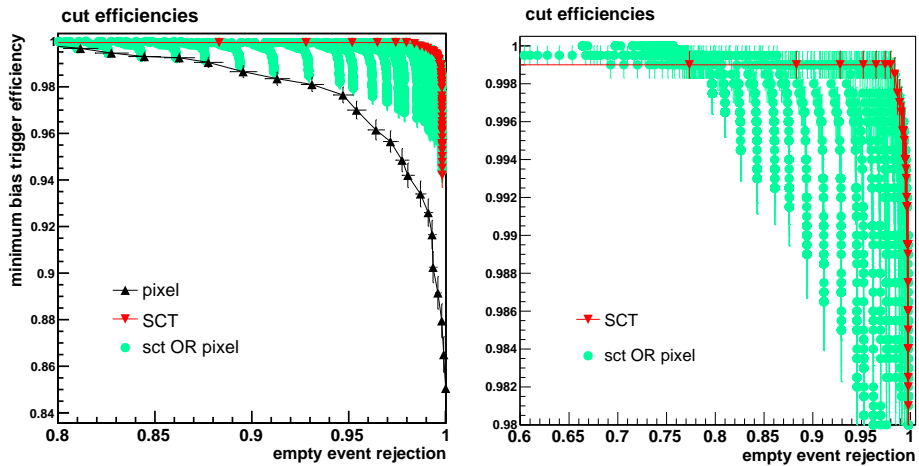


Figure 5.15: A comparison of possible cuts is illustrated. The signal trigger efficiency in dependence of empty event rejection efficiency is shown for the case when a single cut on pixel (black), a cut on SCT spacepoints (red) and an OR-combined cut of SCT or pixel spacepoints (green) are applied (left). An SCT-cut looks more efficient as a pixel cut. The combined cut may achieve high trigger efficiency but then without a high empty event rejection (right).

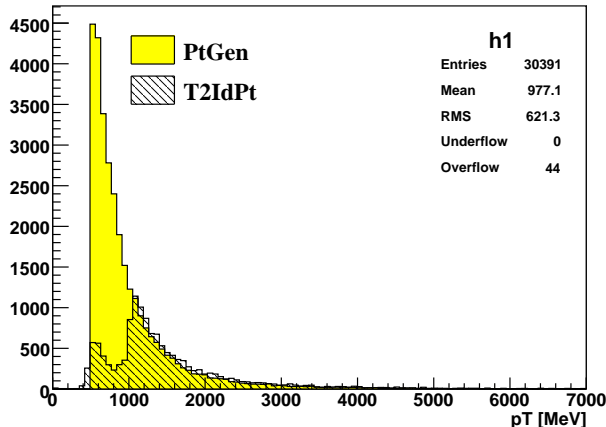


Figure 5.16: In yellow is shown the distribution of visible generated particles and in hashed the by IdScan reconstructed  $p_T$  values of the tracks.

$p_T$ -distribution of the MC truth is shown together with the reconstructed  $p_T$ -spectrum. For the Monte Carlo sample the visible cuts defined in table 5.4 were applied, for the reconstructed tracks the inner detector acceptance cut was used. The efficiency lies only at around 45 % with a fake rate of  $\sim 15\%$ . They explain the structure in the reconstructed distribution; the first peak up a  $p_T \sim 800$  MeV are fake tracks according to the definition given in section 5.5.1.

The adaptation for low  $p_T$  track reconstruction in IdScan was divided into two parts: The first one consisted in identifying parameters for correct z-vertex reconstruction, which was studied with the zFinder standalone. For the second part the track reconstruction efficiency was determined employing the parameters found with the zFinder standalone in track reconstruction for the complete IdScan sequence (but without TRT). As an orientation for the parameter scan the  $\phi$ -width slices were calculated beforehand.

**Determination of Parameter Sets** We are interested in the difference of maximal angular separation of hits for a track at a given  $p_T$  which can be related to the width of the  $\phi$ -bin size. It was already indicated in section 5.4.1 that the implicit  $p_T$ -cut is introduced by the width of the  $\phi$ -slice. The relation between the radius  $R$  of a curved track and its transverse momentum  $p_T$  in a homogeneous magnetic field  $B$  can be described with

$$R[\text{mm}] = \frac{p_T[\text{MeV}]}{0.3 \cdot B[\text{T}]} \quad (5.5)$$

Further, the relation between  $R$  and  $\phi$  is obtained by choosing a reference plane such that the first spacepoint lies in the origin. The connection of the first two spacepoints is of length  $\rho$  and defines the reference plane. Then, the relation to radius of the track curvature is given by

$$\rho = 2R \cdot \sin(\phi_0 - \phi) \quad (5.6)$$

where  $\phi_0$  and  $\phi$  represent the azimuthal angles of the spacepoints in the reference plane. By definition  $\phi_0$  is always chosen to  $\phi_0 = 90^\circ$ . For illustration of equation (5.6) see figure

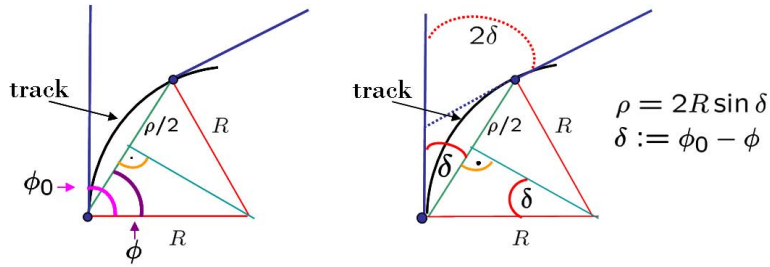


Figure 5.17: Illustration of parameters of spacepoints (blue dots) to the track : On the left the angle definitions in  $\phi$  are shown, on the right they are related to the  $p_T$ -dependent track radius  $R$ . The framework is chosen such that  $\phi_0 = 90^\circ$ .

$p_T$ [MeV]	250	500	700
R[mm]	417	833	1167
$\Delta\phi$ [°]	34.6	16.3	11.5
$\phi$ -bin size $\delta\phi$ [°]	11.6	5.4	3.8

Table 5.6: The parameter which was tuned is  $\delta\phi$  determining the  $p_T$ -cut in IdScan.

5.17. The change in angle between inner- and outermost hits corresponds to the angular difference  $\Delta\phi$  obtained by equation (5.6) for  $\rho$  values taken from the innermost and outermost detector layer,  $\rho_{inner} = 50.5$  mm for the first pixel-layer, and  $\rho_{outer} = 514$  mm for the fourth SCT-layer.

To estimate a possible  $\phi$ -slice width  $\delta\phi$  one calculates the bending from inner to outer silicon layer given a certain  $p_T$ . In our case this was done for a  $p_T = 250$  MeV, 500 MeV and 700 MeV. The zFinder determines the z-vertex position from the bin with the highest entry as well as the two adjacent bins in the z-histogram. Thus, the  $\phi$ -bin size is  $\delta\phi = \Delta\phi/3$ . The values serving as an orientation for the parameter scan is shown in table 5.6.

**Parameter Scan in the zFinder Standalone** The zFinder standalone provided information of the reconstructed and the true z vertex position. With this information one could test easier different parameters allowing to examine the performance of the zFinder.

The parameter scan was performed using different couples of a  $\phi$ - and z-bin size value. The  $\phi$ -bin size was chosen to range from  $\delta\phi = 4^\circ \dots 11^\circ$  in steps of  $1^\circ$  covering about the range calculated for different curvatures, i.e. transverse momenta, as shown in table 5.6. To each  $\delta\phi$  several z-bin sizes were tested ranging from z-bin size = 0.2, 0.5, 1., 1.5.

Ten events were processed per parameter couple. In order determine whether the parameter couple achieved a good z-vertex reconstruction performance a mean value of the differences between reconstructed and true z-vertex position for each event per parameter couple was formed according to

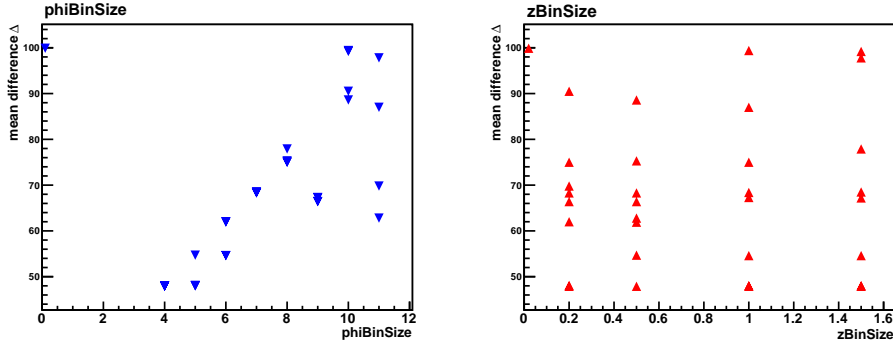


Figure 5.18: The difference of reconstructed and true z-positions averaged over 10 events is shown as a function of  $\phi$ -bin size (left) and z-bin size.

$$\Delta = \frac{1}{10} \sum_{i=1}^{10} |z_i^{\text{true}} - z_i^{\text{meas}}| \quad (5.7)$$

Large values of  $\Delta$  indicate a poor reconstruction performance of the zFinder, hence the corresponding parameters are not appropriate. The result of the parameter scan in the standalone is shown in figure 5.18. One can see that only in a few cases the difference is relatively low, if the  $\phi$ -bin size  $\delta\phi = 4^\circ$ - $5^\circ$ . The change in the z-bin size does not contribute to an improvement or degradation of performance as for each chosen z-bin size low differences could be obtained.

**Parameter Scan using IdScan track reconstruction** The application of the same parameter for the subsequent IdScan steps showed what can be expected from the zFinder. The reconstruction efficiencies were determined as defined in section 5.5.1 taking into account the usual visibility and acceptance criteria and using equation (5.2) and (5.3). The resulting efficiencies for each parameter couple is shown in figure 5.19. Practically no rise in efficiency could be achieved with respect to the reference reconstruction efficiency of 31.4%. The best value was obtained for  $(\delta\phi, \text{z-bin size}) = (4^\circ, 1.5)$ . However, the absolute value of the efficiency is still too small with 31.9%. The complete parameter couples are listed in the appendix C.

**Conclusion of Parameter Scan** The adaptation of IdScan failed so far due to insufficient track reconstruction efficiencies for  $p_T > 500$  MeV aiming at significantly more than 50 % reconstruction efficiency. It was confirmed that the performance of the zFinder is crucial for the complete IdScan sequence as lower differences of reconstructed and true z-vertex position in the zFinder corresponded to higher reconstruction efficiencies in IdScan. However, IdScan seems not appropriate for low  $p_T$  track reconstruction. These studies were continued with the alternative software NewT and is described in the following section.

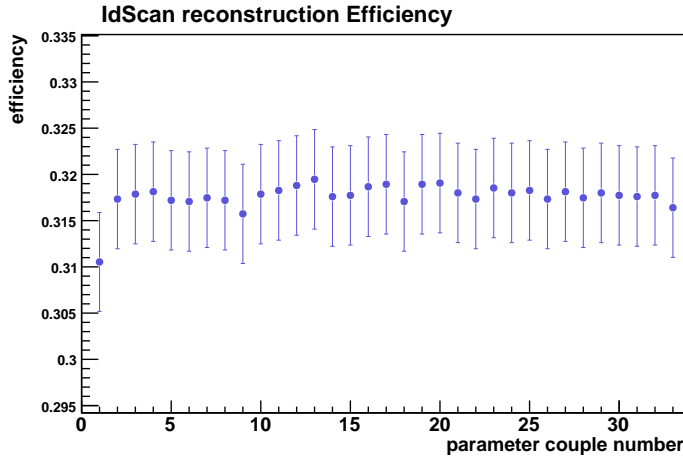


Figure 5.19: IdScan reconstruction efficiencies shown for each parameter couple. Obviously one can not recognise a significant efficiency rise.

#### 5.5.4 Beam-Gas Rejection based on Track Requirements

**Low  $p_T$ -Track Reconstruction in NewT** NewTracking is used for offline analysis as well as in the trigger at EF-level, the basic concepts of NewT were described in 5.4.2. Like in the case for IdScan the TRT part was omitted explicitly. The results for running with default parameters and in a full scan mode seem already much more satisfying than in the previous case with IdScan. It is not very surprising that looser time constraints on EF lead to more elaborate reconstruction strategies which enables more efficient low  $p_T$ -track reconstruction. The reconstruction efficiency for minimum bias events is demonstrated in figure 5.20. There, the distribution of the reconstructed transverse momenta are shown together with the respective Monte Carlo truth sample. From figure 5.21 one can see the event multiplicity also for the MC truth and the reconstructed case. For both figures the usual visibility and acceptance cuts were applied defined in section 5.5.1. An overall efficiency is obtained by the ratio of reconstructed tracks and MC truth tracks. The efficiency is  $(97.0 \pm 0.1)\%$  and the fake rate of  $(5.6 \pm 0.2)\%$ . This is fully sufficient for track reconstruction with  $p_T > 500$  MeV. Track multiplicity and  $p_T$  distribution are shown in figure 5.22 for single diffractive events and in figure 5.23 for double diffractive events.

The actual purpose for low  $p_T$ -track reconstruction is the rejection of beam-gas events. In beam-gas events collisions of protons with residual gas molecules in the beam-pipe were simulated<sup>8</sup>, here the available selection of the nucleons berilliyum, hydrogen and carbon are shown. As argued before the nucleon itself is not crucial at LHC energies. The topology of beam-gas events are shown in figure 5.24 for the generated and in figure 5.25 for the reconstructed sample where one can see a dramatic difference caused by track reconstruction in beam-gas events. This indicates an intrinsic suppression in NewT of these events which is due to an internal cut on the longitudinal impact parameter at

<sup>8</sup>This was work of A. Stradling.

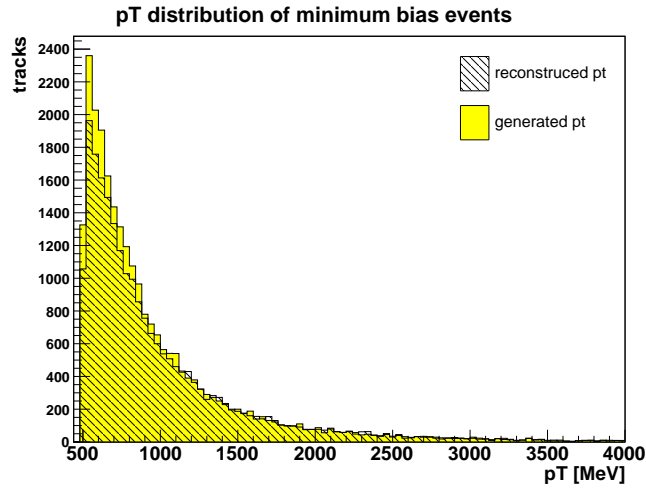


Figure 5.20: NewT reconstruction efficiency. Shown are the  $p_T$ -spectra from MC and reconstructed. Visibility-criteria were used for the MC sample and the requirement that  $|\eta_{rec}| < 2.5$  for the reconstructed distribution. Fake tracks are excluded.

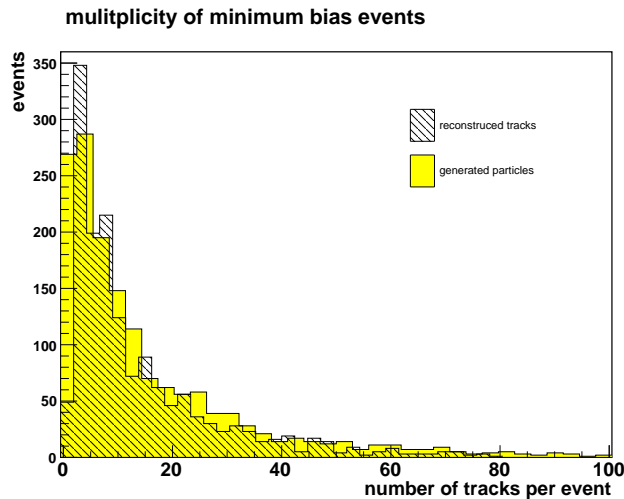


Figure 5.21: Event multiplicity for tracks reconstructed in NewT shown together with MC truth multiplicity. A mean value of 15 reconstructed tracks per event can be expected, for the truth there are around 15.5 particles considering the visibility criteria.

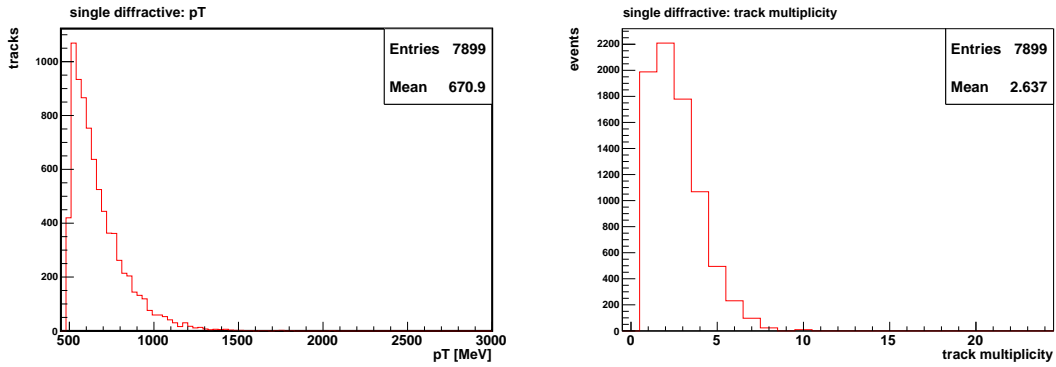


Figure 5.22: Event characteristics for single diffractive events reconstructed with NewT:  $p_T$ -spectrum (left) and track multiplicity (right). For both distributions the cut at  $|\eta| < 2.5$  was applied.

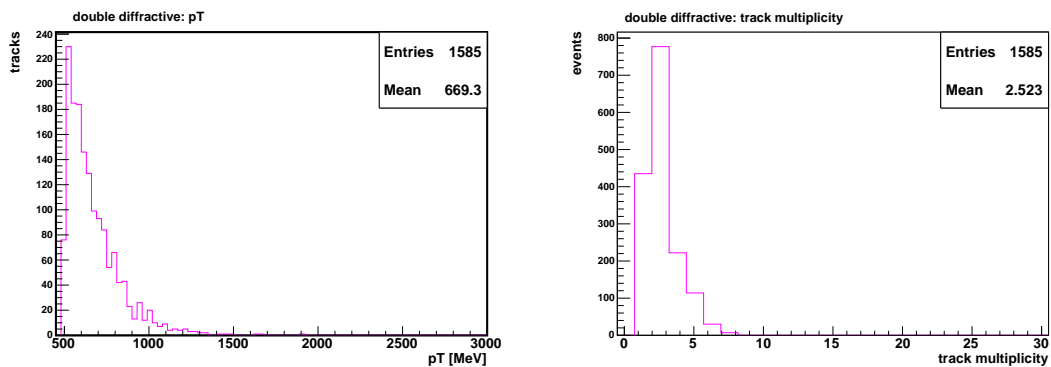


Figure 5.23: Events characteristics for double diffractive events reconstructed with NewT:  $p_T$  (left), track multiplicity (right). For both distributions  $|\eta| < 2.5$  was required.

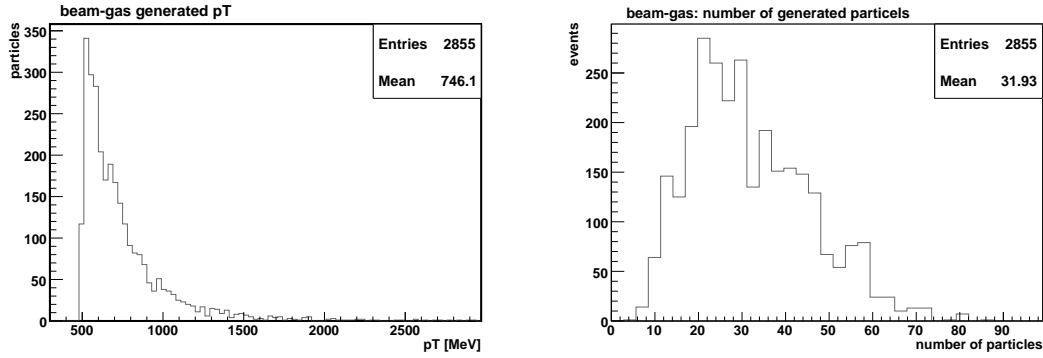


Figure 5.24: Beam-gas events characteristics generated in Hijing:  $p_T$  (left), number of particles (right). Here only stable charged particles inside the inner detector with  $p_T > 500$  MeV are accounted.

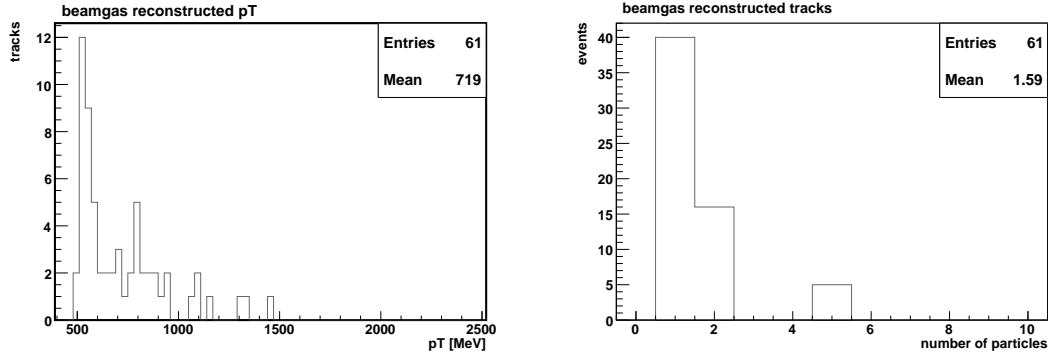


Figure 5.25: Distributions of beam-gas events characteristics reconstructed with NewT:  $p_T$ (left), track multiplicity (right). Out of around 3000 events, about 1000 for the species C, H and Be, only 61 events could be reconstructed.

$|z_0| = 250$  mm. A more stringent cut at  $|z_0| = 200$  cm can be additionally applied to reject some fraction of the reconstructed beam-gas events, the fraction that will be left is shown in figure 5.27 as a thick line whereas the thin line represents all the reconstructed  $z_0$ -value without an additional impact parameter cut. The same cut was applied to the minimum bias sample and is illustrated in figure 5.26.

Aiming at high rejection of beam-gas events the trigger efficiency was determined using formula (5.2) and (5.3). The ratio considered the number of tracks having passed a cut on the number of reconstructed tracks with  $|\eta| < 2.5$  and all tracks with  $|\eta| < 2.5$ . No further  $z_0$ -cut was applied for this determination of trigger efficiency. The result is shown in figure 5.28. One can see that requiring at least 5 tracks yields to complete rejection of beam-gas event while retaining  $(93.0 \pm 0.2)\%$  of the minimum bias events. For a more optimistic case already a cut at two tracks might be sufficient: While  $(91.8 \pm 2.5)\%$  of the beam-gas events can be rejected the efficiency for minimum bias events is still  $(98.6 \pm 0.1)\%$ . Also, about 45% of the diffractive events can be kept. Possible efficiencies for minimum bias, diffractive and beam-gas events are listed for both cuts in table 5.7.

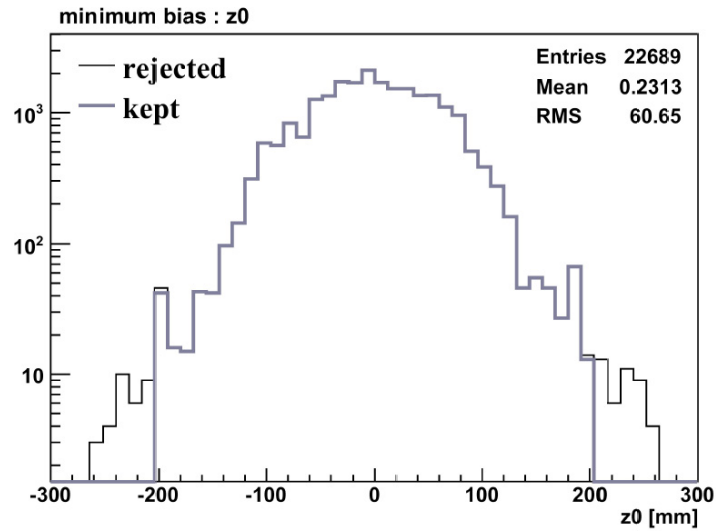


Figure 5.26: Distribution of longitudinal impact parameter  $z_0$  of minimum bias events. The thick line indicated particles having passed an additional cut at  $|z_0| = 200$  mm.

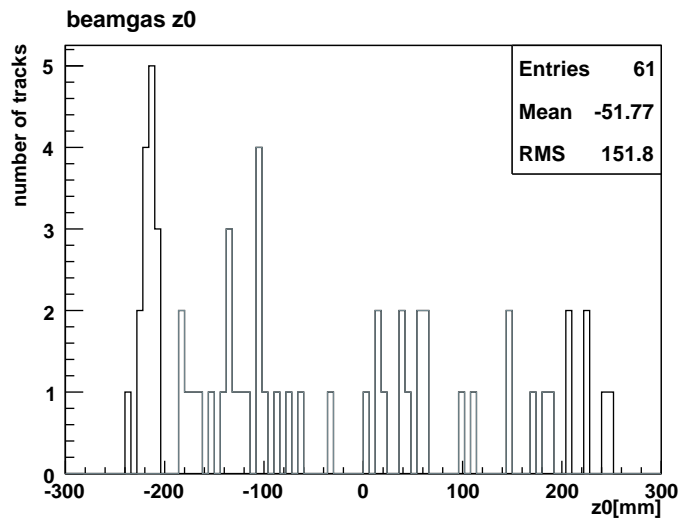


Figure 5.27: Distribution of longitudinal impact parameter  $z_0$  of beam-gas events. As in figure 5.26 the thick line indicated particles having passed an additional cut on at  $|z_0| = 200$  mm. The asymmetry in the distribution is due to single-sided event simulation. As ATLAS is symmetric one can simply imagine the same simulation mirrored.

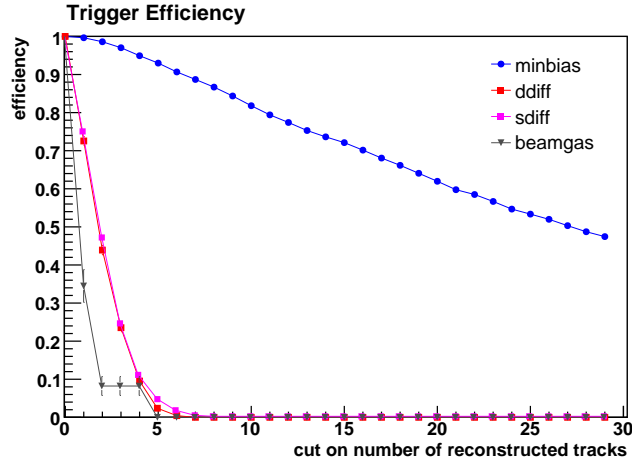


Figure 5.28: Trigger efficiency for minimum bias (blue), single diffractive (magenta), double diffractive events (red) and beam-gas events are shown requiring a certain track multiplicity.

track requirement	trigger efficiency in %	
	2	5
minimum bias	$98.6 \pm 0.1$	$93.2 \pm 0.2$
single diffractive	$46.9 \pm 0.6$	$4.6 \pm 0.2$
double diffractive	$44 \pm 1$	$2.4 \pm 0.4$
beam-gas	$8.2 \pm 2.5$	0

Table 5.7: The trigger efficiency for 2 and 5 track requirements are listed for minimum bias (signal), diffractive (non-background) and beam-gas events (background). Only a cut at the number of tracks with  $|\eta| < 2.5$  has been applied.

To conclude it will be possible to highly suppress beam-gas events by a track multiplicity cut on tracks in a given z-region while efficient triggering on minimum bias events is respected. However, a combined cut of spacepoint and track requirements was not investigated. This would be a more realistic case as tracking is performed after the event has passed a cut on spacepoints to reject noise. Nevertheless, the results obtained so far signify that the efficiencies given in table 5.7 will be reduced by less than 1% in the worst case for a previously applied SCT-cut at 20 spacepoints. In better cases spacepoints that were cut away for empty bunch-crossing events are the partly the same with spacepoints that might be lost by a track multiplicity cut. Then, the efficiencies obtained by a pure track requirement represent already overall trigger efficiencies. Nevertheless, this is still be confirmed.

## 5.6 Timing Performance

In order to examine the feasibility of the presented concept the time consumptions of algorithmic work for spacepoint formation and track reconstruction were measured. According to [23] comparable times could be measured on a 3 GHz processor which the machines

that were used provided<sup>9</sup>. Special care still has to be taken for the read-out of the whole pixel and SCT detector at LVL2 as for reasons of speed and thereby data handling of expected high rates it is not foreseen in the trigger system to process complete silicon data at this stage.

Time performance has been measured for LVL2 as well as for EF algorithms (IdScan and NewT). The measured times are independent from the farm where the algorithms will run as LVL2 and EF will use identically designed processors, only the number of CPU-units is different at LVL2 and EF. The steps of spacepoint formation are the same for both trigger levels, however there is a difference within the size of the formed objects being much smaller for LVL2 (less accurate information) than for EF objects which is also visible in the measured times. The time consumption was essentially measured for minimum bias and empty events. Diffractive and beam-gas events should have times in between as they showed this behaviour so far in spacepoint formation and track reconstruction. Their absolute value becomes important for the case when the contribution of each event constituents is known in order to make an realistic timing estimation which is likely to be possible when LHC has turned on.

### 5.6.1 Timings in IdScan

In IdScan the timing for Spacepoint formation was measured. The procedure consist of three main sequences which are *I. Bytestream Decoding*, *II. Clustering*, *III. SpacePoint Formation*. This was already outlined in section 3.2.1.

The time consumption for the complete sequence of spacepoint formation at LVL2 in a full scan mode took 32 ms for empty events as well as for minimum bias events. This might be surprising regarding the number of formed spacepoints for both event types. However for Bphysics timing measurements similar times were obtained [47], indicating that the time performance depends rather on the logic to access the spacepoints data than on the tested event types. The measured times represent rather pessimistic values as formation of both kind of spacepoints were measured. In any of the cases real data retrieval at LVL2 might be time-critical. Earlier measurements of data retrieval from the read-out buffers to the LVL2 processing farm showed that even for a large RoI (Bphysics-RoI) the retrieval time is not negligible. However these measurements are not conclusive yet as the data network was not the final [48].

### 5.6.2 Timings in NewT

To measure the timing for track reconstruction different setups needed to be tested aiming at the best possible performance of track reconstruction algorithms functioning in a full scan of the inner detector. The performed measurements can be grouped according to a “trigger” and an “offline” setup that were used. The trigger setup contained a modified sequence such that track reconstruction could be performed in a full scan of the inner detector and without TRT. For the offline setup only the TRT had to be excluded. Different event access methods are employed in each setup and had to be compared, e.g. in the trigger one event is usually accessed several times according to the number of RoI’s. This not performed offline where the whole event is processed once which is rather appropriate

---

<sup>9</sup>The machines parameter of atlhlt3 are: 2 dual core processors each with Intel(R) Xeon(R) CPU 5160 @3.00GHz, 4 MB cache, 8 GB memory

for minimum bias events. The measurements of time consumption also targeted optimization studies of the algorithm sequence that will be used in the later minimum bias trigger chain. Several features were tested: unconstrained and constrained search (see section 5.4.2) and two  $p_T$ -thresholds, being  $p_T= 500$  MeV and  $p_T= 200$  MeV, that become relevant for track reconstruction (SiTrackFinder).

The result of the comparison between the constrained and unconstrained seed search is that no significant advantage is obtained in preferring one or the other method as the measured times were about the same for both methods.

Further measurements were performed in the trigger setup with the default method of unconstrained search. Time consumption was measured for single reconstruction steps and for both  $p_T$ -thresholds as listed in table 5.8. Basically one can read in this table that the EF latency is respected for track reconstruction for the given algorithm sequence if the  $p_T$  threshold is set to 500 MeV. Mere spacepoint formation is also not time-critical, though it takes much longer than on LVL2 as might be expected from different formation of spacepoint objects (see also section 5.4.2). Additionally listed are the time for unpacking the raw data as this is expected to take most of the time. For the case that the  $p_T$  cut is lowered to 200 MeV the EF constraint is not directly met with about 1300 ms for the whole reconstruction sequence. Nevertheless, this  $p_T$  threshold could be still feasible in this setup as the averaged time still falls below the limit of 1 s for the case that track reconstruction is not performed for all events which is most likely the case e.g for the ratio 2:8 (track reconstruction:spacepoint formation).

trigger setup, rel.13 unconstrained search	<b>minbias</b>		<b>empty events</b>
	SCT+PIX/ms	SCT+PIX/ms	SCT+PIX/ms
$p_T$ -cut /MeV	200	500	independent
SCT Clustering Total (Unpacking)	233 (172)	226 (168)	178 (147)
pixel Clustering Total (Unpacking)	116 (45)	113 (43)	86 (40)
SP finding	108	183	168
SiTrackFinder	503	327	-
AmbiguitySolver	214	100	-
Total time SP formation	529	522	432
Total time tracking	1246	949	-

Table 5.8: Time consumption for track reconstruction of trigger setup (EF) in release 13. The  $p_T$ -cut was at 500 MeV. Measurements were performed on atlht3.

Timing measurements with an offline setup were considered in order to compare different methods with respect to the trigger setup. The results are listed in table 5.9 and show large differences to the trigger setup measurements: The offline timing performance is much better. The CPU-usage for the complete sequence as listed in the table is with 461 ms only the half of the time consumed at the trigger setup. This was resolved by the different event access methods as indicated above<sup>10</sup>. Indeed, recent modifications such that a new method of the RegionSelector is employed showed in first measurements a very good time performance. Even an higher performance compared to the times obtained by an offline setup could be achieved for a reference sample [46]. This is still to be tested for

<sup>10</sup>Offline uses newEvent() method while the trigger newRegion().

offline setup, rel. 12.0.6 constraint search	<b>minbias</b>		
	SCT/ms	PIX/ms	SCT+PIX/ms
1. SCT Clusterisation	110	-	120
2. pixel Clusterisation	-	105	115
3. SP finding	14	3.84	18
4. SiTrackFinder	17	25	71
5. AmbiguitySolver	18	17	28
Total time SP formation	124	100	353
Total time tracking	159	151	461

Table 5.9: Time consumption for minimum bias events with a  $p_T$ -cut at 500 MeV and run in an constraint search. Release 12.0.6 was used for track reconstruction at the EF. The times are averaged values.

minimum bias events, but the same improvement of the time performance with respect to the times in table 5.8 is expected. However, the trigger constraints can be met already. An time improvement would further allow for lowing the  $p_T$ -cut to 200 MeV which in fact has already been set to default.

## Chapter 6

# Implementation of the “Random based” Minimum Bias Trigger

In the previous chapter it was shown that the presented selection variables allow an efficient minimum bias selection. The realization of this concept is hence the next step and studies performed in this thesis have lead to possible strategies for the implementation in terms of processing steps after which the event is examined and a trigger decision is taken. Basically one trigger chain is depicted here in more detail, but since there are still open questions the description should be read as summary of the studies supplemented with more details of technical issues.

### 6.1 Trigger Requirements

The minimum bias trigger should be implemented such that it is flexible: Due to different strategies that have to be tested one should be able to switch on and off certain features. One would like to have the option to perform empty event rejection either by a cut on SCT or pixel or an OR/AND combination of SCT and pixel spacepoints. Though the efficiency for a minimal amount of SCT spacepoints looked quite promising in the studies, it is not necessarily the case in the real experiment. Therefore, other selection variables than a single SCT-cut like a combined cut on SCT- and pixel spacepoints were additionally considered to form further event requirements and achieve efficient noise rejection. The spacepoints objects in the trigger are different at LVL2 and EF (see below at FEX\_1, FEX\_2). The measured time of 32 ms refer to the case that the spacepoint formation is performed with IdScan on the EF because necessary information of all silicon detectors is forseen to be available only at this stage. Theoretically, the time for complete data retrieval are included in the measured times for spacepoint formation in 32 ms. However, for the case spacepoints are rejected at LVL2, the usual time budget there does not necessarily apply to the minimum bias trigger. For time consumption exceeding the LVL2 latency, the LVL2 input rate has to be accordingly adjusted. To exploit a maximal minimum bias output-rate one can imagine a the time for complete silicon data collection + spacepoint formation + decision time for recording or rejecting the event to be  $x \cdot 10$  ms, where  $x$  denotes the factor taking into account the unknown time additionally needed to the LVL2 latency. Then the trigger rate becomes  $75 \text{ kHz}/x$  where  $75/x$  is at the same time the rejection factor at LVL2 charging EF with the remaining 1 kHz. The EF input will then contain more then 10 % interactions supposing the 10 % pp-interaction probability as estimated in section 5.3.

On the EF one can then make use of NewTracking algorithms starting by reforming the respective spacepoints with which tracking is performed to check the number of the tracks reconstructed within a certain  $z_0$  region. Dependent on this number possible background events are rejected. A chain executing these steps is described in the following.

## 6.2 Minimum Bias Trigger Chain

The trigger will be composed of random (RD) and a bunch group (BG) trigger on filled bunches as mentioned in section 4.3. This will be represented by a LVL1 trigger item which is named here RD+BG unrolling following chain. The chain is split in two sequences denoted in extensions of the FEX or HYPO. Each sequence is listed in terms of steps.

1. Step 1: **FEX\_1** is called by the mere existence of the LVL1 trigger item RD+BG. FEX\_1 inherits from **ALLTEA1go**<sup>1</sup> and is derived from algorithms of the package Trigger/TrigTools/TrigOnlineSpacePointTool. It
  - runs in an unseeded mode,
  - retrieves SCT + pixel data,
  - forms spacepoints,
  - outputs one TE with feature objects including the information of number of SCT spacepoints  $N_{\text{SCT}}$  and number of pixel spacepoints  $N_{\text{pixel}}$ .
2. Step 2: **HYPO\_1** is started by the output TE of step 1. It
  - checks if  $N_{\text{SCT}} \geq \text{threshold\_SCT}$ ,
  - checks if  $N_{\text{pixel}} \geq \text{threshold\_pixel}$ .
  - In case of a negative result of the checks the required input TE for the following FEX\_2 is deactivated. Else it proceeds with
3. Step 3: **FEX\_2** is started by the output TE of step 2. FEX\_2 should inherit in the same way from **ALLTEA1go** and is derived of respective algorithms for the EF belonging to InnerDetector/InDetTrigRecAlgs, i.e. omitting TRT-algorithms. FEX\_2
  - re-forms SCT and pixel spacepoints resulting in EF specific **SpacePoint** objects,
  - performs tracking,
  - outputs a TE providing the number of tracks within a certain  $z_0$ -region.
4. Step 4: **HYPO\_2** is started by the output TE of step 3, it
  - checks if  $N_{\text{tracks}} \geq \text{threshold\_tracks}$  and
  - records or rejects the event depending on the preceding check.

The minimum bias trigger chain looks rather simple in structure. However there are some issues undefined yet which concern feasibility of processing SCT and pixel data at LVL2. For this reason it has been on purpose ignored to specify the trigger level where the algorithms for empty bunch-crossing rejection should be run. Other open issues are that

---

<sup>1</sup>ALLTEA1go will be called exactly once per event performing a full scan of the inner detector.

further studies for background rejection of beam-gas and halo events should be performed when their simulation is available. This will help decide how much of the actual track reconstruction should be employed with respect to the almost standard tracking (standard, but without TRT). Final trigger thresholds can most likely be determined in “technical runs” where functionality of single trigger and data acquisition components are tested.

## Chapter 7

# Summary and Outlook

In this thesis studies have been performed for the realization of a minimum bias trigger based on random selection at LVL1 and event processing on HLT. This trigger will be employed in the start-up phase of LHC data-taking enabling to sample events whose physics of soft QCD-interactions is not fully understood to quantify the final state particles of proton-proton collisions. These soft interactions will however pile up in the detector especially when LHC reaches its design luminosity of  $\mathcal{L} = 10^{34} \text{ cm}^{-2}\text{s}^{-1}$ . Signatures of processes that house possible discoveries can only be undoubtedly identified if the characteristics of the soft QCD background are known. Therefore, these minimum bias events have to be understood as precisely as possible beforehand at lower luminosities. It was the aim of this thesis to make these studies possible. An independent approach to the minimum bias trigger that uses signals from the Minimum Bias Trigger Scintillators was followed and it was shown that an efficient selection of minimum bias events is also feasible using signals of the silicon sub-detectors of the inner tracking system. Two main background sources were investigated, empty bunch-crossing events, where the proton bunches do not interact but merely permeate each other, and beam-gas events that are created when the proton beam interacts with residual gas molecules in the beam-pipe. Those taking place close to the interaction point are most crucial. However, their rate was estimated to be around 30 kHz which is about a quarter of the expected minimum bias rate at an initial luminosity of  $\mathcal{L} = 10^{31} \text{ cm}^{-2}\text{s}^{-1}$ .

Two possible pattern recognition algorithms for low  $p_T$  track reconstruction were studied in more detail, one being IdScan employed at the second trigger level and the other one being NewTracking which is a offline pattern recognition algorithm modified to be used also at the third trigger level (EF). The adaptation of IdScan for low  $p_T$  track reconstruction failed due to insufficient reconstruction efficiency for tracks with  $p_T > 500 \text{ MeV}$ . Slightly more than 30% efficiency was obtained which could not be significantly increased. Satisfactory results for low  $p_T$  track reconstruction were obtained with NewTracking.

The best result for the minimum bias event selection is grounded on basically two selection variables in order to reject empty bunch-crossing and beam-gas events. First, a cut on three dimensional detector hits (spacepoints) in the semi-conductor tracker (SCT) can be applied whose microstrip technology allows already an intrinsic noise suppression. The use of solely SCT-information yields to a rejection of empty bunch-crossing events with  $(93.9 \pm 0.1)\%$  efficiency. At the same time the minimum bias events can be triggered with  $(99.5 \pm 0.1)\%$  efficiency. As second selection step a cut on the track multiplicity yielded a high suppression of beam-gas events using NewTracking. By the requirement of merely 2

tracks in the event,  $(98.6 \pm 0.1)\%$  of the minimum bias are retained while  $(91.8 \pm 2.5)\%$  of beam-gas events are rejected. A requirement of 5 tracks yields complete rejection of beam-gas events while  $(92.3 \pm 0.2)\%$  of the signal is kept.

These numbers showed that a highly efficient minimum bias trigger can be obtained by the application of cuts on the presented selection variables. However, the efficiencies for beam-gas event rejection should not be regarded as final numbers. It is very likely that they can change a little due to two reasons: A combined cut on SCT spacepoints and track multiplicity has not been investigated. However, it was estimated that the trigger efficiency with track requirement for minimum bias events decreases by less than 1% applying previously an SCT-cut at 20 spacepoints which affects only very few the minimum bias events. Another issue concerns the simulation of beam-gas events which has not reached final tunings yet. The analysed beam-gas events were rather simulated in a preliminary manner, although they showed main features of beam-gas collisions. However, new simulations of beam-gas events are underway taking into account several modifications in the GEANT4 detector simulation. For similar reasons the study of halo events had to be postponed.

Regarding the studies of time performance for the presented concept it was determined that the concept looks well realizable within the given trigger constraints. Already a sufficiently fast time performance was obtained for the latest tested trigger setup. These studies led to an improvement of the trigger algorithms that will be employed in a full scan on EF. However, new timing measurement are still to be done.

As the main criteria seem to be fulfilled for the presented concept the next step is the implementation of the flexible trigger following the requirements described in chapter 6. However, to determine the trigger threshold for the track based event selection studies on the new beam-gas and halo simulation should be performed. If it will be considered to incorporate the LVL2 farm as well in the selection special attention to the retrieval time of complete silicon data at this stage has to be paid.

## Acknowledgment

The last year has been very enriching for me thanks to all the new people and methods I got to know. I would like to express my special thanks to my supervisor Klaus Mönig who made this possible. In the same way I want thank Prof. Hermann Kolanoski. Their encouragement as well as their valuable support and criticism made it a pleasure for me to work in particle physics.

In addition, I would like to thank many people at CERN and in the MinimumBias-WorkingGroup for their interest in my work. In particular, I would like to thank John Baines for the warm welcome at RAL and all the helpful discussions. I am likewise thankful to Iwona Grabowska-Bold for her professional communication from the very beginning of the thesis. Special thanks belong also to Nick Ellis who gave important support to the work. All their feedback guided me throughout the year.

I also want thank my colleagues at Humboldt University and DESY, like Sami and Kai who shared their knowlegde of shell-pyhton-scripting and root-debugging issues with me or Felix for his power training lessons. But I owe my thanks also to many others who made physics so lively to me.

Special thanks go to Christiane Risler who put much effort into correcting the manuscript though she herself was quite busy. I will never forget Gwenola and Antoine and all the wonderful welcomes in Lausanne, Geneva and Villars-Tiercelin. Finally, I am very grateful to my family and my SchatzTresor Jan for everything they made possible for me.

# Appendix A

## Glossary

AOD - Analysis Data Objects

Data format containing condensed information of event data like trigger decision, track parameters.

ATLAS - a toroidal LHC apparatus

BS - Byte Stream

Data format in the TDAQ data flow

CTP - Central Trigger Processor

DAQ - Data Acquisition System

DD - double diffractive dissociation

DFM - Data Flow Manager

EBN - Event Building Network

EDM - Event Data Model

A computing model that allows commonality and consistency in software across the detector subsystems.

EF - Event Filter

third trigger level

ESD - Event Summary Data

Data format containing summarized event data including LVL2 and EF results

HEC - Hadronic End Cap

HLT - Higher Trigger Level

Term comprising the second and third trigger levels.

IdScan - Inner Detector Scan

track reconstruction algorithm employed at the second trigger level

IP - Interaction Point

L1A - level-1 accept

logical combination of trigger items

L2SV - level-2 supervisor

L2PU - level-2 processor unit

LHC - Large Hadron Collider

LVL1 - first trigger level

LVL2 - second trigger level

MBTS - Minimum Bias Trigger Scintillators

MC - Monte Carlo

NewT - NewTracking

track reconstruction algorithms used in the event filter and for offline analysis

QCD - Quantum Chromo Dynamics

pp-interaction - proton-proton interaction

$p_T$  - transverse momentum

PT - Processing Task

RDO - Raw Data Objects

ByteStream data with header information, obtained by digitization through the ByteStream Converters.

ROB - Read out Buffer

ROD - Read out Driver

ROS - Read out System

RoI - Region of Interest

Selected detector region showing activity above a certain trigger threshold.

RPC - Resistive Plate Chambers

Part of muon trigger chamber

SCT - Semi-Conductor Tracker

SD - single diffractive dissociation

SFI - sub-farm input

SP - spacepoint  
detector measurement with 3 dim- information

TE - Trigger Element

TRT - Transition Radiation Tracker

TDAQ - Trigger and Data Acquisition System

TGC - Thin Gap Chambers  
trigger chambers in the muon spectrometer

## Appendix B

# Error Calculation for Efficiency Computation

For efficiency computation of generally several cuts on a sample the selected part and the total sample are not independent. In [42] the error calculation for the general weighted case is demonstrated at length, here the unweighted case was used and is therefore shown in detail: If the efficiency  $\epsilon$  consists of the selected events having passed the cuts  $N_{pass}$  and the total number of events  $N_{total}$  by

$$\epsilon = \frac{N_{pass}}{N_{total}}$$

where  $N_{total}$  is the sum of  $N_{pass}$  and the events that are cut  $N_{cut}$ , the error  $\sigma_\epsilon$  can be determined using the derivations of the independent variables to

$$\sigma_\epsilon^2 = \left( \frac{\partial \epsilon}{\partial N_{pass}} \sigma_{N_{pass}} \right)^2 + \left( \frac{\partial \epsilon}{\partial N_{cut}} \sigma_{N_{cut}} \right)^2$$

The derivatives are

$$\frac{\partial \epsilon}{\partial N_{pass}} = \frac{N_{pass}}{N_{total}^2} \quad \frac{\partial \epsilon}{\partial N_{cut}} = -\frac{N_{cut}}{N_{total}^2}$$

while one can use for  $N_{total} \gg 1$  the uncertainties of the Poissonian distribution

$$\sigma_{N_{pass}} = \sqrt{N_{pass}} \quad \sigma_{N_{cut}} = \sqrt{N_{cut}}$$

which yields via

$$\sigma_\epsilon^2 = \frac{N_{cut} \cdot N_{pass}}{N_{total}^3}$$

to the formula given in (5.3).

## Appendix C

# Parameters for low $p_T$ Adaptation in IdScan

The efficiency for each parameter couple was obtained by taking the ratio of the number of reconstructed tracks to the generated using the acceptance and visibility criteria respectively as defined in section 5.5.1.

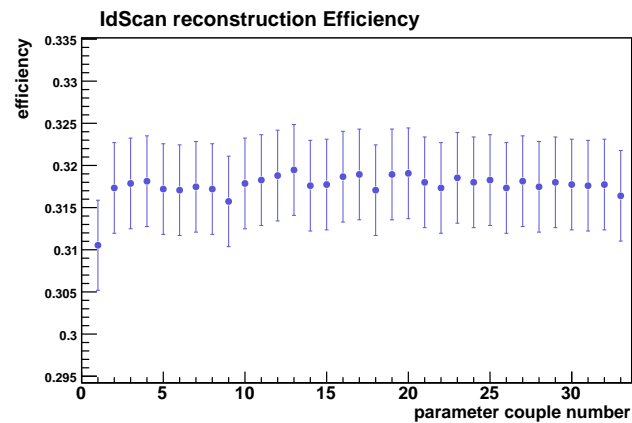


Figure C.1: IdScan reconstruction efficiencies shown for each parameter couple. This figure was shown in section 5.5.3.

$\delta\phi[^\circ]$	z-bin size [cm]	efficiency [%]
4	0.2	31.79
4	0.5	31.83
4	1	31.88
4	1.5	31.95
5	0.2	31.76
5	0.5	31.77
5	1	31.87
5	1.5	31.89
6	0.2	31.71
6	0.5	31.89
6	1	31.91
6	1.5	31.80
7	0.2	31.73
7	0.5	31.85
7	1	31.80
7	1.5	31.83
8	0.2	31.73
8	0.5	31.81
8	1	31.75
8	1.5	31.80
9	0.2	31.77
9	0.5	31.76
9	1	31.77
9	1.5	31.64
10	0.2	31.73
10	0.5	31.79
10	1	31.81
10	1.5	31.72
11	0.2	31.70
11	0.5	31.75
11	1	31.72
11	1.5	31.57

Table C.1: Idscan parameters,  $\phi$ -bin size and the z-resolution parameter, with respective efficiency.

# List of Figures

2.1	Resolving the hierarchy problem in the SM by introducing a supersymmetric partner particle $\tilde{t}$ to the SM $t$ . The contribution of quadratic divergencies in Higgs production cancels out automatically and no unnatural fine-tuning is needed in SUSY. . . . .	4
2.2	Higgs production modes either by gluon-gluon fusion (a) $gg \rightarrow H$ and (d) $gg \rightarrow t\bar{t}H$ or by vector boson fusion (VBF) (b) $qq \rightarrow WW, ZZ \rightarrow qqH$ and (c) $qq \rightarrow WH, ZH$ . The outcome is either a direct (a,b) or an associated (c,d) Higgs production. . . . .	6
2.3	Cross-section predictions for different channel modes. The associated Higgs production has smaller cross-sections than the direct production. Largest contribution may come from $gg \rightarrow H$ . . . . .	7
2.4	Higgs decay produced in $t\bar{t}H$ -channel. . . . .	7
2.5	The SM-like Higgs can be seen in ATLAS in most cases with $5\sigma$ significance. . . . .	8
2.6	Cross-section predictions for different physics processes at LHC. Compared to QCD-background e.g. heavy jet production where $E_T^{jet} > 100$ GeV the light Higgs with $m_H = 150$ GeV is produced only with a ratio of $10^{-5}$ . . . . .	10
2.7	Cross-section prediction for LHC. Total $p\bar{p}$ (empty dots) and $pp$ (black dots) were fitted to $(\ln s)^\gamma$ . At LHC energies the fit-prediction ranges from 90-120 mb. . . . .	12
2.8	A typical non-diffractive process: By gluon radiation in a proton-proton collision a color field is produced which allows final state particles everywhere in the detector. . . . .	13
2.9	Schematic processes for diffraction: The exchange of color-neutral objects, here in Pomeron picture ( $\mathbb{P}$ ), gives rise to rapidity gaps (RG) where final state particles are exponentially suppressed. Shown are single diffractive (left), double diffractive (middle) and central diffractive dissociation (right). The dissociated system is assigned a mass $M$ . . . . .	14
3.1	Four major experiments located along the tunnel of the Large Hadron Collider. ATLAS, CMS, LHCb and ALICE. ATLAS is situated at Point 1. . . . .	16
3.2	Computer animation of the ATLAS detector in its full beauty. Indicated are the main components of the detector. Especially the large toroidal magnets are eye-catching, giving ATLAS the name. . . . .	17
3.3	The tracking system, consisting of two silicon sub-detectors pixel and SCT and a gaseous tracking chambers featuring transition radiation detection TRT. . . . .	18
3.4	Arrangement of pixel detector components. The barrel, which consists of three cylindrical layers, is enclosed by 5 disks at each side representing the pixel endcaps. This figure is taken from [15]. . . . .	19

3.5	Arrangement of the SCT detector components. The barrel, which consists of four cylindrical layers and nine disks at each side of the endcap. This figure is taken from [18]. . . . .	20
3.6	Ghost spacepoints in silicon strip detectors. Thanks to a very small stereo-angle the impact of ghost hits can be reduced in pattern recognitions. In blue and green are the strips shown for a front- and back-side of a SCT module. The black lines indicate a hit on these strips. Assuming the black dots as true spacepoints, the white dots will be also registered as spacepoints, though they are ghosts. From the right picture one can imagine many more possibilities of ghost spacepoints (only few strips are indicated). . . . .	21
3.7	Planned deployment of the MBTS (red). The yellow spot represents the IP while the horizontal line is the beam-axis. The scintillators are mounted on the front-face of the LAr endcaps of the hadronic calorimeter and provide a total acceptance of $2.12 <  \eta  < 3.85$ . . . . .	22
3.8	Calorimetric system in ATLAS. In yellow the electromagnetic calorimeters based on the LAr technique are shown. Also part of the hadron calorimeter uses LAr technique (red). For larger radii with respect to the beam-line the hadronic calorimeter is made of iron tile scintillators. . . . .	23
3.9	Muon Spectrometer. Shown are: Monitored Drift Tube (MTD) and Cathode Strip Chambers (CSC) as well as Resistive Plate Chambers (RPC) and Thin Gap Chamber (TGC). . . . .	25
4.1	Overview of the ATLAS Trigger and Data Acquisition System. It shows functional elements and their connections, see text for explanations. This figure is taken from [21]. . . . .	28
4.2	Example for signature tables (horizontally) and two trigger chains (vertically). In case of the left trigger chain a signature consists of two equal trigger elements of an electron with at least $p_T \geq 50$ GeV. The refinement is indicated by ' . . . .	30
5.1	Sketch of the acceptance of Minimum Bias Trigger Scintillators (MBTS). The event selection is restricted to events with tracks with $2.12 <  \eta  < 3.85$ . . . .	34
5.2	Concept of the random based track trigger for minimum bias events: At the first stage at LVL1 a random trigger selects with a rate of 1 kHz, that are passed through LVL2 and processed on the third trigger level using its maximal processing capacity of 1 kHz to obtain a storage rate of 100 Hz. . . . .	36
5.3	Illustration of perigee parameters $d_0$ and $\phi_0$ . The longitudinal impact parameter $z_0$ is the z-coordinate of the perigee. . . . .	37
5.4	shows a sketch of the reconstruction mechanism of IdScan from the transverse plane: Filled dots represent detector hits of a high $p_T$ track and empty dots hits of a low $p_T$ track. By slicing the transverse plane in $\phi$ one can grep most of the 3d-hits of a high $p_T$ particle in one slice (filled dots) while those of a low $p_T$ track (empty dots) are distributed over several slices. . . . .	39
5.5	MC truth distribution of particles per event. About 15 charged stable particles per event are expected at design luminosity. Not shown are the number of neutral particles created in pp-collisions as they are invisible to the inner detector tracking system. . . . .	43

5.6	MC truth $p_T$ -distribution of minimum bias events. The charged stable particles rather settle at lower $p_T$ -values, showing an exponentially suppressed $p_T$ -spectrum. . . . .	43
5.7	MC truth distribution of pseudorapidity in minimum bias events. The particles are approximately flat distributed in $\eta$ . . . . .	44
5.8	As expected no tracks are reconstructed in empty events, neither on LVL2 by IdScan (right) nor on EF by NewT (left). . . . .	47
5.9	Comparison of noise events of real data (right) and simulation (left). For the real data several data files from a $\pi/2$ of the SCT barrel were used indicated by different run numbers. . . . .	49
5.10	Noise events of recorded in cosmic runs for $\pi/2$ of the SCT-endcap. . . . .	49
5.11	Comparison of summed noise events of real data from $\pi/2$ of the SCT barrel and $\pi/2$ of the SCT endcap (grey) and simulation of SCT spacepoints of minimum bias events (blue). In red and magenta are the double and single diffractive events shown. A relatively low cut can be applied at around 25 to reject empty events already while keeping almost all of the signal. . . . .	50
5.12	Simulated noise spacepoints in the pixel detector are compared to pixel spacepoints of minimum bias and diffractive events. As the distributions of noise and minimum bias events overlap significantly it will not be possible to remove empty events with a single cut on pixel spacepoints completely without losing efficiency in the signal. . . . .	51
5.13	Trigger efficiency for essentially minimum bias (blue), empty (dark grey) and for other datasets are shown when applying a cut on sct spacepoints. For the empty events real data of $\pi/2$ of the SCT detector were used linearly scaled to the whole detector. . . . .	52
5.14	Trigger efficiency is shown for the case that a single cut on pixel spacepoints is applied. Though one could principally reject also empty events by cutting on pixel spacepoints e.g. at around 900, one loses also efficiency on the signal. SD and DD show a very similar behaviour which is not very surprising. . . . .	53
5.15	A comparison of possible cuts is illustrated. The signal trigger efficiency in dependence of empty event rejection efficiency is shown for the case when a single cut on pixel (black), a cut on SCT spacepoints (red) and an OR-combined cut of SCT or pixel spacepoints (green) are applied (left). An SCT-cut looks more efficient as a pixel cut. The combined cut may achieve high trigger efficiency but then without a high empty event rejection (right). . . . .	53
5.16	In yellow is shown the distribution of visible generated particles and in hashed the by IdScan reconstructed $p_T$ values of the tracks. . . . .	54
5.17	Illustration of parameters of spacepoints (blue dots) to the track : On the left the angle definitions in $\phi$ are shown, on the right they are related to the $p_T$ -dependent track radius $R$ . The framework is chosen such that $\phi_0 = 90^\circ$ . . . . .	55
5.18	The difference of reconstructed and true z-positions averaged over 10 events is shown as a function of $\phi$ -bin size (left) and z-bin size. . . . .	56
5.19	IdScan reconstruction efficiencies shown for each parameter couple. Obviously one can not recognise a significant efficiency rise. . . . .	57
5.20	NewT reconstruction efficiency. Shown are the $p_T$ -spectra from MC and reconstructed. Visibility-criteria were used for the MC sample and the requirement that $ \eta_{rec}  < 2.5$ for the reconstructed distribution. Fake tracks are excluded. . . . .	58

5.21	Event multiplicity for tracks reconstructed in NewT shown together with MC truth multiplicity. A mean value of 15 reconstructed tracks per event can be expected, for the truth there are around 15.5 particles considering the visibility criteria. . . . .	58
5.22	Event characteristics for single diffractive events reconstructed with NewT: $p_T$ -spectrum (left) and track multiplicity (right). For both distributions the cut at $ \eta  < 2.5$ was applied. . . . .	59
5.23	Events characteristics for double diffractive events reconstructed with NewT: $p_T$ (left), track multiplicity (right). For both distributions $ \eta  < 2.5$ was required. . . . .	59
5.24	Beam-gas events characteristics generated in Hijing: $p_T$ (left), number of particles (right). Here only stable charged particles inside the inner detector with $p_T > 500$ MeV are accounted. . . . .	60
5.25	Distributions of beam-gas events characteristics reconstructed with NewT: $p_T$ (left), track multiplicity (right). Out of around 3000 events, about 1000 for the species C, H and Be, only 61 events could be reconstructed. . . . .	60
5.26	Distribution of longitudinal impact parameter $z_0$ of minimum bias events. The thick line indicated particles having passed an additional cut at $ z_0  = 200$ mm. . . . .	61
5.27	Distribution of longitudinal impact parameter $z_0$ of beam-gas events. As in figure 5.26 the thick line indicated particles having passed an additional cut on at $ z_0  = 200$ mm. The asymmetry in the distribution is due to single-sided event simulation. As ATLAS is symmetric one can simply imagine the same simulation mirrored. . . . .	61
5.28	Trigger efficiency for minimum bias (blue), single diffractive (magenta), double diffractive events (red) and beam-gas events are shown requiring a certain track multiplicity. . . . .	62
C.1	IdScan reconstruction efficiencies shown for each parameter couple. This figure was shown in section 5.5.3. . . . .	76

# List of Tables

2.1	Cross-section predictions at LHC energy of 14 TeV. Despite of different predictions for $\sigma_{tot}$ one recognises that the non-diffractive part (nd), usually referred to minimum bias events, contributes largely in contrast to single and double diffractive (sd, dd) events. While in PHOJET also central diffraction (cd) was simulated, it was not in PYTHIA [10], however the differences between these two model are relatively large (more than 50% for the elastic processes). . . . .	13
5.1	Scoring strategy employed for ambiguity solving by evaluation of track characteristic. Track scores are distributed according to the sub-detector and detector layer; + symbolizes a benefit and - a penalty. . . . .	41
5.2	Events considered for the presented minimum bias trigger concept. The diffractive events were neither background nor signal events. They are rather counted to signal but with less priority w.r.t the non-diffractive processes. Halo events have not been studied here but will be treated as background. . . . .	42
5.3	Estimation of the gas rate in the start-up phase is listed for main gas species close to the interaction point at $\pm 25$ cm and for the inner detector acceptance at $\pm 3.5$ m. . . . .	45
5.4	To define the Monte Carlo truth sample several cuts were used ensuring to take only those into account that are <i>visible</i> . Application of the last cut is a looser restriction on the sample. . . . .	46
5.5	Mean number of spacepoints in the SCT and pixel detector for empty events. The SCT-values were obtained from data while the value for pixel spacepoints was obtained from simulation. The small error for the endcaps is due to the larger sample that was available. . . . .	50
5.6	The parameter which was tuned is $\delta\phi$ determining the $p_T$ -cut in IdScan. . . . .	55
5.7	The trigger efficiency for 2 and 5 track requirements are listed for minimum bias (signal), diffractive (non-background) and beam-gas events (background). Only a cut at the number of tracks with $ \eta  < 2.5$ has been applied. . . . .	62
5.8	Time consumption for track reconstruction of trigger setup (EF) in release 13. The $p_T$ -cut was at 500 MeV. Measurements were performed on atlhlt3. . . . .	64
5.9	Time consumption for minimum bias events with a $p_T$ -cut at 500 MeV and run in an constraint search. Release 12.0.6 was used for track reconstruction at the EF. The times are averaged values. . . . .	65
C.1	Idscan parameters, $\phi$ -bin size and the z-resolution parameter, with respective efficiency. . . . .	77

# Bibliography

- [1] W.-M.Yao et al. (Particle Data Group), *J. Phys. G* **33**, 1 (2006) and 2007 partial update for the 2008 edition
- [2] G.Altarelli, M.W.Grünwald, *Precision electroweak tests of the Standard Model*, *Phys. Reports*, 403-404 (2004), 189-201
- [3] Lectures of W. Bietenholz and U.-J.Wiese, *The Standard Model of Particle Physics*, October 2005
- [4] F. Gianotti, *Physics at the LHC*, *Physics Reports*, 403-404 (2004), 379-399
- [5] Tevatron Electroweak Working Group (for the CDF and D0 Collaborations), *A Combination of CDF and D0 Results on the Mass of the Top Quark*, arXiv:hep-ex/0703034v1, 19. March 2007
- [6] M. Barisonzi, *Mass measurements of the top quark in electroweak production channels at ATLAS*, PhD Thesis, 31. May 2006
- [7] F. Abe et al., *Phys. Rev. D* **47** (1993) 4857;  
F. Abe et al., *Phys. Rev. Lett.* **79** (1997) 584;  
F. Abe et al., *Phys. Rev. D* **56** (1997) 3811
- [8] N. M. Amos et al., *Phys. Rev. Lett.* **68** (1992) 2433
- [9] F. Abe et al., *Phys. Rev. D* **50** (1994) 5550
- [10] J.P. Guillaud and A. Sobol, *Simulation of diffractive and non-diffractive processes at the LHC energy with PYTHIA and PHOJET MC event generators*, LAPP-EXP 2004-06, July 2004
- [11] M. Arnedo and M.Diehl, *Diffraction for Non-believers*, [www.desy.de/heralhc/proceedings/wg4intro-diff.pdf](http://www.desy.de/heralhc/proceedings/wg4intro-diff.pdf)
- [12] V. Barone and E.Predazzi, *High-Energy Particle Diffraction*, Springer-Verlag Berlin Heidelberg, 2002
- [13] Atlas Fact Sheet 5 (LHC)
- [14] M. Keil, *Pixeldetektoren aus Silizium und CVD-Diamant zum Teilchennachweis in ATLAS bei LHC*, Dissertation, Oktober 2001
- [15] *Pixel Detector Technical Design Report*, ATLAS TDR 11, CERN/LHCC 98-13, 1998

- [16] [http://atlas.web.cern.ch/Atlas/GROUPS/INNER\\_DETECTOR/PIXELS/pixel.html](http://atlas.web.cern.ch/Atlas/GROUPS/INNER_DETECTOR/PIXELS/pixel.html)
- [17] *Calorimeter Performance Technical Design Report*, CERN/LHCC 96-40, 13 Jan 1997
- [18] *Inner Detector Technical Design Report*, ATLAS TDR 5, CERN/LHCC/97-17, ISBN 92-9083-103-0, 30. April 1997
- [19] *ATLAS Muon Spectrometer Technical Design Report*, CERN/LHCC/97-22 – ATLAS TDR 10 (ISBN 92-9083-108-1), 31 May 1997
- [20] Atlas Detector Fact Sheet
- [21] L. Mapelli, *The ATLAS Trigger and Data Acquisition*, slides, 16. January 2006
- [22] Technical Design Report, *ATLAS High-Level Trigger Data Acquisition and Controls*, CERN/LHCC/2003-22, ATLAS TDR 016, 30 June 2003
- [23] <https://twiki.cern.ch/twiki/bin/view/Atlas/TriggerPerformanceTargets>
- [24] J.Haller, R.Stamen, *Steering, Configuration and Implementation of HLT Trigger Menus*, Atlas Note, Version 1.0, 23. April 2006
- [25] <https://twiki.cern.ch/twiki/bin/view/Atlas/EventDataModel>
- [26] F. Akesson, T. Atkinson, M.J. Costa, M. Elsing, S.Fleischmann, A.Gaponenko, W.Liebig, E.Moyse A.Salzbunger and M. Siebel *ATLAS Tracking Event Data Model* ATLAS Note, ATL-COM-SOFT-2006-004
- [27] A.Moraes, C.Buttar and I.Dawson, *Prediction for minimum bias and underlying event at LHC energies* Scientific ATLAS Note SN-ATLAS-2006-057, re-submitted 23. January 2007
- [28] E. Feng, Pilcher, J. E., *Triggering ATLAS with Minimum Bias Trigger Scintillators*, ATL-COM-TILECAL-2007-013 (2007), <http://cdsweb.cern.ch/record/1034461>
- [29] discussions in the Minimum Bias Working Group Meeting, May 2007
- [30] discussions in the trigger menu meeting at CERN, 23.May 2007, <http://indico.cern.ch/conferenceDisplay.py?confId=16537>
- [31] discussion with John T. Baines and Nick Ellis
- [32] private communication with Carlo Schiavi, May 2007
- [33] talk by E.Özcan, *IDSCAN Zfinder*, in ATLAS PESA InDet Meeting, 3.October 2006, <http://indico.cern.ch/conferenceDisplay.py?confId=6316>
- [34] H. Drevermann, N. Konstantinidis, *Determination of the z position of primary interactions in ATLAS prior to track reconstruction*, ATL-SOFT-CONF-2002-007 (2002).
- [35] J. Baines, H. Drevermann, D. Emeliyanov, N. Konstantinidis, F. Parodi, C. Schiavi and M. Sutton, *Fast Tracking for the ATLAS LVL2 Trigger*, ATL-DAQ-CONF-2005-001 (2005).

- [36] T.Cornelissen, M.Elsing, S.Fleischmann, I.Garvilenko, W.Liebig, E.Moyse and A.Salzburger, *Concepts, Design and Implementation of the ATLAS New Tracking (NEWT)*, ATLAS Note, ATLAS-COM-SOFT-2007-002 (2007)
- [37] private communication with Richard Batley, April 2007
- [38] private communication with John T. Baines, January 2007
- [39] <https://twiki.cern.ch/twiki/bin/view/Atlas/MonitoringLogbook>
- [40] <https://twiki.cern.ch/twiki/bin/view/Atlas/ListOfDataRunsSR1Endcap>
- [41] <https://twiki.cern.ch/twiki/bin/view/Atlas/PixelCosmicsAnalysisResults>
- [42] B. Laforge and L. Schoeffel, *Elements of Statistical Methods in High Energy Physics Analysis*, H1 08/97-528
- [43] M. Boonekamp, F.Gianotti, R. A. McPherson, M. Nesi and P. Nevski, *Cosmic Ray, Beam-Halo, Beam-Gas Rate Studies for ATLAS Commissioning*, ATLAS-GEN-2004-001, March 2007
- [44] A. Rossi and N. Hilleret, *Residual Gas Estimations in the Experimental Interaction Regions*, LHC project report 674, 2003
- [45] LHC Design Report, Volume I
- [46] Work by Iwona Grabowska-Bold, see her talk at Inner Detector Trigger Meeting, 22. May 2007, <http://indico.cern.ch/conferenceDisplay.py?confId=13414>
- [47] private communication with Dmitry Emilianov and John Baines, Trigger and Physics Week, November 2006
- [48] discussion in TAPM Meeting 12. April 2007, private communication with Imma Riu, presentations on results in technical run, see talk of Imma Riu and Xin Wu: <http://indico.cern.ch/conferenceDisplay.py?confId=14318> <http://indico.cern.ch/conferenceDisplay.py?confId=14412>

# Selbständigkeitserklärung

Hiermit erkläre ich, dass die vorliegende Arbeit selbständig und nur mit Hilfe der in der Literatur angegebenen Referenzen verfasst wurde.

Berlin, 19. Juli 2007